



SAPIENZA
UNIVERSITÀ DI ROMA

Measurement with the FOOT apparatus of ^{16}O fragmentation cross sections relevant for Particle Therapy applications

Facoltà di Scienze Matematiche, Fisiche e Naturali
Corso di Laurea Magistrale in Fisica

Candidate

Federica Murtas
ID number 1715900

Thesis Advisor
Prof. Giacomo Traini

Co-Advisor
Prof. Marco Toppi

Academic Year 2019/2020

Measurement with the FOOT apparatus of ^{16}O fragmentation cross sections relevant for Particle Therapy applications

Master thesis. Sapienza – University of Rome

© 2020 Federica Murtas. All rights reserved

This thesis has been typeset by L^AT_EX and the Sapthesis class.

Version: October 5, 2020

Author's email: murtas.1715900@studenti.uniroma1.it



*"C'è una forza motrice più forte del vapore,
dell'elettricità e dell'energia atomica:
la volontà"*
-Albert Einstein-

Acknowledgments

Finalmente, dopo cinque lunghi anni, è arrivato il tanto atteso traguardo.

Prima di lasciare spazio alla trattazione della mia tesi vorrei ringraziare chi mi è stato accanto in questo percorso. Ringrazio il prof. Faccini per avermi fatto conoscere ed appassionare alla Fisica Medica, che ora spero possa diventare il mio lavoro, e per avermi proposto il percorso di tesi con l'esperimento FOOT. La sua presentazione mi ha portato a conoscere il gruppo SBAI che, dal primo giorno, mi ha accolto e fatto sentire il suo appoggio. Voglio ringraziare prof. Alessio Sarti, il primo che ho avuto modo di incontrare, che con il suo modo di fare ha fatto sì che da "laureanda impaurita" diventassi "laureanda" e basta. Voglio ringraziare in modo particolare il mio correlatore il prof. Marco Toppi che mi è stato accanto tutti questi mesi, 24 ore su 24, aiutandomi a rendere questo lavoro di tesi così soddisfacente. Il periodo di Covid-19 ci ha imposto la lontananza ma Google Meet - Skype - Zoom ed il cellulare hanno fatto sì che non ci sentissimo mai davvero distanti e completissimo nel migliore dei modi questa "tesi al telefono". Ringrazio il mio correlatore anche per avermi fatto presentare innumerevoli volte il nostro lavoro (preparando slide all'ultimo minuto) al gruppo di ricerca, questo mi ha permesso, superato l'iniziale ostacolo dell'imbarazzo, di essere più preparata ed in grado di esporre il mio lavoro ad un pubblico competente in materia. Lo ringrazio soprattutto per avermi sempre incoraggiato e mai lasciato a sbattere la testa sui bug nei codici da sola.

Un doveroso ringraziamento va anche al mio relatore, Giacomo Traini, per il quale spero di essere stata una valida prima tesista, al professor Vincenzo Patera che è in grado di dispensare importanti insegnamenti sempre con il sorriso, ed a tutto il meraviglioso gruppo SBAI che ti fa sentire come a casa.

Nonostante in questi mesi io non abbia più frequentato assiduamente il dipartimento di Fisica ne ho una parte nel cuore. Per questo motivo voglio dire grazie anche a chi mi ha sempre fatto da spalla durante le lezioni, gli esami, le pause caffè ed anche le pause pranzo: Gaia e Giulia. Due persone uniche che ho conosciuto tra i banchi dell'università nei primi giorni di lezione del primo anno e che mi hanno accompagnato fino all'ultimo giorno dell'ultimo anno e spero continueranno a farlo sempre. Loro sono state una valvola di sfogo, sempre pronte a placare la mia ansia o a farmi fare un sorriso, e un aiuto inestimabile nella preparazione dei moltissimi esami sostenuti insieme. Insieme a loro va ringraziato tutto il fantastico gruppo che ha fatto trascorrere questi anni così veloce, alleggerendone il peso, ed in particolare Federica e Chiara senza le quali molte giornate sarebbero state più grigie. Loro hanno saputo consigliarmi, ascoltarmi e ridere con me, sempre.

Al di fuori dell'università ci sono gli amici storici, quelli che conoscono tutto di te e sanno cosa ti succeda ogni giorno, da più di dieci anni, quindi un grazie speciale a Martina, compagna di banco fedele e amica preziosa ma anche a Marta, Luca e Alessandro.

Per ultima, ma prima nel mio cuore, la mia famiglia. A loro devo TUTTO. A mio padre e mia madre, che non mi hanno mai fatto mancare nulla, mi hanno dato la possibilità di raggiungere i miei obiettivi e mi hanno sostenuto e sopportato quando nessun altro sarebbe stato in grado di farlo. Grazie anche a mia sorella, Francesca, la piccola di casa, un punto di riferimento saldo, senza di lei quelle mura sarebbero

così silenziose da dar fastidio.

Voglio ringraziare anche i miei nonni, Renata, Elena e Enzo, per ogni "in bocca al lupo" ed anche nonno Mario, che spero in questo momento mi guardi, so che sarebbe orgoglioso.

Concludo con un sincero e profondo grazie a Marco che in questi ultimi tre anni ha saputo comprendermi, cosa che ammetto essere complicata, e starmi accanto apprezzando anche i miei difetti. Senza di te nulla sarebbe come è.

Contents

Introduction	ix
1 Charged Particle Therapy (PT)	1
1.1 Radiation interaction with matter	2
1.1.1 Bethe-Bloch curve	2
1.1.2 Dose deposition and Bragg Peak	4
1.1.3 Stopping Power and Linear Energy Transfer (LET)	5
1.1.4 Range and angular straggling	7
1.2 Nuclear Fragmentation	10
1.2.1 Influence of nuclear reactions on delivered dose	11
1.2.2 Reaction cross section and its impact on dose deposition computation	13
1.2.3 Role of secondary fragments	14
1.3 Biological Effectiveness	16
1.3.1 Linear-Quadratic model	17
1.3.2 Relative Biological Efficiency factor (RBE)	18
1.3.3 Oxygen effect	20
1.4 Importance of a well known RBE and nuclear cross section	21
2 FOOT experiment (FragmentatiOn of Target)	25
2.1 Experiment main goals	25
2.2 Methods and materials	26
2.2.1 Inverse kinematic approach	27
2.2.2 FOOT Target	29
2.3 Experimental Apparatus	30
2.3.1 Magnetic spectrometer	30
2.3.2 Emulsion Chamber	39
3 Monte Carlo Simulation and measurements	43
3.1 Fluka	44
3.2 Isotopic identification of fragments	46
3.2.1 Beam Energy and fragments energy loss measurement	47
3.2.2 Time Of Flight measurement	48
3.2.3 Momentum measurement	49
3.2.4 Charge identification	50

4	Z identification with TW detector	51
4.1	Bethe-Bloch parametrization on Monte Carlo	51
4.1.1	Tuning of the Monte Carlo on Data	53
4.2	Charge assignment	54
4.3	Algorithm performances	56
4.4	Critical Aspects	56
4.5	Moving from Simulation to GSI data	59
4.5.1	Implementation of the detector calibration	59
4.5.2	Ghosts management	63
4.6	Final result on GSI 2019 data	64
5	Fragmentation Cross Sections	69
5.1	Detectors alignment and angular acceptance	69
5.2	Monte Carlo simulation and detector efficiency	71
5.3	Clustering implementation	74
5.4	Event selection and fragment yields extraction	76
5.5	Fragmentation cross sections	78
5.6	Future corrections to the cross sections measurement	80
5.6.1	Charge mixing matrix	80
5.6.2	Secondary fragments impact	81
	Conclusions	83
	A Bethe-Bloch parametrized curves	85
	B Bisection method	89
	C Birk's Law	91

Introduction

Life expectancy and healthy life expectancy (HALE) have both increased by over 8% globally between 2000 and 2016, and remain profoundly influenced by income. Compared with the advances against communicable diseases, there has been a smaller progress in preventing and controlling premature death from noncommunicable diseases (NCDs). However, countries need comprehensive strategies to reduce these causes of death more effectively in order to achieve global targets by 2030.

An estimated 41 million people worldwide died of NCDs in 2016, equivalent to 71% of all deaths. Four NCDs caused most of those deaths: cardiovascular diseases (17.9 million deaths), cancer (9.0 million deaths), chronic respiratory diseases (3.8 million deaths), and diabetes (1.6 million deaths). The probability of dying from any one of the four main NCDs between the ages of 30 and 70 decreased by 18% globally between 2000 and 2016. The most rapid decline in the age-standardized ‘premature’ mortality rate – defined as mortality rate between ages 30 and 70 – is seen for chronic respiratory diseases (40% lower), followed by cardiovascular diseases and cancer (both 19% lower). Diabetes, however, is showing a 5% increase in premature mortality. In high-income countries, cancer has become the leading cause of premature death.[1]

There are many type of cancer treatment. The types of treatment depend on the type of cancer and how advanced it is. The most common treatments are surgery, radiation therapy (involving X-rays and charged particles), chemotherapy, immunotherapy and targeted therapy; some people with cancer have only one of them, but most people have a combination of treatments, such as surgery with chemotherapy and/or radiation therapy.

Radiotherapy is an essential component of cancer therapy. For irradiating tumors, radiation oncologists can use either photons (X-rays) produced at linear electron accelerators (linacs), or charged particles, which include protons and heavy ions (typically carbon). Out of the approximately two-thirds of patients with cancer who are treated with radiotherapy, > 80% receive X-rays and only about 0.8% receive radiation from high-energy charged particles, a proportion that is rapidly increasing[2].

Charged Particle Therapy (PT) uses proton or ^{12}C beams to treat deep-seated solid tumors, and due to the advantageous characteristics of charged particles energy deposition in matter, the maximum of the dose is released to the tumor at the end of the beam range, in the Bragg peak region. However, the nuclear interactions of the beam nuclei with the patient tissues induce fragmentation both of projectile and target nuclei and need to be carefully taken into account. In proton treatments, considering that the ions of the beam have the lowest possible atomic number (${}_1p$)

there is only the fragmentation due to the target ions, it can induce low energy, short range fragments along all the beam path, that may deposit a non-negligible dose in the entry channel. On the other hand in treatments with ^{12}C , or other possible ions of interest, like ^4He or ^{16}O , the main concern is long range fragments, produced by projectile fragmentation, that release their dose in the healthy tissues. Treatment planning software based on deterministic codes, and benchmarked on Monte Carlo simulations, are not yet able to reproduce such mixed radiation field modified by fragmentation, with the accuracy of 3% required in the field of the radiotherapy[43][44]. This discrepancy between computed and released dose is due to a lack of experimental data, in particular of the most valuable results, the double differential cross section measurements with respect to the angle and the kinetic energy of the fragment, that, when inserted in the nuclear models used, will allow to have better predictions for the treatment plans. In recent years some experiments have been dedicated to the measurement of the projectile fragmentation cross sections for ^{12}C ions, however this program was carried out only for a few, energies-target combinations[45][46][47]. As a matter of fact, a complete set of experimental data for double differential fragmentation cross sections on thin targets are still badly missing.

The **FOOT** (FragmentatiOn Of Target) collaboration composed of researchers from France, Germany, Italy and Japan, designed an experiment to study these processes. The experiment is meant to investigate target (mainly ^{12}C and ^{16}O nuclei) fragmentation induced by 50÷200 MeV proton beams. The nuclear fragmentation cross section on hydrogen will be studied via an inverse kinematic approach, where ^{12}C and ^{16}O therapeutic beams collide on graphite and hydrocarbon targets. Increasing the beam energy to 400÷500 MeV/u also the projectile fragmentation of these beams, impinging on targets of interest for PT, will be explored. The same process is of interest for the case of ^4He with beam energies up to 200 MeV/u. The FOOT detector will also be able to study the interaction of the same beams with hydrogen-rich targets at the increased energy range of 100÷800 MeV/nucleon of interest in the field of radioprotection in space.

My thesis project is focused on two main topics:

1. The development of the algorithms for the fragments charge identification through one of the FOOT detectors, an hodoscope of two layers of plastic scintillator bars, called Tof-Wall (TW). Such detector provides a simultaneous measurement of the energy release and the crossing time of an impinging fragment, that paired with the starting time measurement, performed through another scintillating detector, positioned few meters in front of the TW, measures the Time-Of-Flight (TOF).
2. The analysis of the data acquired in 2019 in GSI laboratory (Gesellschaft für Schwerionenforschung, Darmstadt, Germany) with a partial set-up of the final FOOT detector, in which the TW was the only detector for the identification of the fragments, performed to measure the elemental and total charge-changing cross sections for an oxygen beam at 400 MeV/nucleon impinging on a carbon target.

In Chapter 1 the basics of radiation interaction with matter for the charged particles and a description of the relevant radiobiological parameters adopted in PT will be introduced. Chapter 2 will describe the experimental setup adopted in the FOOT experiment. Chapter 3 will present the Monte Carlo (MC) FLUKA code adopted in the FOOT experiment to perform studies and the measurement strategies. The fragments charge identification algorithm with its performances and application is reported in Chapter 4. To conclude, in the Chapter 5, the measurement strategy of the fragmentation cross sections, for the process $^{16}\text{O} + C$ at beam energies of 400MeV/nucleon, is reported, together with the obtained preliminary results.

Chapter 1

Charged Particle Therapy (PT)

Radiation therapy is the medical use of ionizing radiation to treat cancer. In conventional radiation therapy, beams of X-rays are produced by accelerated electrons and then delivered to the patient to destroy tumor cells. Using a number of beams greater than one and delivering them from many angles, radiation oncologists irradiate the tumor target while trying to spare the surrounding normal tissues. Inevitably some radiation dose is always deposited in the healthy tissues due to the characteristic X-ray dose profile shown in the following figure. When the irradiating beams are

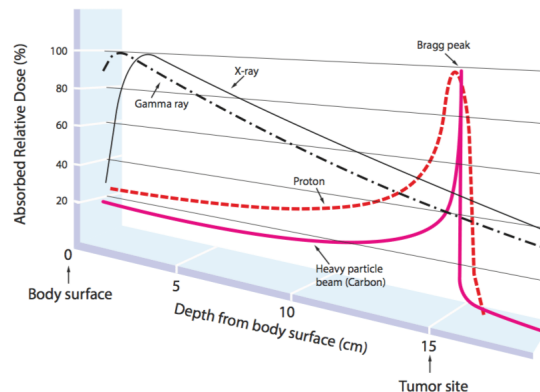


Figure 1.1. Schematic comparison of the dose of radiation released as a function of the penetration into the human body between different types of particles.

made of charged particles (protons and other light ions, such as carbon), radiation therapy is called **hadrontherapy** or **charged particle therapy (PT)**.

The strength of hadrontherapy lies in the unique physical and radiobiological properties of these particles[3]: they can penetrate the tissues with little diffusion and deposit the maximum energy just before stopping (see figure 1.1). This allows a precise definition of the specific region to be irradiated. The peaked shape of the hadron energy deposition is called Bragg peak and has become the symbol of hadrontherapy. With the use of hadrons the tumor can be irradiated while the damage to healthy tissues is less than with X-rays.

The idea of using protons for cancer treatment was first proposed in 1946 by the physicist Robert Wilson, who later became the founder and first director of the Fermi National Accelerator Laboratory (Fermilab) near Chicago. The first patients were treated in the 1950s in nuclear physics research facilities by means of non-dedicated accelerators. Initially, the clinical applications were limited to few parts of the body, as accelerators were not powerful enough to allow protons to penetrate deep in the tissues.

In the late 1970s improvements in accelerator technology, coupled with advances in medical imaging and computing, made proton therapy a viable option for routine medical applications. However, it has only been since the beginning of the 1990s that proton facilities have been established in clinical settings, the first one being in Loma Linda, USA. Currently about thirty proton centers are either in operation or in construction worldwide. Although protons are used in several hospitals, the next step in radiation therapy is the use of carbon and other ions. These have some clear advantages even over protons in providing both a local control of very aggressive tumors and a lower acute or late toxicity, thus enhancing the quality of life during and after cancer treatment. Since the birth of hadrontherapy, more than 120,000 patients have been treated globally with hadrons, including 20,000 with carbon ions. In Europe, the interest in hadrontherapy has been growing rapidly and the first dual ion (carbon and protons) clinical facility in Heidelberg, Germany started treating patients at the end of 2009. Three more such facilities are now in operation: CNAO in Pavia, MIT in Marburg, and MedAustron in Wiener Neustadt are treating patients. Globally there is a huge momentum in particle therapy, especially treatment with protons.

In this chapter the main physical properties used for the therapy with charged particles and the quantities necessary to catalog the damage on the human body will be treated.

1.1 Radiation interaction with matter

To know how PT works is fundamental to introduce first some physical principles of charge particles interaction with matter, in particular (as explained in section 1.3) with biological tissues. The most important of these physical principles, such as loss of energy by ionization, dose released and angular straggling are described below.

1.1.1 Bethe-Bloch curve

Radiotherapy of deep-seated tumors requires ion beam ranges in tissue of up to 30 cm corresponding to specific energies up to 220 MeV/u for protons and helium ions, 430 MeV/u for carbon ions, and ~ 500 MeV/u for oxygen ions with particle velocities $\beta \equiv v/c \approx 0.7$. At these velocities the energy-loss rate dE/dx in the slowing-down process is dominated by inelastic collisions with the target electrons (electronic stopping) and can be well described by the *Bethe-Bloch formula*:

$$-\left(\frac{dE}{dx}\right) = 2\pi N_A r_e^2 m_e c^2 \cdot \frac{Z^2}{\beta^2} \cdot \frac{Z_{TG} \rho_{TG}}{A_{TG}} \cdot \left[\ln\left(\frac{2m_e c^2 \beta^2 \gamma^2 W_{max}}{I^2}\right) - 2\beta^2 - 2\frac{C}{Z_{TG}} - \delta(\gamma) \right] \quad (1.1)$$

where:

- $N_A = 6.022 \times 10^{23}$ is the Avogadro number.
- Z_{TG} is the target atomic number.
- A_{TG} is the target mass number.
- ρ_{TG} is the target density.
- $m_e = 0.510998 \text{ MeV}$ is the electron mass.
- $c = 2.998 \times 10^8 \text{ m/s}$ is the speed of light.
- $r_e = \frac{\alpha \cdot \hbar c}{m_e \cdot c^2} = 2.817 \times 10^{-13} \text{ cm}$ is the classical electron radius.
- Z is the unitary charge of the projectile.
- $\beta = v/c$ of the projectile.
- $\gamma = 1/\sqrt{1 - \beta^2}$ of the projectile.
- $W_{max} = \frac{4m_e M E_k}{(m_e + M)^2}$ is the maximum energy transferable in a collision (head on case) in which M is the incident particle mass and E_k its own initial kinetic energy.
- I is the ionization potential of the target and it has to be calculated using the quantum mechanical approach or empirically measured in experiments.
- C is the shell correction that must be included to consider electrons atomic binding.[4]
- δ is the density correction, in fact, as the particle energy increases, its electric field flattens and extends, so that the distant-collision contribution increases as $\ln(\beta\gamma)$. However, real media become polarized, limiting the field extension and effectively truncating this part of the logarithmic rise.[4]

Due to the $1/\beta^2$ dependence the energy loss increases with decreasing particle energy (as in figure 1.2). The energy loss increases also proportionally at the square of the charge Z of the impinging particle. At high velocities the atomic electrons are completely stripped off and the projectile charge is equal to the atomic charge number Z . At lower velocities (for light ions below about 10 MeV/u), the mean charge state decreases due to the interplay of ionization and recombination processes and Z in Eq. 1.1 has to be replaced by the effective charge Z_{eff} which can be described by the empirical formula[5]:

$$Z_{eff} = Z[1 - \exp(-125\beta Z^{-2/3})] \quad (1.2)$$

Bethe-Bloch formula expresses average energy losses, since it refers to processes of a stochastic nature. In other words, if n identical particles having all the same initial energy pass through the same portion of material in general they undergo different energy losses. Bethe's formula provides the average value of these energy losses while the fluctuations around the average value are described by the Landau distribution[6].

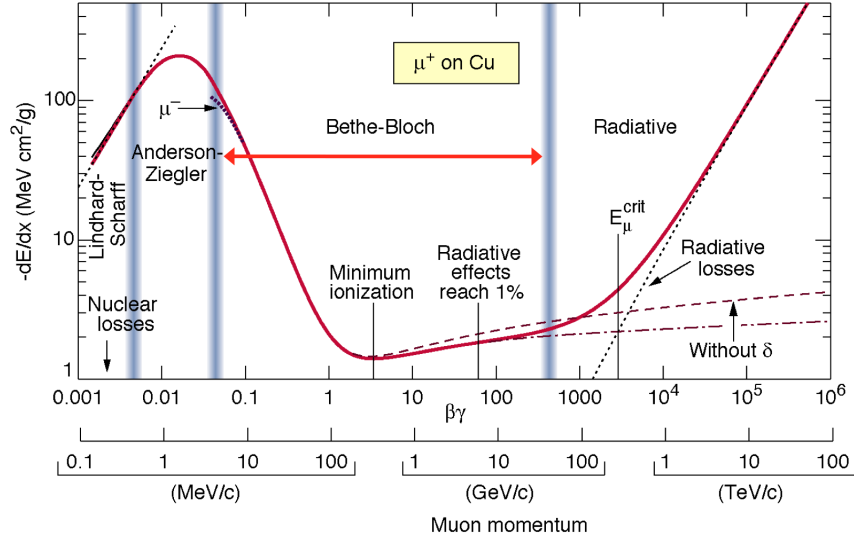


Figure 1.2. Total energy loss $-dE/dx$ for a muon in Copper target as a function of $\beta\gamma = p/Mc$. At low energy, the energy loss according to the Bethe-Bloch formula decreases approximately as $1/\beta^2$ with increasing energy. It reaches a minimum for approximately $\beta\gamma = 1$. For highly relativistic cases $\beta\gamma > 1$, the energy loss increases again, logarithmically due to the transversal component of the electric field. The dotted part on the right indicates the behavior of $-dE/dx$ for heavy charged particles, with or without density correction.[4]

1.1.2 Dose deposition and Bragg Peak

The *dose* deposited in tissue is the most important physical quantity in radiotherapy. It is defined[39] by the term *absorbed dose* (unit Gray [1Gy=1J/kg]) as the mean energy $d\epsilon$ deposited by ionizing radiation in a mass element dm .

$$D = \frac{d\epsilon}{dm} \quad (1.3)$$

In radiation therapy (RT) water is used as tissue reference medium because human body is $\sim 70\%$ composed by this element. Dose measurements are normally performed with air-filled ionization chambers and have to be converted to the absorbed dose in water by correction factors. For a parallel beam with particle fluence F the dose deposited in a thin slice of an absorber material with mass density ρ can be calculated as follows:

$$D[\text{Gy}] = 1.6 \times 10^{-9} \times \frac{dE}{dx} \left[\frac{\text{keV}}{\mu\text{m}} \right] \times F[\text{cm}^{-2}] \times \frac{1}{\rho} \left[\frac{\text{cm}^3}{\text{g}} \right] \quad (1.4)$$

where dE/dx is the energy loss of the particles per unit path length (*stopping power* as explained in section 1.1.3).

The main reason for using heavy charged particles in radiotherapy, as already mentioned in the introduction, is their favorable depth-dose profile (*Bragg curve*) named after Sir William Henri Bragg who investigated the slowing down of α particles in air[6]. Many years later Wilson proposed the application of protons and heavier

ions for precision exposures in radiotherapy. A comparison of depth-dose profiles for electromagnetic radiation X-rays, electrons and protons in water is displayed in figure 1.3. Low-energy X-rays and specially electrons show a steep exponential decrease of dose with depth (absorption law). For higher energy photons, mostly used in conventional therapy nowadays, the initial dose buildup, mainly caused by forward scattered Compton electrons, shifts the peak dose by a few centimeters away from the surface of the patient's body, thereby improving the target-to-entrance dose and sparing the radiosensitive skin. In contrast to photons, the dose profiles

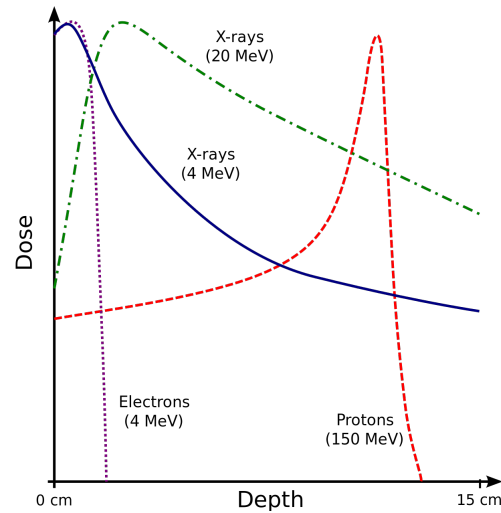


Figure 1.3. Depth-dose profiles of X-ray radiation, electrons and protons in water.[41]

of protons and heavier ions are characterized by a distinct narrow peak at the end of their path given the dependence on $1/\beta^2$ in formula 1.1. The position of this peak can be precisely adjusted to the desired depth in tissue by changing the kinetic energy of the incident ions.

On average the extension of a tumor is greater than the size of the Bragg peak and therefore more beams are needed to irradiate it. The technique employed in PT to cover a region broader than the Bragg peak is shown in figure 1.4. A series of beams (^{12}C in the case displayed) with the same direction but different energies and intensities are delivered onto the patient, releasing a total dose profile usually called *Spread-Out Bragg Peak (SOBP)*. Obviously, this approach relies on a precise knowledge of the range of the particle (see section 1.1.4). Small modifications could either lead to an incomplete irradiation of the tumor or move one of the BPs over a healthy region.

1.1.3 Stopping Power and Linear Energy Transfer (LET)

Closely related to the formula of Bethe-Bloch is the concept of *stopping power*, defined as the retarding force acting on charged particles, due to interaction with matter, resulting in loss of particle energy[6].

$$S(E) = -\frac{dE}{dx} \quad (1.5)$$

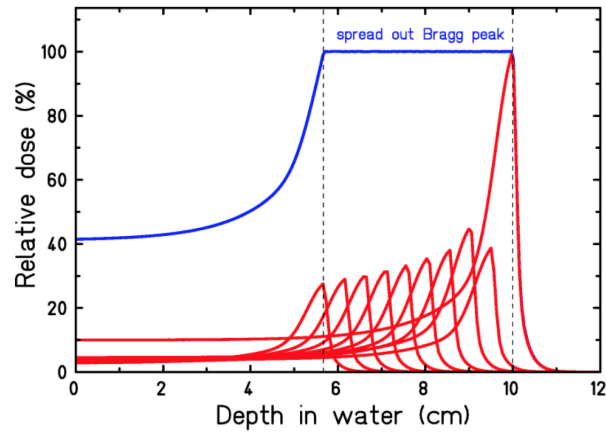


Figure 1.4. Example of Spread-Out Bragg Peak (SOBP) made by ^{12}C beams with energy in a range between 102 MeV/u and 110 MeV/u.[41]

Stopping power depends on the type and energy of the radiation and on the properties of the material it passes. It is numerically equal to the loss of energy E per unit path length, x . The equation 1.5 defines the *linear stopping power* (expressed in the

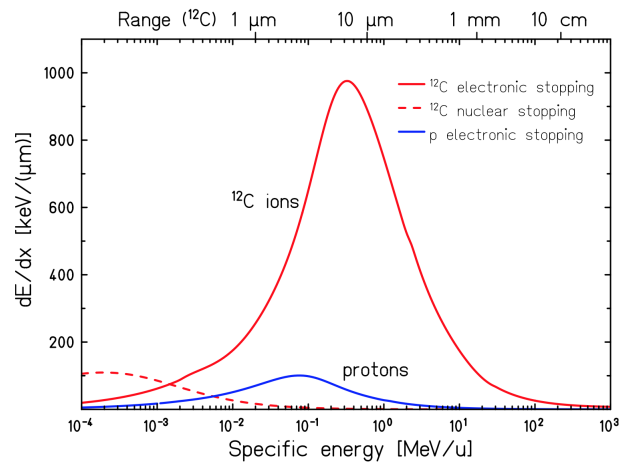


Figure 1.5. Energy loss dE/dx in function of the kinetic energy per nucleon (specific energy) of ^{12}C ions and protons in water. The range of ^{12}C ions in water corresponding to their specific energy is indicated at the top.[7]

SI in Newton). If a substance is compared in gaseous and solid form, then the linear stopping powers of the two states are very different because of their different density. So usually the force is divided by the material density to obtain the *mass stopping power* which in the international system is expressed in m^4/s^2 . The mass stopping power then depends only very little on the density of the material. Stopping power curves for protons and ^{12}C ions in water are shown in figure 1.5.

The secondary electrons produced during the process of ionization by the primary charged particle are conventionally called δ rays, if their energy is large enough so that they themselves can ionize. Usually the focus is upon the energy transferred

in the vicinity of the primary particle track and therefore exclude interactions that produce δ rays with energies larger than a certain value Δ . This energy limit is meant to exclude secondary electrons that carry energy far from the primary particle track, since a larger energy implies a larger range (see section 1.1.4). This approximation neglects the directional distribution of secondary radiation and the non-linear path of δ rays, but simplifies analytic evaluation.

Restricted *linear energy transfer* (LET is the amount of energy that an ionizing particle transfers to the material traversed per unit distance) is defined by

$$LET_{\Delta} = \frac{dE_{\Delta}}{dx} \quad (1.6)$$

where dE_{Δ} is the energy loss of the charged particle due to electronic collisions while traversing a distance dx , excluding all secondary electrons with kinetic energies larger than Δ . If Δ tends toward infinity, then there are no electrons with larger energy, and the linear energy transfer becomes the unrestricted linear energy transfer which is identical to the linear electronic stopping power.

1.1.4 Range and angular straggling

Another fundamental parameter in PT is the beam *Range* defined as the path that a particle of the beam can make in average inside the target material before stopping. It is possible to distinguish two different types of ranges:

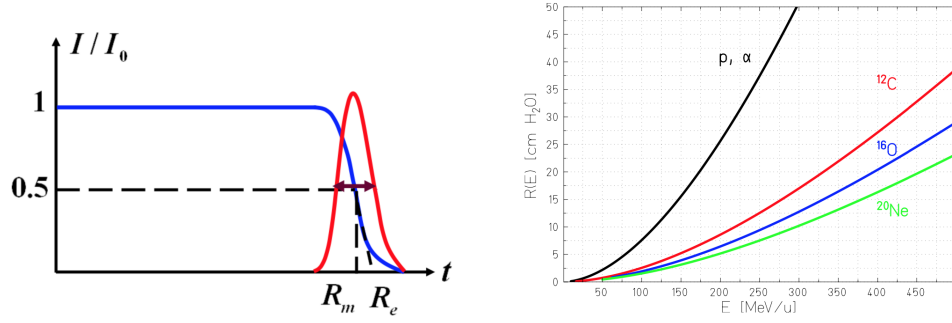
- *CSDA Range* is an approximation of the effective length of the path traveled by the particle under consideration, taking into account the scattering due to the medium crossed
- *Projected Range* is the distance between the point where the particle enters the medium and the point where it is absorbed (or ends its energy), projected on the original "travel" direction. This quantity is always less than the CSDA range.

For heavy charged projectiles as the ions used in hadrontherapy CSDA Range and Projected one are nearly the same thing because heavy ions are very little scattered and travel almost on a straight line. Considering energy deposition in a portion of material dx as $dE = \frac{dE}{dx} \cdot dx$ it is possible to write $dx = \left(\frac{dE}{dx}\right)^{-1} \cdot dE$ and so Range is obtainable integrating this quantity on all the available energy:

$$R(E) = \int dx = \int_0^E \left(\frac{dE}{dx}\right)^{-1} \cdot dE \quad (1.7)$$

The range of ions with the same specific energy scales with a factor of A/Z^2 (figure 1.6 (b)).

Statistical fluctuations of the energy loss in the large number of collisions of the slowing-down process result in a broadening of the Bragg peak for an ion beam consisting of many particles. These fluctuations are described by the asymmetric Vavilov distribution for charged particles passing through a thin layer of matter



(a) Relative beam intensity and (b) Mean range of heavy ions in water.[7] straggling.[7]

Figure 1.6

(energy-loss *straggling* figure 1.6 (a)). In the limit of many collisions the Vavilov distribution[6] becomes a Gaussian:

$$f(\Delta E) = \frac{1}{\sqrt{2\pi}\sigma_E} \exp\left(-\frac{(\Delta E - \langle \Delta E \rangle)^2}{2\sigma_E^2}\right) \quad (1.8)$$

with

$$\sigma_E = 4\pi Z_{eff} Z_t e^4 N \Delta x \left[\frac{1 - \beta^2/2}{1 - \beta^2} \right] \quad (1.9)$$

The variance σ_R^2 of the range straggling is related to the variance σ_E^2 of the energy-loss straggling by

$$\sigma_R^2 = \int_0^{E_i} \left(\frac{d\sigma_E}{dx} \right) \left(\frac{dE}{dx} \right)^{-3} dE \quad (1.10)$$

The ratio of straggling width σ_R and mean range R is nearby constant and can be described by

$$\frac{\sigma_R}{R} = \frac{1}{\sqrt{M}} f\left(\frac{E}{Mc^2}\right) \quad (1.11)$$

where f is a slowly varying function depending on the absorber and E and M are the particle energy and mass. Because of the $1/\sqrt{M}$ dependence straggling is smaller for heavier ions than for protons. So the profile of the Bragg peaks is broader, mainly due to the density inhomogeneities of the penetrated tissue. Furthermore, for scanning beam delivery systems using slice-by-slice irradiation of the target volume, it can be even advantageous to widen the sharp Bragg peaks by passive systems in order to reduce the treatment time[7].

The small lateral deflection of heavy ions penetrating through an absorber is a particular advantage of heavy ions in comparison to protons and is of clinical relevance for treatments near organs at risk (*OAR*). The beam spread is mainly caused by elastic Coulomb interactions with the target nuclei, while scattering due to electronic interactions, which dominate the stopping process, can be neglected. The statistical distribution function $F(\theta, d)$ for the resulting scattering angle θ at penetration depth d has an analytical solution given by Molière for a shielded Coulomb potential. For small angles the higher-order terms in Molière's solution

can be neglected and the angular distribution can be approximated by a Gaussian function with a standard deviation given by:

$$\sigma_{\theta}[\text{rad}] = \frac{14.1 \text{ MeV}}{\beta pc} Z_p \sqrt{\frac{d}{L_{rad}}} \left[1 + \frac{1}{9} \log_{10} \left(\frac{d}{L_{rad}} \right) \right] \quad (1.12)$$

The absorber material is characterized by the thickness d and the radiation length L_{rad} . The value of L_{rad} for the most common compound (H_2O) is 36.08 g/cm^2 [9]. Targets containing heavy elements cause a larger angular spread than targets of light elements with the same thickness.

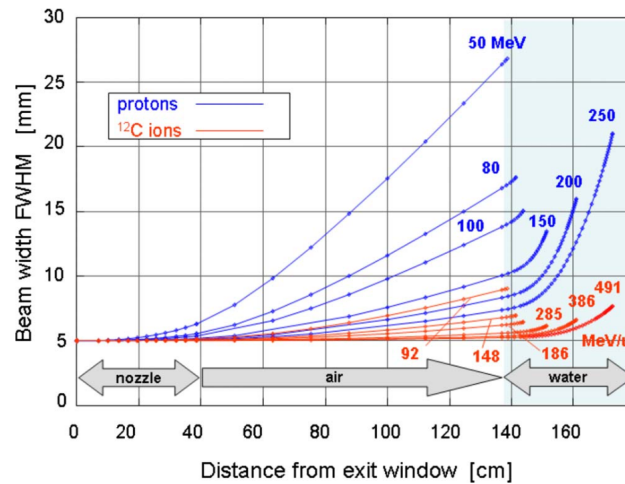


Figure 1.7. Calculated beam spread for ^{12}C ions and protons in a typical treatment beam line. It was assumed that an initially parallel particle beam (5 mm full width at half maximum) passes through the nozzle (including a thin vacuum window and beam monitors) and enters a water absorber (patient) at 1 m distance from nozzle exit. At small depth (i.e., small particle energies) the width is mainly determined by scattering in the nozzle, while at higher energies the scattering in the water absorber dominates. Carbon ions show a much smaller spread than protons at the same penetration depth.[7]

Multiple small angle deviations along the particle path, in total, lead to a change in particle directions that result in a visible deviation in primary path. The lateral broadening of beam due to multiple scattering is often called *lateral scattering*. Clinical measurements and calculations on lateral scattering and also energy straggling have often been done for water or soft tissues.[8] It should be kept in mind that two different contributions to the angular beam spreading have to be considered:

1. Scattering caused by materials in front of the patient (vacuum exit window, beam monitor, beam shaping devices).
2. Scattering in tissue between entrance point and stopping depth.

At low energies 1) represents the dominant contribution because even a small angular spread translates in a significant broadening of the beam spot due to the traveling distance of typically 0.5–1.0 m before entering the patient. Therefore the material in the beam path in front of the patient should be kept as thin as possible, not contain

heavy elements, and be located as close as possible towards the patient. At higher energies contribution 1) becomes less important or even negligible while 2) increases due to the larger penetration depths in tissue. The calculations shown in figure 1.7 demonstrate the much smaller beam spread of ^{12}C ions compared to protons.

1.2 Nuclear Fragmentation

While the stopping process of high-energy (hundreds of MeV/u for PT application) ions slowing down in matter is dominated by the inelastic collisions with the atomic electrons, the probability of nuclear reactions, even if much smaller, leads to significant effects at large penetration depths. At energies of several hundred MeV/u violent nuclear spallation reactions may result in a complete disintegration of both projectile and target nuclei (e.g., in central head-on collisions) or in partial fragmentations.[10] The nucleus-nucleus collisions can be schematically described as follows, as shown in

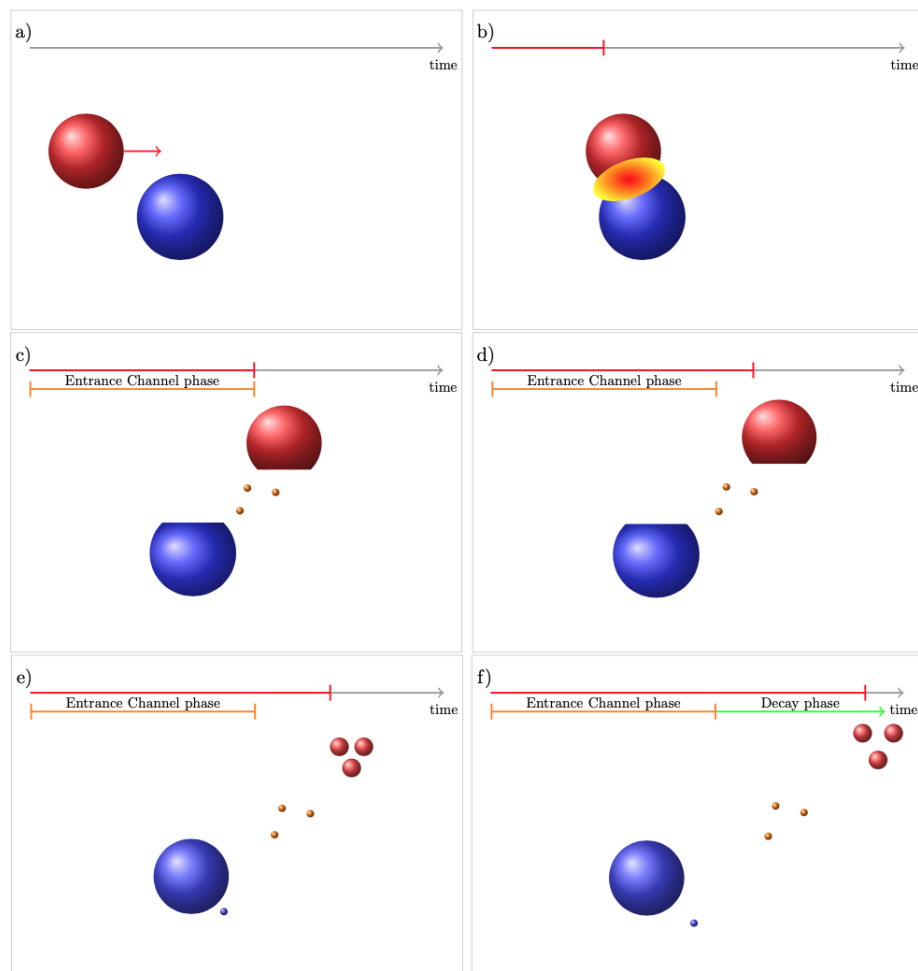


Figure 1.8. Schematic view of a nucleus-nucleus collision[41].

figure 1.8. When a projectile hits a target nucleus (panels a) and b)), light particles are promptly emitted and an excited quasi-projectile and an excited quasi-target

are formed (panel c)). These excited nuclei decay through consecutive light particle emissions (“evaporation” process) or by a simultaneous break-up (“fragmentation” process). The first step of this description is called the “entrance channel phase” (panels a),b) and c)) and the second step is called the “decay phase” (panels d),e) and f)). For both steps, several models have been developed, strongly dependent on the center-of-mass energy of the system. A complete nucleus-nucleus collision modeling is achieved by a combination of a model describing the entrance channel and a model describing the decay phase.

Some important conclusions can be drawn for the effects of fragmentation relevant to radiotherapy with high-energy ion beams:

1. Nuclear reactions cause a loss of primary beam particles and a build-up of lower-Z fragments, these effects becoming more and more important with increasing penetration depth.
2. The secondary (or higher-order) projectile-like fragments are moving with about the same velocity as the primary ions. They have in general longer ranges and produce a dose tail beyond the Bragg peak.
3. The angular distributions of the projectile fragments are mainly determined by reaction kinematics and forward directed, but much broader than the lateral spread of the primary ions caused by multiple Coulomb scattering.
4. The target fragments and the decay and evaporation products (essentially protons, neutrons and pions) are isotropically distributed in space and have a low kinetic energy and therefore small range, which is why they are not generally treated as a major problem in dose distributed in an hadrotherapy treatment with ions with $Z > 1$.

1.2.1 Influence of nuclear reactions on delivered dose

The figure 1.9, from GEANT4 simulations[11], shows the ratio of projectiles which have not experienced a nuclear collision on a nucleus of the absorber with respect to the penetration depth for 150 MeV proton in liquid water (left panel) and the Bragg Curve (the evolution of LET per incident proton with the penetration depth) for 150 MeV protons in liquid water (right panel). On both panels, the black curve corresponds to simulations in which the nucleus-nucleus collision process has been deactivated (there is only electro-magnetic interaction) and the red curves to simulations in which the nucleus-nucleus collision process has been activated (there are electro-magnetic and nuclear interactions). The effect of the projectile consumption is clearly seen on figure 1.9. Whereas all projectiles reach the Bragg Peak for electro-magnetic interaction simulations, only 80% of them reach for nuclear interaction simulations. As a consequence, the energy deposition at the Bragg Peak (see left panel of fig 1.9) is reduced by 20% for nuclear collisions compared to electro-magnetic collisions. Nuclear collisions have no effect on the location of the Bragg Peak which is driven by the Bethe-Bloch equation only.

Secondary fragments are issued from the target only. Their velocity is very small and hence their range do not exceed few micro-meters. They deposit their energy close to the collision location. The indirect effect lies in the total amount of energy which has

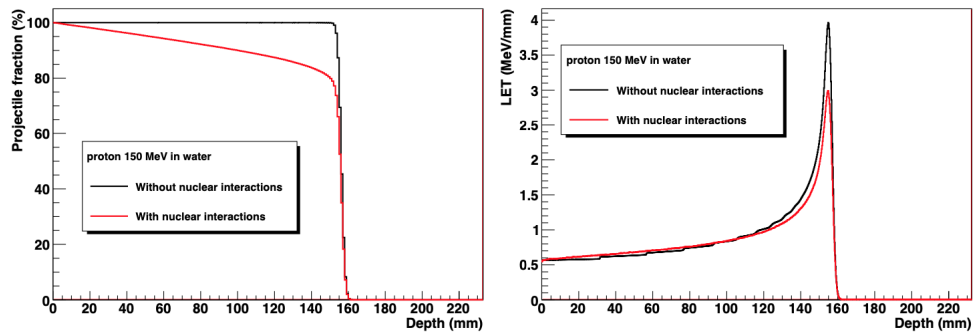


Figure 1.9. Evolution of the primary protons ratio (left panel) and the mean LET for protons (right panel) with the penetration depth for 150 MeV protons according to GEANT4 simulations.[41]

been deposited in the absorber. Since some energy is needed to produce fragments, each time a proton collides on a nucleus, one part of the total energy of the system is exhausted in the particle production. As a result, the integral of the Bragg Curve for nuclear interaction simulations is $\sim 97\%$ of the projectile total energy. The same integral is equal to the projectile incident energy for electro-magnetic simulations. The influence of the nucleus-nucleus reactions on the dose deposition for ^{12}C ions

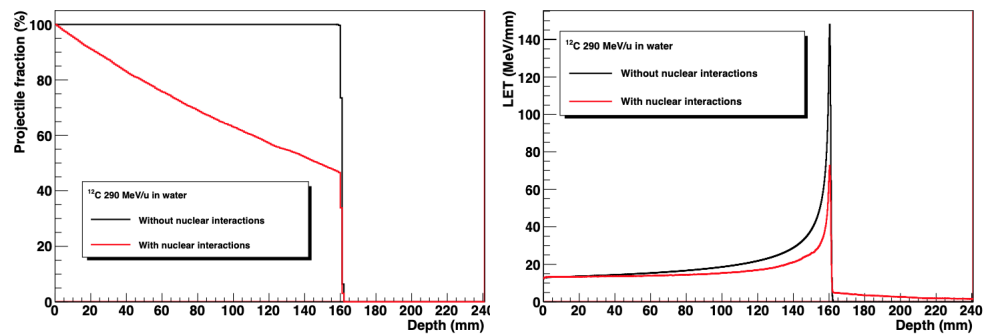


Figure 1.10. Evolution of the primary ^{12}C ions ratio (left panel) and the mean LET for with ^{12}C ions (right panel) with the penetration depth.[41]

can be observed on figure 1.10 which has been obtained for 290 MeV/u ^{12}C ions using the GEANT4 simulation framework. Only 50% of projectiles reach the Bragg Peak (see left panel of figure 1.10), leading to a reduction of 50% on the energy deposition per incident ^{12}C at the Bragg Peak (right panel of figure 1.10).

The ratio of ^{12}C ions which do not experience a nuclear interaction decreases exponentially with respect to the penetration depth. As for protons, the locations of the Bragg Peaks are identical for electro-magnetic and nuclear simulations. The $\int LET(x)dx$ integral is equal to $\sim 93\%$ of the incident energy for nuclear simulations. The difference compared to protons is the energy deposition tail beyond the Bragg Peak. As for protons, the fragments emitted by the target nucleus have a very short range and deposit their energy close to the collision location. The fragments

emitted by the fragmenting projectile have a velocity close to the projectile velocity and hence, due to the A/Z^2 scaling of the ranges, they will travel a longer path before stopping. In particular, the lighter fragments will have a much longer range with respect to the primary ions. The overall effect of the longer range of projectile fragments is a tail in the depth-dose profile, as shown in the right panel of figure 1.10, also called the **fragmentation tail**.

These simulations show clearly that the dose map is significantly changed when the nucleus-nucleus collisions are taken into account.

1.2.2 Reaction cross section and its impact on dose deposition computation

In physics, the *cross section* is a measure of probability that a specific process will take place in a collision of two particles. Its unit of measure is m^2 or most commonly *barn* [$1\text{barn} = 10^{-24}\text{cm}^2$].

The occurrence of a nucleus-nucleus collision is driven by the total reaction cross section σ_R . The number $N_{\text{reactions}}$ a beam of fluence $f = N/S$, with S section of the beam and N the number of projectiles, will experience crossing a thin target of thickness dx , in the hypothesis in which multiple collisions per particle can be neglected, is:

$$N_{\text{reactions}} = f \cdot N_t \cdot \sigma_R \quad (1.13)$$

where $N_t = (N_A/M_{\text{mol}}) \cdot \rho S dx$ is the number of nuclei in the fraction of target crossed by the beam, N_A is the Avogadro's number, ρ the material density and M_{mol} the material molar mass. The variation dN of the number of projectiles which remain unchanged after a path of length dx is $dN = -N_{\text{reactions}}$, which leads to:

$$N(x) = N_0 e^{-x/\lambda} \quad (1.14)$$

with

$$\lambda = \frac{M_{\text{mol}}}{N_A \rho \sigma_R} \quad (1.15)$$

The exponential decrease of the number of projectiles with the path length is directly driven by the total reaction cross section σ_R .

In order to understand how much the experimental knowledge of the reaction cross section impact on the energy released computed by a simulation let's consider figure 1.11 (b). In figure 1.11 (b) the average LET as a function of the penetration depth of ^{12}C ions in a stack of materials (skin, cranium, brain white matter, cancerous tumor) has been obtained with a GEANT4 simulation. The incident energy distribution has been determined to have a SOBP from 6 cm to 7 cm which corresponds to the tumor size. The corresponding mean LET curve is the black one. Two others simulations have been performed by increasing all the cross section values by 10% (blue LET curve on figure 1.11 b) or by decreasing all the cross section values by 10% (red LET curve on figure 1.11 b). It is observed that this variation of $\pm 10\%$ on the cross sections values induces a variation of $\pm 3\%$ on the LET value in the tumor region. This implies that the reaction cross sections have to be known within 10% to achieve a 3% accuracy on the dose computation.

Typical values for various ions and the corresponding mean free paths in water are shown in table 1.1.

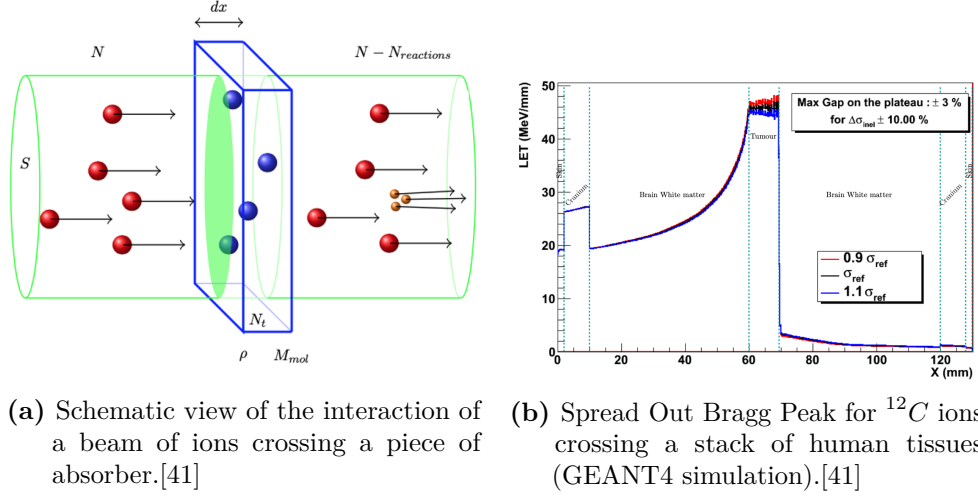


Figure 1.11

Ion	E (MeV/u)	σ_R (mb)	λ (cm)
p	200	352	85.2
^4He	200	767	38.6
^{12}C	380	1424	20.8
^{20}Ne	530	1929	15.5

Table 1.1. Total reaction cross section σ_R and mean free path in H_2O of high-energy ions with about 25 cm range.[12]

1.2.3 Role of secondary fragments

The contribution of secondary particles is twofold. Firstly, a part of the initial kinetic energy of the projectile is exhausted to produce secondary fragments. When a projectile of mass excess $\Delta m(A_p, Z_p)$ with a kinetic energy T_p hits a target nuclei of mass excess $\Delta m(A_t, Z_t)$ and produces a set of fragments of mass excesses $\Delta m(A_i, Z_i)$ and kinetic energies T_i , the energy conservation law reads:

$$\Delta m(A_p, Z_p)c^2 + T_p + \Delta m(A_t, Z_t)c^2 = \sum_i [\Delta m(A_i, Z_i)c^2 + T_i] \quad (1.16)$$

by introducing the mass balance

$$Q = \Delta m(A_p, Z_p)c^2 + \Delta m(A_t, Z_t)c^2 - \sum_i \Delta m(A_i, Z_i)c^2 \quad (1.17)$$

the equation 1.16 becomes:

$$\sum_i T_i = T_p + Q \quad (1.18)$$

For small charge number systems ($Z < 26$) the mass balance is negative so the sum of the kinetic energies of the produced fragments is smaller than the projectile's kinetic

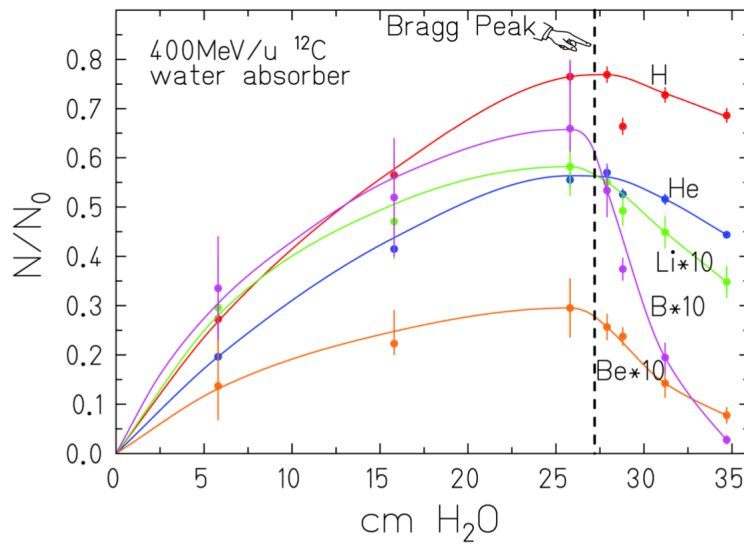


Figure 1.12. Experimental evolution of the mean secondary fragment multiplicities with the penetration depth in liquid water for 400 MeV/u ^{12}C ions. Note that the multiplicities of Li, Be and B isotopes have been multiplied by 10 to be visible on the figure[13].

energy. The second type of contribution of secondary particles to the dose map is the energy they will deposit in the target material. As already seen, the particles produced by the quasi-projectile will contribute to the fragmentation tail beyond the Bragg Peak. But since they are produced all along the projectile path, they will also deposit a fraction of their energy before and at the Bragg Peak. The mean LET at depth x is then the weighted sum of all mean LET's of all particles present at depth x :

$$\langle LET(x) \rangle = \sum_i \nu_{A_i, Z_i}(x) \langle LET_{A_i, Z_i}(x) \rangle \quad (1.19)$$

where $\nu_{A_i, Z_i}(x)$ is the multiplicity of fragments with charge number Z_i and mass number A_i at depth x per incident projectile and $\langle LET_{A_i, Z_i}(x) \rangle$ is their mean LET at depth x . The figure 1.12 shows the measured evolution of the multiplicity of different fragment type per incident ion with respect to the penetration depth in liquid water for 400 MeV/u ^{12}C ions. Behind the Bragg Peak (indicated by the dashed vertical line), the multiplicities of secondary fragments increase with the penetration depth as expected. Beyond the Bragg Peak these multiplicities decrease with the depth. The maximum multiplicities are reached at the Bragg Peak.

According to the Bethe-Bloch equation the mean LET scales roughly like Z^2 for particles having the same velocity. As a consequence, the mean LET value at depth x is dominated by the mean LET of the carbon projectile. The contribution of the hydrogen and helium isotopes to the mean LET remains weak even if their multiplicity is high. The contribution of heavier secondary particles to the mean LET is weak due to their low relative multiplicities. Instead beyond the Bragg Peak, the mean LET is dominated by the contributions of the hydrogen and helium isotopes. An estimation of the contribution of secondary particles to the mean LET

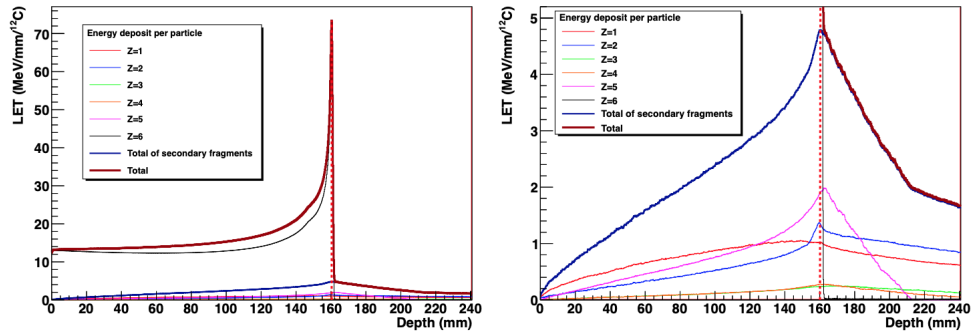


Figure 1.13. Mean LET value of secondary fragments for ^{12}C ions at 290 MeV/u (GEANT4 simulations). The right panel is a zoom on the right panel on low LET values.[41]

value can be seen on the figures 1.13. The right panel of this figure is a magnification of the figure displayed on the left panel on low LET values. These figures show the mean LET value of all particles with respect to the penetration depth in liquid water. This has been obtained with the GEANT4 framework for a 290 MeV/u ^{12}C ion. It is clear that, the specific choice of the nuclear collision model selected in GEANT4 to describe the nucleus-nucleus collision has an influence on the computation of the dose that, as already mentioned, depends on the reaction cross section values. Indeed, the relative multiplicity of secondary particles may change from a model to another and hence modify the evolution of the mean LET with the penetration depth.

1.3 Biological Effectiveness

The basic principle of any type of radiotherapy is to use ionizing radiation to damage tumor cells. The aim is to kill these cells (directly or by apoptosis) or, at least, interrupt their ability to reproduce. Thus, the actual target of radiation therapy is to damage DNA of cancer cells. DNA damage is usually referred to as:

- *Direct* when particles ionize the DNA molecule, breaking one or both of its chains.
- *Indirect* when DNA gets damaged by chemical reactions with unstable molecules, called free radicals, generated by the beam traveling inside cells.

The ionizing radiation effects depend mostly on the LET values. Depending on the incident beam energy, direct (high LET) and indirect (low LET) hits are observed. In general the ionization events generated by low LET radiations (particles with an energy value around $0.2 - 0.5\text{keV}/\mu\text{m}$, i.e. photons emitted by ^{60}Co source) are quite separate from each other (see figure 1.14). For this reason, these particles are indicated as sparsely ionizing. Instead the high LET radiations (particles with energy value of the order of $100\text{keV}/\mu\text{m}$, i.e. carbon ions) are called densely ionizing.

The severity of the damage is directly linked to the type of lesion induced by the particles on the DNA helix (see figure 1.15). It is usually classified as:

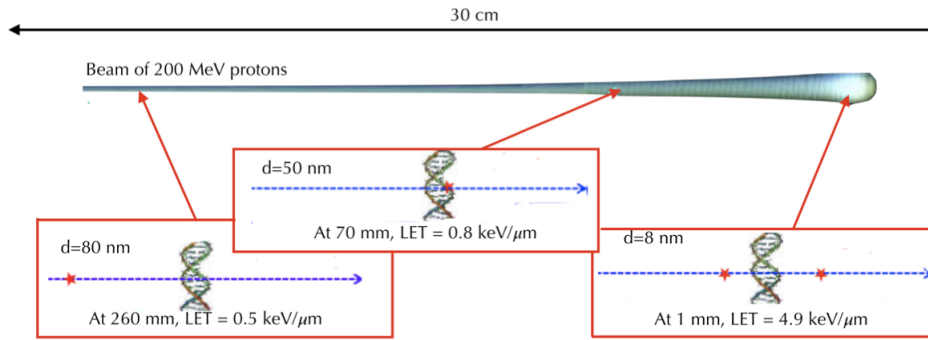


Figure 1.14. Ionization density for different distance from the Bragg Peak placed at 30 cm of penetration depth. The data are obtained considering a proton ion beam at 200 MeV that crosses a water target. d indicates the distance between two consecutive ionization events.

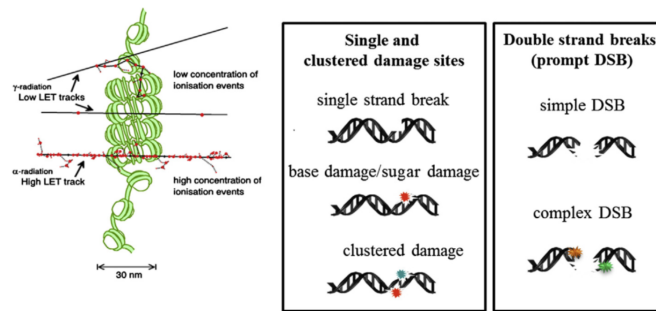


Figure 1.15. Example of low/high LET interactions and different types of DNA damage[14].

- *Single Strand Break (SSB)*: the lesion is confined to only one of the two strands, breaking it into two pieces. This type of damage has low biological impact because cells are able to repair most of these fractures without consequences. SSBs are the main kind of breaks induced by X-rays.
- *Double Strand Break (DSB)*: in this case both of the DNA strands are broken, either at the same level or at a distance of few DNA base pairs. These type of lesions are very difficult to repair and usually result in cell death. Heavy charged particles mainly cause DSBs when interacting with cells.
- *Clustered damage*: in this case, the beam induces multiple DNA lesions, but at a distance of few tens of base pairs. The outcome of these interactions mainly depends on the position of ionized DNA sites.

1.3.1 Linear-Quadratic model

One of the most common models used in clinical radiation therapy to link dose and cell damage is the *linear-quadratic model*:

$$S_{fx}(D) = e^{-\alpha D - \beta D^2} \quad (1.20)$$

where D represents the physical dose and S the surviving fraction of cells. In the standard experimental protocol, cell proliferation is analyzed about 1-2 weeks after irradiation and cells are counted as survivors, if they have formed a colony with more than 50 daughter cells. The α and β parameters (in particular their ratio R), which can vary depending on targeted tissue and type of radiation, are used to define the radiosensitivity of the exposed region. Low R ratio is associated with a prevalence of repairable damage, while high R value is related to a severe non repairable damage[15]. Both cases are presented in figure 1.16: ions with high energies have also high velocity, so the LET is low and the ionization density is small. In this case the damage caused by the ions can be repaired more frequently and

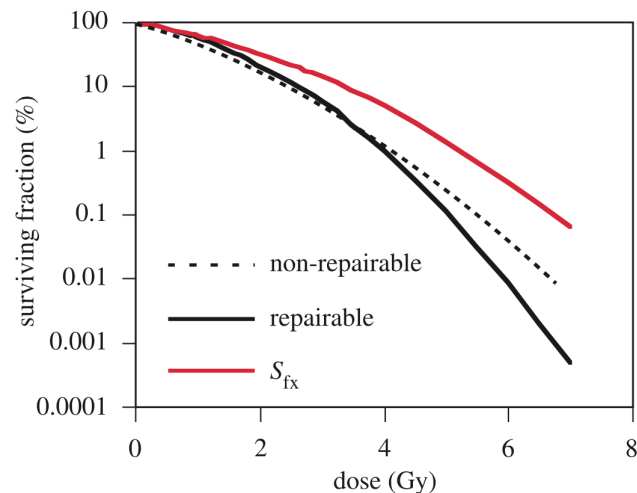


Figure 1.16. Cell survival curve illustrating the surviving fraction of cells after a single dose of radiation. The repairable and non-repairable components are also shown.[15]

the survival curve (black in figure 1.16) present a small shoulder. When the initial energy decreases, the LET increases. Therefore ions have a higher ionization density leading to a higher probability to produce unreparable damages (dotted curve). Empirical tests determine that DNA repair mechanisms of tumor cells are significantly less effective than those of normal healthy cells (i.e. tumor cells exhibit low values of β [15]). This effect is exploited by ‘fractionating’ the radiation treatment into a succession of small doses, typically one dose-fraction a day for 6–7 weeks. After each fraction the normal healthy cells are able to repair some of the radiation damage whereas the tumor cells are unable to repair the damage, leading to compounded decimation with each new fraction. The fractionation is optimized when maximum cancer cell sterilization is achieved with minimal damage to normal tissues. Determining the optimal trade-offs between dose per fraction, time interval between fractions and total treatment dose is the subject of a great deal of current research[15].

1.3.2 Relative Biological Efficiency factor (RBE)

The main advantage of the PT lies in the biological effects induced by the charged particles, coupled to the high spatial selectivity in the dose release, explained by the

Bethe theory (section 1.1). To kill the same amount of cells lower doses are needed compared to X-rays. This effect is parametrized by the *Relative Biological Efficiency factor* (labeled RBE). It is defined as the ratio of the dose D_γ needed to kill a given amount of cells for X-rays to the dose D_{part} needed to kill the same amount of cells for the particle under interest:

$$RBE_{iso} = \frac{D_\gamma}{D_{part}} \quad (1.21)$$

The RBE is the most important quantity in biological treatment planning of heavy-ion therapy. The photon-equivalent dose, D_γ , sometimes abbreviated as biological dose, quantifies the dose of conventional radiation that would yield the same biological effect as the applied radiation[16]. Figure 1.17 shows different survival curves (the

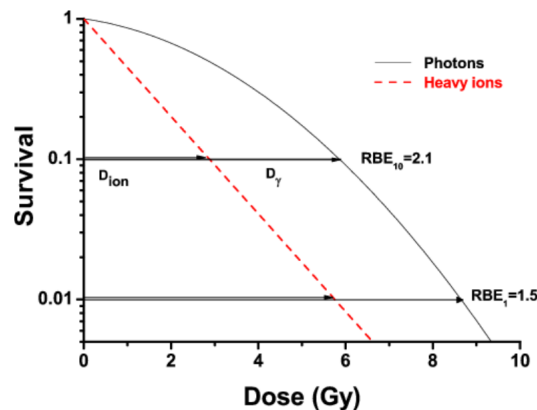


Figure 1.17. Survival curves and determination of RBE for cell inactivation for 10% and 1% survival level for a typical heavy ion irradiation[17].

rate of surviving cells with respect to the dose) for photons (full line) and for heavy ions (dashed line): depending on the survival rate, the RBE can range from 1.5 (1% surviving cell) to 2.1 (10% surviving cell). RBE strongly depends on the ion employed and for each ion can range in an interval dependent on the delivered dose. The average RBE is around 1.1 for protons. The assumed RBE value for carbons is around 3: the mixed radiation field due to the build-up of secondary fragments makes no easy the contribution of such fragments to the overall dose and so the RBE computation.

As aforementioned, the response of cellular system depends also on the LET of the penetrating particle. In Figure 1.18 a compilation of different cell survival experiments with V79 hamster cells (a frequently used cell line in radiobiology laboratories) reveals that the RBE increases with LET up to an ion-dependent maximum value and decreases for higher LET values. According to the higher ionization density in the track center of particles with a larger LET, the radiation damage is more severe, thus increasing the RBE. However, at a certain LET value the dose deposition is so large that a single-particle traversal sufficiently reduces the cell survival probability. In that case, the additional dose deposited by ions with a larger LET is wasted and we would not expect a larger RBE. Moreover,

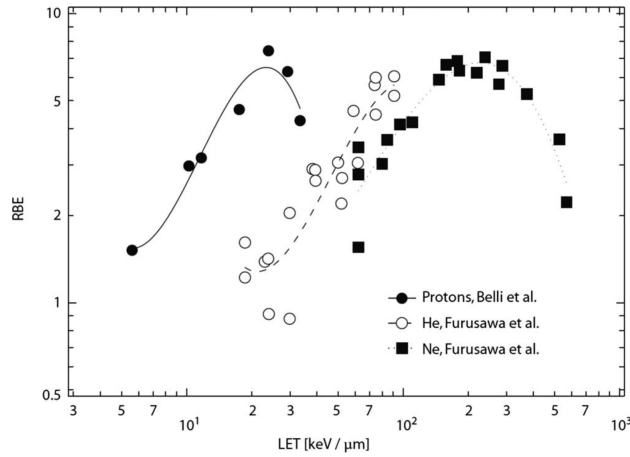


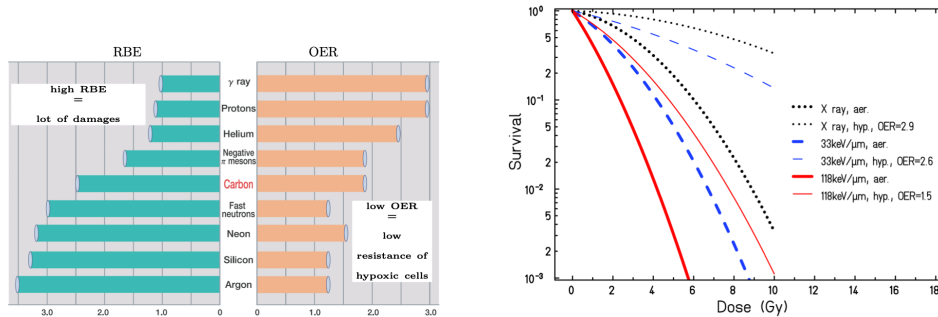
Figure 1.18. Dependence of $RBE_{\alpha} = \alpha_{ion}/\alpha$ on LET and particle type, where α and α_{ion} are the linear part of the survival curve for photons and ions, respectively[18].

the RBE decreases due to the lower hitting probability, since the number of ions required for the same dose deposition is lower for particles with a higher LET. As a consequence, the ratio of cells without any particle hit (obviously being survivors) increases resulting in a lower RBE for cell killing.

For heavier particles, the position of the RBE maximum is typically shifted to higher LETs.

1.3.3 Oxygen effect

Another biological effect is the so called *Oxygen effect*: the cells with a low oxygenation rate (hypoxic cells) are more resistant to radiations than cells with a normal oxygenation rate (normoxic or aerobic cells). As a consequence, more dose is needed to destroy hypoxic cells. Unfortunately, resistant hypoxic cells are located in the cancer tumors.



(a) RBE (left) and OER (right) values of different particles. (b) Influence of the oxygen level on cell survival of human kidney T-1 cells for carbon ions with different LET[17].

Figure 1.19

This effect is parametrized by the Oxygen Enhancement Ratio (OER) which is defined as follows:

$$OER = \frac{D_{hypoxic}}{D_{aerobic}} \quad (1.22)$$

where $D_{hypoxic}$ is the dose needed for heavy ions to kill a fixed amount of hypoxic cells and $D_{aerobic}$ is the dose needed to kill the same amount of aerobic cells.

The figure 1.19 b shows the survival curve for particles with different Linear Energy Transfer (LET) values for aerobic cells (full lines) and hypoxic cells (dashed lines). The OER value clearly depends on the LET value. For X-rays the OER value is around 3. For particles with low LET values like carbon ions at high energies, the OER value is around 2.6. For high LET values like carbon at low energies (close to the Bragg peak), the OER value decreases down to 2. RBE and OER values are summarized on figure 1.19 a. One can see that the main improvement in using protons for radiation therapy is the ballistics of protons since the RBE value is only 1.1 and the OER value is close to the OER value of γ rays.

For ions heavier than neons the OER value is close to one: the oxygen effect has almost disappeared. A major improvement in radiation therapy may be achieved by using heavy ions: less dose is necessary to kill cancerous cells and no additional dose is needed to kill hypoxic radio-resistant cells. Using heavy ions, however, implies a significant increase in the fragmentation generated (an effect that for PT must be absolutely avoided in order not to incur collateral damage), this means that the right ion must be chosen with a compromise between the right OER-RBE and minimum fragmentation. The field then narrows to ions with $Z \leq 8$, first of all carbon, followed by oxygen and helium currently under study. One can also notice that neutrons are also very efficient in killing cancerous cells. Unfortunately, neutrons have a very poor ballistics and an accurate sighting of a tumor is very difficult to achieve.

1.4 Importance of a well known RBE and nuclear cross section

As already mentioned the survival curve of cells irradiated with γ rays and protons are similar, indicating that, when the effects of the nuclear interactions are not considered, the behavior of high energy protons is like that of γ rays. The proton data are also well fitted by the model on which the production of secondary fragments is being taken into account. This indicates that the low energy recoil particles contribution is significant. Thus in clinical context, due to the high RBE values expected for the secondary particles, the contribution arisen from the nuclear reactions might be especially relevant at the low dose deposited in the entrance region. However, very limited information is available in the literature in terms of biological experiments. This is reflected especially in the large uncertainties that can be found in the literature concerning the definition of an RBE-LET relation for protons. In figure 1.20 a collection of RBE values for 10% survival as extracted from the Particle Irradiation Data Ensemble[20] is shown. Large fluctuations are observed in published data sets for the description of RBE in tumor cells as well as in surrounding healthy tissues. Such fluctuations are in general larger for in vitro compared to in vivo experiments, the former representing the majority of available data. In most of the

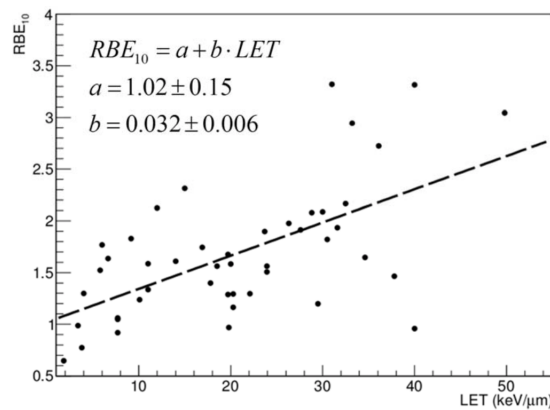


Figure 1.20. RBE values for 10% survival, as extracted from PIDE [20]. The dashed line shows the tendency to an increase in RBE with LET and is the result of a linear fit. All values extracted from the database were pooled together, independent of α/β ratio. This is allowed when looking at RBE for 10% survival.[21]

cases cell killing as measured by means of clonogenic survival assay¹ is the end point studied with in vitro experiments. This information then represents the basis for the evaluation of Tumor Control Probability (TCP) in treatment planning.

Furthermore, the majority of in vitro measurements have been performed with V79 cells, having a low α/β ratio, while in vivo experiments were performed by looking at early-reacting tissues, having in general a high α/β ratio. Thus, since RBE is also dependent on α/β ratio, a direct quantitative comparison of *in vitro vs. in vivo* outcomes might be misleading. At the same time, it is now clear that cell killing alone is a simplistic end point to describe tumor response. This is due to the impact of the tumor microenvironment on the response, communication, and interaction among different cancer cells and among healthy and cancer cells, as well as among targeted and non-targeted cells.

Thus, a fixed RBE equal to 1.1, based in particular on in vivo results, is currently adopted in Proton Therapy in order to describe the increased effectiveness of proton radiation compared to therapeutic photons. This fixed RBE is assigned to protons over the whole range. Indeed, despite the large fluctuations observed, several studies support the idea that $RBE = 1.1$ seems to be a reasonable approximation, and at this time there is no clear and unique clinical evidence against this assumption[21]. In other words, even if this assumption is notoriously wrong, it does not necessarily modify the clinical responses. In addition to the physical uncertainties, biology can contribute with the so-called *biological range extension*. This is a consequence of the parallel increase of LET and decrease of dose taking place at the distal fall-off of the SOBP, resulting in an increase of RBE. This effect can result in a significant biological dose in normal tissues beyond the tumor region, thus introducing additional uncertainty (figure 1.21). According to the fixed RBE of 1.1 adopted in PT, this

¹A *clonogenic assay* is a cell biology technique for studying the effectiveness of specific agents on the survival and proliferation of cells. It is frequently used in cancer research laboratories to determine the effect of drugs or radiation on proliferating tumor cells as well as for titration of Cell-killing Particles (CKPs) in virus stocks.

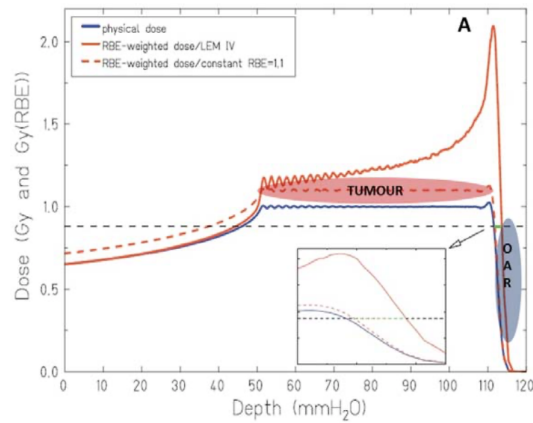


Figure 1.21. Physical and RBE-weighted dose are shown, as obtained with a constant and with a variable RBE. Special emphasis is given to the differences at the distal fall-off, where OAR (*organ at risk*) might be located.[21]

biological range extension due to a gradually increasing RBE is currently not directly considered in treatment planning. The role of a variable RBE in the estimation of the biological range extension has been recently studied using a Monte Carlo- or a LEM-based approach[22][23]. A pronounced dependence on dose and α/β parameters is reported in both studies. Despite some quantitative and qualitative differences attributed to the different biophysical models employed, the largest extensions are obtained for the combination of low doses and low α/β ratios, when a large increase in RBE is expected. The biological extension does not seem to be dependent on target volume, but is rather strongly influenced by the width of the distal penumbra, generally becoming more pronounced at higher energies. To date, there are no

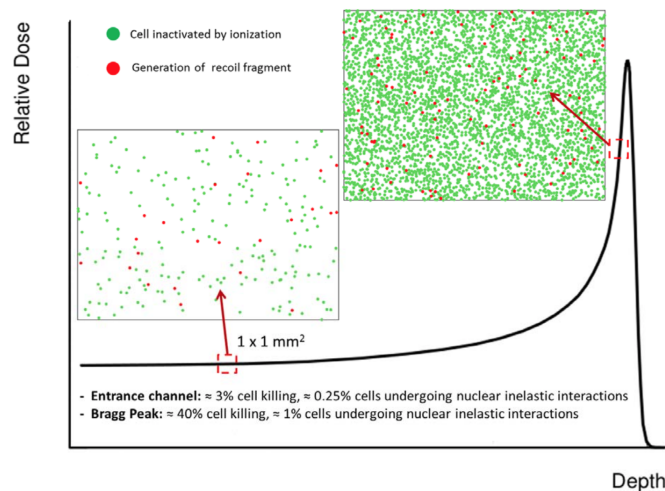


Figure 1.22. Impact of ionization and target fragmentation in tissue sections of $1 \times 1 \text{ mm}^2$ for a proton beam of 250 MeV/u in H_2O . The effect is considered at two different positions along the depth-dose profile.[21]

experimental measures that describe how protons can have a non-constant RBE in the presence of a significant fragmentation of the target. The use of hadron beams in the medical field requires an in-depth study of the process of fragmentation of beams on light targets. The targets, in general, are light elements or materials, such as carbon, water or PMMA (polymethylmethacrylate), in order to simulate human tissues as likely as possible. It is important to acquire knowledge on what types of fragments are produced, in what proportion and with which cross sections and on their kinematic properties, such as kinetic energy and emission angle, through fragmentation measures for different types of projectile-target pairs, at various energies and thicknesses. This knowledge is essential to be able to predict, with some precision, what happens in the patient's body. As can be seen in figure 1.22, the target fragmentation in proton beam is more relevant in the entrance channel region where the impact of nuclear fragmentation as compared to ionization induced cell killing is less (the ratio between the cells damaged by the generated fragments and the ones damaged by the ionization process is $1/8$) than in the peak region (the same ratio is equal to $1/40$).

Is therefore essential to improve the knowledge about the role of nuclear fragmentation in proton therapy and charged particle therapy in general. To preserve the healthy tissues and improve the treatment planning a more complete proton RBE model, which include the fragmentations effects, must be obtained.

The aim of the **FOOT** (FragmentatiOn Of Target) experiment, described in next chapter, is to perform a set of nuclear cross section measurements at PT energies and provide a significant portion of the values currently unavailable in nuclear physics databases.

Chapter 2

FOOT experiment (FragmentatiOn of Target)

As already said in chapter 1 particle therapy uses proton and light-ion beams ($Z \leq 8$) to treat deep-seated solid tumors, exploiting the favorable energy deposition profile and RBE of charged particles. Nuclear interactions with patient tissues can induce fragments production that must be taken into account in treatment planning: in proton treatments target fragmentation produces low-energy, short-range fragments depositing a non-negligible dose in the entry channel, while in heavier-ion beam treatments long-range fragments due to projectile fragmentation release dose in tissues surrounding the tumor. The **FOOT** (FragmentatiOn Of Target) experiment of INFN aims to study these processes to improve the nuclear interactions description in next generation Treatment Planning Systems (TPS) softwares and hence the treatments quality. Target (^{16}O and ^{12}C) fragmentation induced by 150-250 MeV proton beams will be studied via inverse kinematics: ^{16}O and ^{12}C beams (150–250 MeV/u) collide on graphite and hydrocarbon targets to provide nuclear fragmentation cross sections on hydrogen. The projectile fragmentation of these beams will be explored as well. Following these observations, the FOOT experiment will consist of an "upstream region" composed by the pre-target detectors, aim to monitor the impinging beam, and by a region, including the target, for the tracking and the identification of the fragments, that consider two alternative complementary setups: a magnetic spectrometer and an emulsion one. These detector's measurements will be combined to accurately identify fragments charge and mass. The construction of the FOOT detector has started in 2018 and will be completed in 2021.

In this chapter, and in particular in section 2.1, the goals of the experiments and its required performances will be discussed. In in section 2.2 the techniques used are reported and in section 2.3 the detectors in play are described.

2.1 Experiment main goals

Due to kinematic reason, fragments with $Z > 1$ are forward emitted within a cone of 10° semiaperture with respect to the beam axis, whereas light fragments are also scattered at larger angles. Hence, the FOOT apparatus has been designed with two

different setups: an electronic experimental setup, aiming to study heavy fragments, and an emulsion chamber, able to measure light fragments at larger angles. The electronic setup has been optimized to study fragments with $Z > 1$, it aims to provide:

- different fragments production cross sections
- charge Z and mass A fragments identification
- fragment energy spectra

The measurement of the target fragmentation induced by protons is a challenging task due to the low energy and short range (\sim tens of μm) of the produced fragments. For this reason, an inverse kinematic approach will be implemented as explained in section 2.2.1.

To calculate the cross sections and to correctly identify charge and mass of the secondary fragments, the detector will measure their momentum p , kinetic energy E_k , time of flight (TOF) and energy release ΔE . The charge can be in fact identified combining the information from ΔE measurements with TOF, while the mass can be retrieved by p , TOF and E_k through the following three equations:

$$p = mc\beta\gamma \quad (2.1)$$

$$E_k = mc^2(\gamma - 1) \quad (2.2)$$

$$E_k = \sqrt{p^2c^2 + m^2c^4} - mc^2 \quad (2.3)$$

where β and γ are obtained from the TOF. To achieve the requested resolution on cross sections and particle identification, the main measurements performances need to be the following:

- $\sigma(p)/p \sim 5\%$
- $\sigma(E_k)/E_k \sim 2\%$
- $\sigma(\Delta E)/\Delta E \sim 3 - 10\%$
- $\sigma(TOF)/TOF \sim 100ps$

An emulsion spectrometer will provide complementary light fragments ($Z \leq 3$) measurements. It will provide measurements of fragments emitted up to 70° (mainly protons, deuterons, tritons, Helium and Lithium ions).

Along with the study of cross sections relevant in PT, also the fragmentation induced by higher energy beams will be investigated to provide data for space radioprotection.

2.2 Methods and materials

FOOT aims to create a portable system capable of performing measurements on both projectile and target nuclear fragmentation processes. The requirement of a portable setup is fundamental because the needed beams will be available in different facilities, which mainly are

- CNAO (Centro Nazionale di Adroterapia Oncologica) in Pavia (Italy), providing proton and ^{12}C ion beams at CPT energies.
- Heidelberg Ion Therapy (HIT) center in Germany, where ^4He , ^{12}C and ^{16}O beams for CPT are available.
- GSI in Darmstadt (Germany), which can provide ^4He , ^{12}C and ^{16}O and other ion species.

The main objectives are: to provide reliable inelastic cross section data in order to improve the quality of nuclear models currently implemented in the MC simulations inside TPS and to perform measurements regarding the target fragmentation induced by the beam to achieve a well know RBE for protons, fundamental for PT. The difficulty resides in the very low energies (and hence, range) involved in the target fragmentation processes. In FOOT experiment to overcome this obstacle is used an inverse kinematic approach and so a particular target is needed.

2.2.1 Inverse kinematic approach

As already said the measurement of the target fragmentation induced by protons is difficult because of the low energy and short range of the produced fragments (see table 2.1). For this reason, an inverse kinematic approach is used in FOOT (figure 2.1): the fragmentation of tissue-like ion beams (mainly C and O, which are the main constituents of human body) impinging on a Hydrogen enriched target are studied. As a result, secondary fragments will have boosted energy and longer range. By applying the *Lorentz transformation*, it will be possible to switch from the laboratory frame to the "patient frame".

Fragment	E (MeV/u)	<i>LET</i> (keV/ μm)	<i>Range</i> (μm)
^{15}O	1.0	938	2.3
^{15}N	1.0	925	2.5
^{14}N	2.0	1137	3.6
^{13}C	3.0	951	5.4
^{12}C	3.8	912	6.2
^{11}C	4.6	878	7.0
^{10}B	5.4	643	9.9
^8Be	6.4	400	15.7
^6Li	6.8	215	26.7
^4He	6.0	77	48.5
^3He	4.7	89	38.8
^2H	2.5	14	68.9

Table 2.1. Average data for target fragments from a 180 MeV proton beam in water, estimated according to a semi-empirical formula.[24]

Moreover, in order to be able to use the Lorentz transformation, the kinetic energy per nucleon has to remain unchanged; hence, the beam will have the same

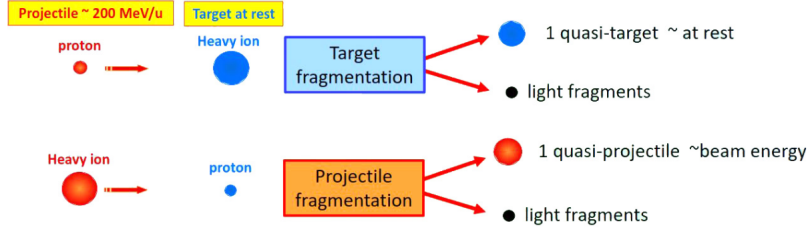


Figure 2.1. Fragments characteristics in direct and inverse kinematics.

kinetic energy of the previous proton beam (the one employed before the application of the inverse kinematics approach (see figure 2.1)), but increased of a factor equal to the projectile mass. This allows also to maintain the same interaction probability that would, otherwise, decrease if the kinetic energy of the new beam had to be the same of the protons one.

Lorentz transformation is a linear transformation that converts the coordinates between two inertial reference frames moving at constant velocity relative to each other. This mathematical tool may also include a rotation of space; in the absence of rotations the transformation is called a *Lorentz boost* (example in figure 2.2). If

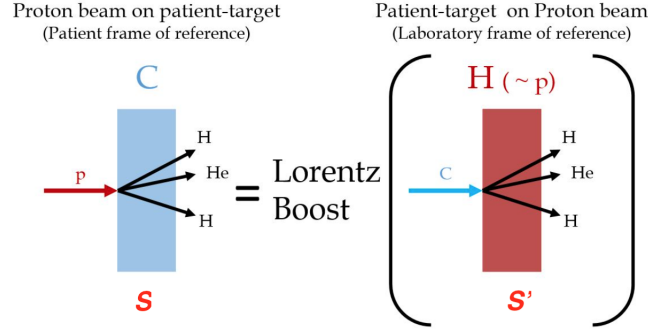


Figure 2.2. Scheme of the Lorentz boost between the two reference frames.

we consider S as the laboratory frame in which the incident beam (composed by heavy charged ions) is moving along z at a constant velocity β and impinges in the stationary hydrogen target and S' the patient frame in which target and projectile material are switched, meaning that the beam is made of protons and the target is tissue-like, the proton 4-momentum components in the S' frame are given by:

$$P' = \Lambda P \quad (2.4)$$

where $P = (E/c, p)$ and $P' = (E'/c, p')$ are the ions 4-momentum in S and S' respectively, while Λ is a 4×4 matrix:

$$\begin{pmatrix} E'/c \\ p'_x \\ p'_y \\ p'_z \end{pmatrix} = \begin{pmatrix} \gamma & 0 & 0 & -\beta\gamma \\ 0 & 1 & 0 & 0 \\ 0 & 0 & 1 & 0 \\ \beta\gamma & 0 & 0 & \gamma \end{pmatrix} \begin{pmatrix} E/c \\ p_x \\ p_y \\ p_z \end{pmatrix} = \begin{pmatrix} \gamma E/c - \beta\gamma p_z \\ p_x \\ p_y \\ -\beta\gamma E/c + p_z \end{pmatrix} \quad (2.5)$$

So the inverse Lorentz transformation is:

$$\begin{pmatrix} E'/c \\ p'_x \\ p'_y \\ p'_z \end{pmatrix} = \begin{pmatrix} \gamma & 0 & 0 & \beta\gamma \\ 0 & 1 & 0 & 0 \\ 0 & 0 & 1 & 0 \\ -\beta\gamma & 0 & 0 & \gamma \end{pmatrix} \begin{pmatrix} E/c \\ p_x \\ p_y \\ p_z \end{pmatrix} \quad (2.6)$$

Such approach requires an emission angle measurements with a resolution of the order of few *mrad* in order to have an error less than 10 – 20% on the final cross section measurement obtained by inverse kinematic, once applied the Lorentz boost. Therefore, both the projectile and fragments directions have to be measured accurately.

2.2.2 FOOT Target

The idea is to send typical PT beams (mainly He, C or O) on different target materials representative of human tissues and to characterize the produced particles, so targets will be mainly composed of H, C and O. The choice of using composite materials was dictated by the large amount of technical difficulties introduced by a pure gaseous target. Hydrogen and oxygen cross section values will be extrapolated indirectly, using the results obtained from two different acquisitions and subtracting the respective data. Hydrogen cross sections will be obtained considering a pure carbon target and a polyethylene (C_2H_4) one and applying the formula

$$\sigma(H) = \frac{1}{4}(\sigma(C_2H_4) - 2\sigma(C)) \quad (2.7)$$

The same procedure is also valid for differential cross section:

$$\frac{d\sigma}{dE_k}(H) = \frac{1}{4}\left(\frac{d\sigma}{dE_k}(C_2H_4) - 2\frac{d\sigma}{dE_k}(C)\right) \quad (2.8)$$

$$\frac{d\sigma}{d\Omega}(H) = \frac{1}{4}\left(\frac{d\sigma}{d\Omega}(C_2H_4) - 2\frac{d\sigma}{d\Omega}(C)\right) \quad (2.9)$$

To check the validity of the target cross sections combination method has been evaluated from the simulated data both the cross section on hydrogen target and the cross section obtained from the difference method. The comparison is reported in figure 2.3, that shows the energy differential cross section of a 200 MeV/u ^{12}C beam on hydrogen target in inverse kinematics obtained with the subtraction method and with the direct one. The results from the two estimations are in good agreements, thus validating the combination method[24]. For Oxygen measurements, an additional PMMA (PolyMethyl MethAcrylate, chemical formula $(C_5O_2H_8)_n$) target will be used. A possible problem with this approach is that the uncertainties on indirect cross sections are calculated as the quadratic sum of single target measurements, meaning that they can become quite large. Furthermore the multiple scattering angle of beam+fragment couple inside the target must be kept below the *mrad* as well. This sets a severe limit on the allowed thickness of the target (of the order of 2 – 4 g/cm^2) and limits accordingly the probability of the fragmentation events to order of 10^{-2} .

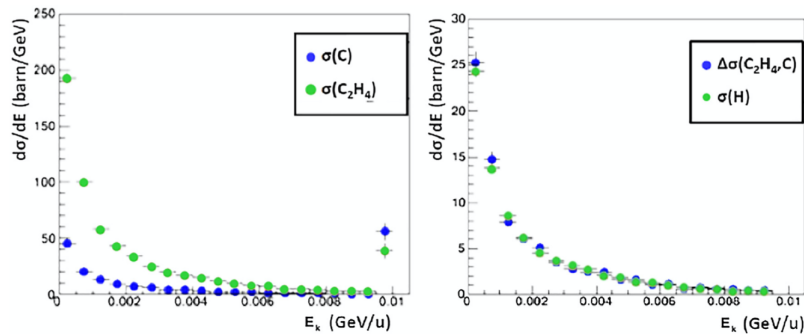


Figure 2.3. Reconstruction of energy differential cross sections of C fragments in inverse kinematics for a ^{12}C beam on C and C_2H_4 target (left panel) and on H obtained either by subtraction or directly on H target (right panel). Data have been obtained from FLUKA simulations.[32]

2.3 Experimental Apparatus

The experience from previous experiments about nuclear fragmentation, together with the study of the relevant physics process by means of Montecarlo simulations, show that it's hard to achieve the desired acceptance for all secondary fragments with an apparatus of limited size. The main reason comes from the fact that lower mass fragments ($Z < 3$) can be emitted within a wider angular aperture with respect to heavier nuclei. Therefore the necessary size, and weight, of a magnetic apparatus would become impracticable in view of a "table-top" setup design. Therefore, the FOOT experiment is composed by two complementary setups:

- a setup based on a *magnetic spectrometer*, aiming to the identification and measurement of fragments heavier than the ^4He , covering an angular acceptance up to 10-20 degrees with respect to the beam axis;
- a setup exploiting the *emulsion chamber* capabilities. As already tested in the FIRST experiment, a specific emulsion chamber will be coupled with the pre-target devices of the FOOT setup to measure the production in target fragmentation of light charged fragments as protons, deuterons, tritons and Helium nuclei. The emulsion spectrometer supplies complementary measurements for fragments emitted at large angle with respect to the electronic detector, extending the angular acceptance up to about 70° .

2.3.1 Magnetic spectrometer

One of the main requirements of the FOOT detector design is a robust charge and isotopic identification of the produced fragments. Therefore the setup measures the following quantities of the fragments produced: momentum, kinetic energy, Time Of Flight (TOF). The fragment dE/dx is measured twice through the energy release (ΔE) in a thin slab of plastic scintillator and thin silicon detector. The required detector performances (see section 2.1) must be achieved on the heavier fragment (C,N,O) that are the most difficult to be correctly identified, and can be released

on the lighter particles produced. The charge can be identified by crossing the ΔE measurements with TOF or kinetic energy, while the mass can be extracted by momentum and kinetic energy.

The fragmentation contribution due to detector material must be kept as low as possible, evaluated using both MC and data itself and finally subtracted. Designing the detector as compact as possible makes it capable of exploiting particle beams at different therapeutic centers so, as a consequence, the overall detector size should lie within the 1.5-2 meters range. The detector geometry is driven by two main factors: the emission angle of the (heavy) fragments and the angular separation between two fragments emitted in the same events. The first item decides the angular acceptance while the second rules the granularity. An example of the prediction from Monte

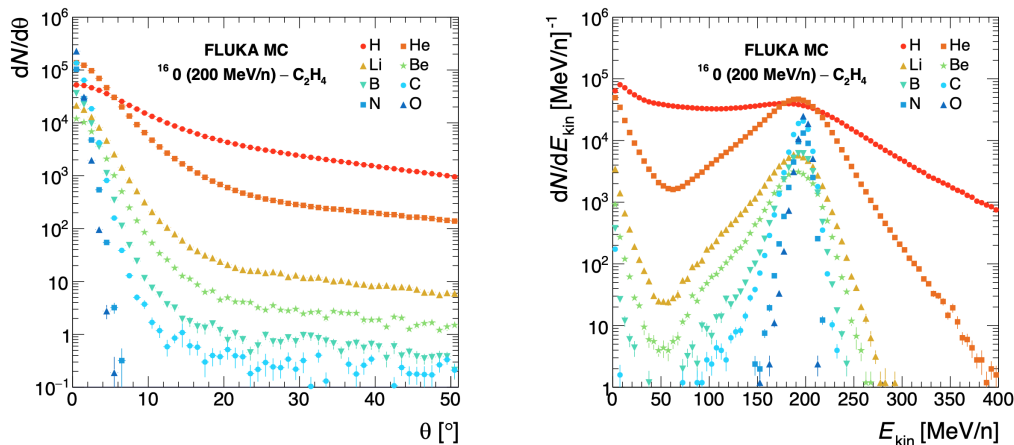


Figure 2.4. MC calculation of the angular (Left) and kinetic energy (Right) distributions of different fragments produced by a 200 MeV/u ^{16}O beam impinging on a C target.[19]

Carlo calculation is given in figure 2.4 where the angular and energy distribution of different fragments produced by a 200 MeV/u ^{16}O beam impinging on a C target are shown as resulting from the FLUKA code[25][26]. The detector can be divided downstream in three different regions: the upstream/target region, the magnetic tracking region and the calorimeter region. A schematic view of the detector is shown in figure 2.5.

Start Counter

The Start Counter (SC) is made of a thin squared foil of EJ-228 plastic scintillator, 250 μm thick and 5 cm transverse size, sufficient to cover the typical beam transverse size. The scintillator foil is held by means of an aluminum frame enclosed in a black 3D printed box to provide the light tightness needed for the detector operation. In the black box, two squared windows are placed in correspondence of the scintillator field of view and closed with thin (4 μm) aluminized mylar. A scheme is shown in figure 2.6. The light produced in the scintillator is collected laterally by 48 (AdvanSiD ASD-NUV3S 1) $3 \times 3\text{mm}^2$ SiPMs, 12 per side, bundled in 8 channels, each reading the series of 6 SiPMs. The readout and powering of the SiPMs is handled by the WaveDAQ system[29], capable of sampling signals at rates up to 5 Gsamples/s in a

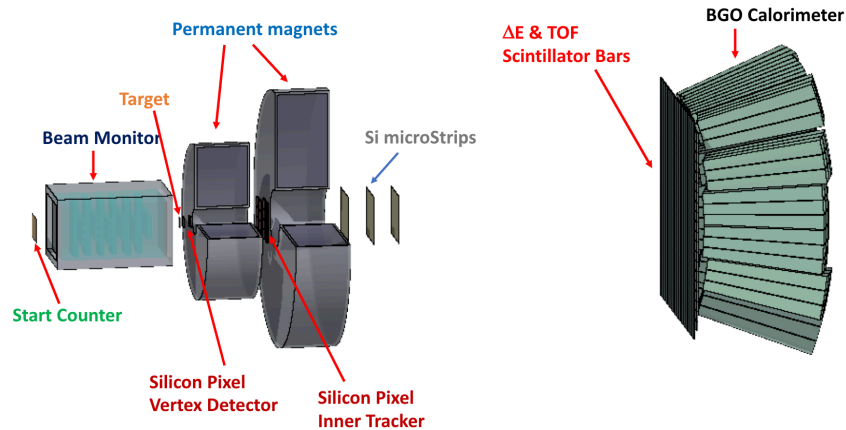


Figure 2.5. FOOT electronic setup for the measurements of heavy ion fragments ($Z > 1$). [19]

dynamic range of 1 V. A gain between 0.5 and 100 can be applied to the incoming signal before digitization. This is a fundamental parameter for SC due to the low light signal released because of its thinness. In this way, the SC gain can be tuned according to the beam type and its energy. The acquired waveforms are analyzed offline with a constant fraction discriminator technique to extract the event time t_0 . The thickness of the scintillator was minimized to reduce the pre-target particle interaction probability, less than 5% with respect to the on-target one, assuming a 2mm thick graphite target. The SC, placed 44 cm upstream of the target, provides the trigger signal to the whole experiment and the measurement of incoming ion flux to be used for the cross section measurement. It provides the reference time for all the other detectors and allows the TOF measurement in combination with the TW scintillator detector. The SC performances show an excellent efficiency very close to unity. A time resolution of the order of $\sigma_t \sim 60$ ps has been measured using only one of the four channels of the device. Such a results indicate that the SC can fulfill the FOOT detector requirements.

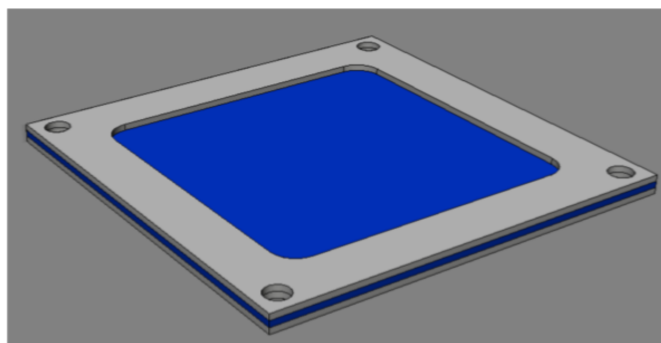


Figure 2.6. Drawing scheme of the start counter.

Beam Monitor

The Beam Monitor (BM), already used in the FIRST experiment[28], is a drift chamber consisting of twelve layers of wires, with three drift cells per layer. Planes with wires oriented along the x and y axes are alternated in such a way to reconstruct the beam profile. The cell shape is rectangular ($16\text{mm} \times 10\text{mm}$) with the long side orthogonal to the beam. In each view two consecutive layers are staggered by half a cell to solve left-right ambiguities in track reconstruction. The BM was operated

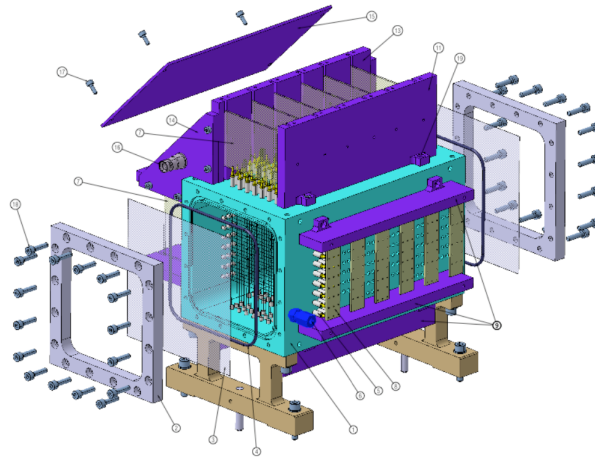


Figure 2.7. Technical drawing of the BM drift chamber.

at atmospheric pressure, at the working voltage of 1.8 kV in Ar/CO_2 , 80/20% gas mixture. The BM efficiency was measured to be close to unity ($\sim 90\%$) for carbon ion beam and the mean track spatial resolution was measured to be of the order of $\sim 100\mu\text{m}$. A technical drawing of the chamber is shown in figure 2.7. The BM detector is placed between the SC and the target and is used to measure the direction and impinging point of the ion beam on the target, a crucial information needed to address the pile-up ambiguity in the slow VTX detector (readout time = $187\mu\text{s}$). In fact the BM read-out time, of the order of $1\mu\text{s}$ or less, is fast enough to ensure that tracks belonging to different events cannot be mixed.

Target & Vertex

The Vertex detector implementation profits of the experience of the FIRST experiment and uses the same mechanical structure. It holds up to five different targets in a sliding tray that can eventually be moved also automatically by a remote controlled actuator. The stack of sensors is placed as shown schematically in the right side of figure 2.8: this arrangement guarantees an acceptance at the level of about ± 40 degrees for the fragments produced in the target. The four tracking layers of the vertex tracker uses as sensing element the M28 chip implemented by the Strasbourg CNRS PICSEL group. The M28 chip is from the family of the CMOS Monolithic Active Pixel Sensors (MAPS) that are widely used in optical imaging, X-ray imaging and charged particle detection for experiments in particle and heavy-ion physics.

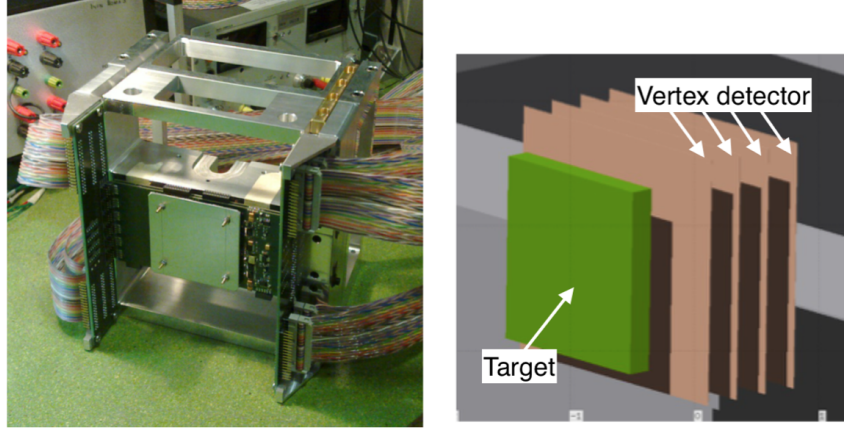


Figure 2.8. FOOT Vertex detector picture complete with its readout system (left). Target and vertex tracker geometrical scheme (right).

The architecture of the MIMOSA28 integrates a fast binary readout and a zero suppression logic to reduce the amount of data produced. The sensor consists of a matrix composed by 928 (rows) x 960 (columns) pixels of $20.7 \mu\text{m}$ pitch for a size of the chip of $20.22 \text{ mm} \times 22.71 \text{ mm}$. The thickness of the epitaxial layer is $15 \mu\text{m}$ on a high resistivity substrate of the order of $400 \Omega\text{cm}$. The high hit rate of the STAR vertex detector of $2.4 \times 10^5 \text{ hits/s/cm}^2$ has driven the design of the sensor for a fast readout frequency in order to keep the track multiplicity per frame at a manageable level for the zero suppression logic implemented in the chip. All four M28 sensors are thinned to $50 \mu\text{m}$, then the overall material budget for the entire Vertex tracker is $200 \mu\text{m}$. In the left picture of figure 2.8 we see the system used for the FIRST experiment equipped with two M26 MIMOSA, in FOOT replaced with M28 MIMOSA, sensor planes (the two printed circuit boards behind the squared aluminum cover).

Magnets

A key element for the FOOT spectrometer is the magnetic system used to bend the fragments produced in the target. The main constraints are the momentum resolution at the level of few percent and the portability of the system. The portability forces choice of permanent magnets producing the needed $B \times L$ in a limited sizes and weight. The accuracy of p measurements increases as transverse momentum variations Δp_T become larger. For a particle of charge q moving in a magnetic field B of length L , Δp_T is given by[30]:

$$\Delta p_T = \int_0^L B dl \quad (2.10)$$

This means that p resolution depends mainly on B and L . A Halbach (showed in figure 2.9) and Halbach-like configuration are adopted: the dipolar magnetic field is obtained with a cylindrical geometry with the internal cylindrical hole being the region where the magnetic field is rather uniform. The magnetic structure is made of twelve single pieces made of $\text{Sm}_2\text{Co}_{17}$ (Samarium-Cobalt).

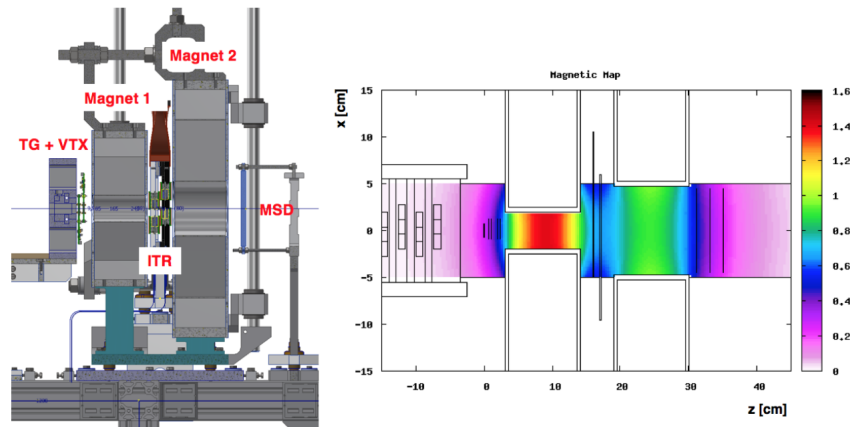


Figure 2.9. (Left) Technical design of the interaction and tracking region. (Right) Computed magnetic field map produced by the FOOT magnets in Halbach configuration.[19]

The magnetic field increases with the external cylinder radius while decreases with the gap radius. So in order to match the final momentum resolution producing the needed $(B \times L)$ and at the same time have an angular acceptance of 10° for the emitted fragments, two different magnet dimensions have been chosen. The first magnet with gap diameter of 5 cm while the second of 10.6 cm can provide respectively a maximum intensity of 1.4 T and 0.9 T in the internal cylindrical hole, with a gaussian shape magnetic field along the cylinder axis, according to the computed magnetic map shown in figure 2.9 (Right), while the inner tracker, sitting in-between the two magnets, will experience a field at the level of 0.6 T. The final magnets weigh 200-300 kg, which means that a robust mechanical frame is mandatory to exploit the best possible resolution ($\sim 10\mu m$) achievable by the tracking system. The further capability of the solid structure (figure 2.9 (Left)) to vertically offset the assembly of about 40 cm gives the opportunity to align the tracking stations in specific runs without the magnets, to adapt the setup to different experimental rooms and it is compatible with the tracking detectors accessibility.

Inner Tracker

The FOOT Inner Tracking station foresees two planes of pixel sensors to measure both the position of the track in the plane orthogonal to the beam axis and the direction of the track itself. While the transverse displacements of the two sensing planes can be reconstructed from the data, their longitudinal distance requires a precise mechanics with a spacer, as it will be described in the following. The ITR covers an area of about $8\text{ cm} \times 8\text{ cm}$, according to the emission angle distribution that is broader here than in the VTX, in between the two permanent magnets at a distance of $\sim 20\text{ cm}$ from the target.

The detector is composed by two planes of 16 M28 sensors. Figure 2.10 shows a schematic view of four of these ladders. The ITR ladder is a double-sided layout, which consist of two modules of M28-sensor layers glued on the opposite sides of a

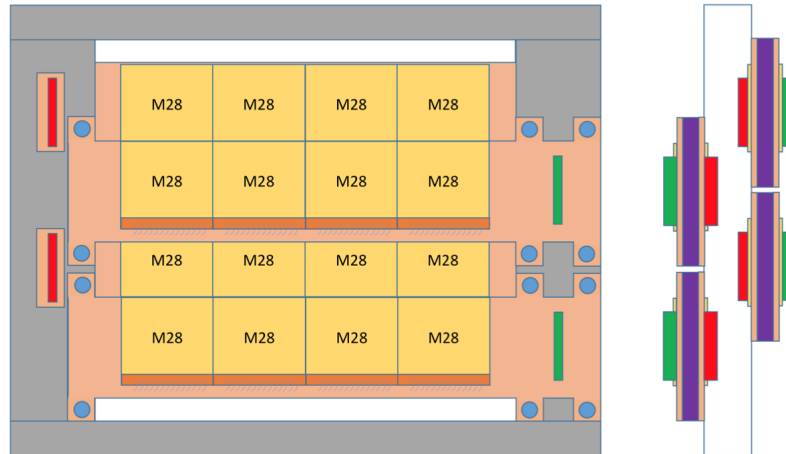


Figure 2.10. Inner tracker scheme.

support structure, made of low density silicon carbide (SiC) foam, 2 mm thick. In each module the four sensors bonded on a Flexible Printed Cable (FPC) made of Kapton having two or three conductive planes and an overall thickness $\sim 100\mu\text{m}$. The flex cables provide all communications and services of the sensors from and to the outside world. The overall material budget of an ITR ladder is $x/X_0 \simeq 0.3\%$. The ITR will be composed of four ladders, two for each plane, supported by a metallic frame to hold the entire tracker.

Microstrip Silicon Detector

Tracking of fragments downstream the magnetic volumes is essential for the measurement of momentum and is also fundamental to match the reconstructed tracks with the hits in the TOF scintillator and the calorimeter. Also the redundant measurement of dE/dx would be mandatory to improve the reliability of the experiment. The choice of a microstrip silicon detector has been dictated by the need to:

- work as close as possible to the last magnet;
- provide a sufficient spatial resolution ($\simeq 40\mu\text{m}$) for at least 3 x-y points;
- minimize the amount of material to reduce the impact of multiple scattering and also to reduce secondary fragmentation effects;
- provide a precise dE/dx measurement for heavy ions up to the 200-700 MeV/u kinetic energy range;
- provide the capability for dE/dx measurements up to 1 GeV/u in order to extend the physics potential of the FOOT experiment in the astrophysical domain.

According to the 10° opening angle needed to cover ions with $Z>2$, the surface that has to be covered right after the second magnet is $9.3 \times 9.3 \text{ cm}^2$. Three x-y planes are

be separated one to each other by a 2 cm gap along the beam direction, ensuring a compact measurement system. In order to reduce the amount of material needed for each measurement plane to $\sim 150\mu\text{m}$, and to ensure the x-y coordinate readout, a solution exploiting two silicon planes thinned down to $70\mu\text{m}$ each one and glued together (see figure 2.11). The two independent layers solution with respect to the one with a single thick plane will ensure two independent dE/dx measurements and more rigid mechanical behavior. To compensate for the smaller signal produced in the silicon, the on strip amplification mechanism (working with gain ~ 10) has been implemented.

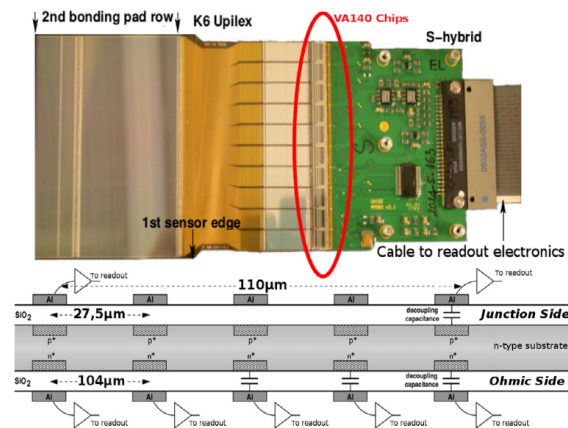


Figure 2.11. The sensor used (top) and its readout scheme (bottom).[31]

Plastic scintillator wall (TW detector)

The TW detector contributes to the particle identification by providing the velocity β of the crossing fragments, which can be obtained by the TOF, and the atomic number Z , since the deposited energy ΔE is proportional to Z (eq. 1.1). The detector is based on plastic scintillators read by silicon photomultipliers (SiPM) [33]. Plastic scintillators are particularly advantageous because they are fast, can be easily shaped based on custom requirements and have long attenuation length. They are appropriate for charged particle detectors because they are capable to reveal minimum-ionizing-like particles with a few mm thick detectors. FOOT TW detector is composed of two layers of plastic scintillator bars (figure 2.12), arranged orthogonally and read by silicon photomultipliers controlled with dedicated electronics. The two layers of orthogonal bars in the TW detector will measure the coordinates in the transverse plane of the interaction position of each fragment in the scintillator[34].

Each bar is 3 mm thick, 2 cm wide and 44 cm long, and each layer is composed of 20 bars. The dimensions of the bars and of the detector are determined by various constraints. Since the TW detector is placed at approximately 1 m from the vertex of production of the fragments, an area of $40\text{ cm} \times 40\text{ cm}$ is required to match the angular aperture of the heavier fragments at this distance. A bar width of 2 cm limits the occurrence of double fragments in the same bar below a few percent level

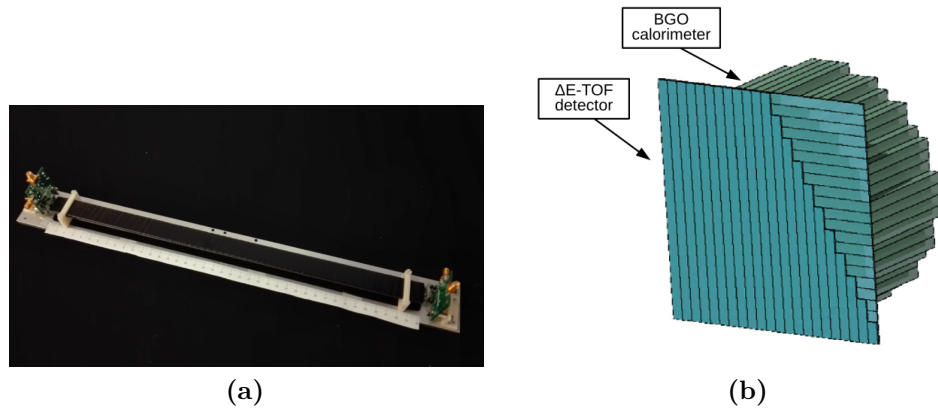


Figure 2.12. In panel (a) a picture of one of the bars in the TOF-Wall detector. Note the darkening tape around the bar used to shield the scintillator material from background light sources.[24] In panel (b) a scheme of the calorimeter region, obtained with FLAIR, the FLUKA graphical interface.

and matches the transversal dimension of the cells of the calorimeter, which the TW detector will be mechanically coupled to.

Each of the two edges of the TW bars is coupled to 4 SiPM (MPPC S13360-3025PE 2) with $3 \times 3 \text{ mm}^2$ active area and $25 \mu\text{m}$ microcell pitch. The signals of each channel (two channels per bar) are digitized at rates of 3-4 Gsamples/s, depending on the trigger scheme adopted, by the WaveDAQ system, the same readout shared also with the SC detector. A total of 1024 samples are collected for each signal allowing to record the whole waveform, and to extract offline the time and the charge information.

Calorimeter

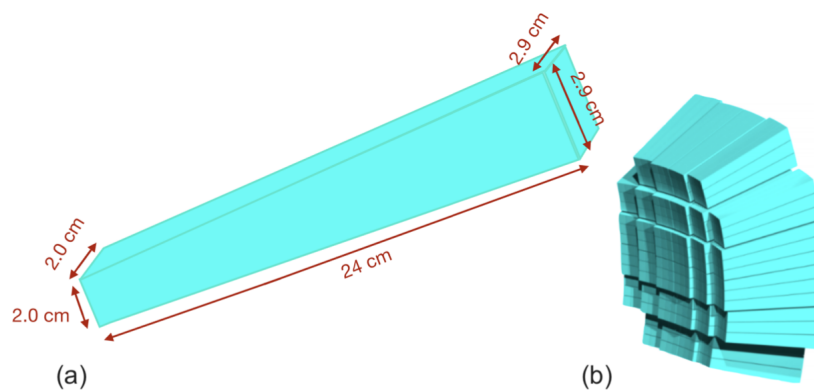


Figure 2.13. Schematic view of the BGO crystal (a) and of the fully assembled calorimeter detector (b).

The FOOT calorimeter is the most downstream detector. It is designed to

measure the energy of projectile fragments produced in the target. The upper bound of the fragments energy range is defined by the beam energy, while the lower bound is set by the intensity of the magnetic field. FOOT operates in a range in which fragments are below the energy threshold that triggers a shower in a calorimeter. Therefore, the mechanisms for energy loss will be driven by the electro-magnetic interaction and nuclear interactions: the production of neutrons escaping the calorimeter undetected produces a systematic underestimation of the initial energy. It includes 32 modules of BGO (it has a high neutron capture cross section ~ 1.47 barn) crystals arranged in a pointing geometry, as shown in Figure 2.13. Each module is made of 9 crystals encased in a 3D-printed plastic support, which was designed to hold the crystals from the back and leave only air and BGO in the first 12 cm of the detector. This is made possible by the shape of the crystals, i.e. a truncated pyramid with $2 \times 2 \text{ cm}^2$ and $2.9 \times 2.9 \text{ cm}^2$ surfaces and a length of 24 cm. The choice of BGO was dictated by its high density and light yield. The crystals are then read-out by $8 \text{ mm} \times 8 \text{ mm}$ Silicon PhotoMultipliers (SiPMs). Some tests have shown that the crystals can reach an energy resolution ranging between 1 – 3%.

2.3.2 Emulsion Chamber

To characterize the production of low Z fragments (i.e. $Z \leq 3$, mainly protons, deuterons, tritons, Helium and Lithium ions), an emulsion spectrometer has been included in the FOOT setup. In figure 2.14 the arrangement of the emulsion spectrometer (ES) inside the FOOT detector is shown: the ES is placed behind the Start Counter and the Beam Monitor. Among all tracking devices used in

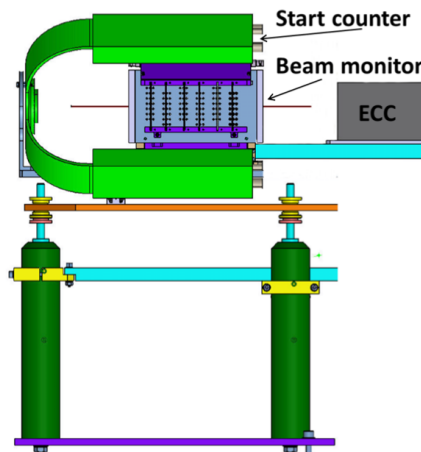


Figure 2.14. Emulsion spectrometer setup inside the FOOT detector.

particle physics, nuclear emulsion detectors achieve the highest spatial resolution (sub-micrometric) for tracking ionizing particles. Emulsions have a long history and contributed to outstanding achievements and discoveries in particle physics. After a natural decline with the advent of fast electronic detectors in the sixties, this technique has experienced a vigorous rebirth in the last twenty years thanks to the advances in high-speed automated scanning and the industrial production

and handling of emulsions. Nowadays, they are still unsurpassed for the detection of short-lived particles and for specific applications in neutrino physics and other emerging fields[35].

Thanks to the huge progresses in the automated scanning system (large angle particles are detected above 70° with respect to the incident angle), emulsion detectors were adopted also in the framework of the FIRST (Fragmentation of Ions Relevant for Space and Therapy) experiment to study fragments produced at large angles by 400 MeV/u ^{12}C ions impinging on a composite target[28].

Based on the Emulsion Cloud Chamber (ECC) concept, the ES for the FOOT experiment is designed with passive materials (as Carbon) alternated to nuclear emulsions films acting as both high-resolution tracking devices and ionization detectors. It is composed of three sections (figure 2.15): vertex and tracking detector, ionization detector for charge identification and tracking detector for momentum measurements. The nuclear emulsion films consist of two $70\ \mu\text{m}$ thick sensitive layers deposited

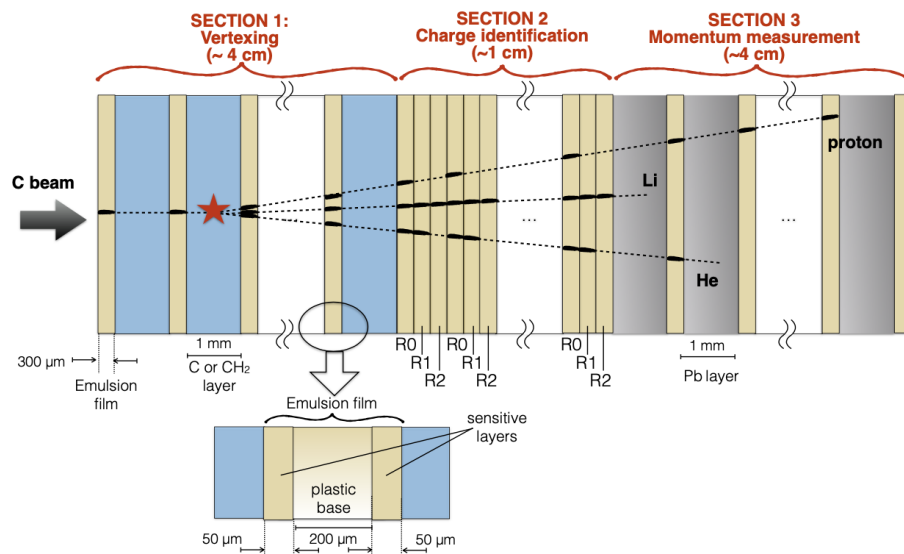


Figure 2.15. Scheme of the emulsion spectrometer (ES) composition for the FOOT experiment.

on both sides of a $210\ \mu\text{m}$ plastic base, resulting in a total thickness of $350\ \mu\text{m}$. The sensitive regions are made of AgBr crystals of $0.2\ \mu\text{m}$ diameter scattered in a gelatine binder, able to detect Minimum Ionizing Particles (MIPs). The trajectory of a MIP is recorded by all AgBr crystals along its path, which act as latent image centers. A chemical process, known as *development*, enhances the latent images inducing the growth of silver clusters (grains) with a diameter of $0.6\ \mu\text{m}$, which can be seen with an optical microscope. The grains density is proportional to the ionizations caused by the passage of the charge particle within the dynamical range. When the ES setup is in operation the pre-target region of the electronic one monitors the incoming primary beam, while the emulsion chamber acts as both target and fragments detector: the first section, where the target layers (C or C_2H_4) are alternated with emulsion films reconstructs the interaction vertex; the second one, composed of emulsion films reconstructs the charge; the last one, in which the

emulsion films are interleaved with Lead layers, measures fragments energy and momentum through the Multiple Coulomb Scattering (MCS) process:

$$p[MeV/c] = \frac{13.6}{\beta\partial\theta[mrad]} Z \sqrt{\frac{x}{X_0}} \quad (2.11)$$

where p is the fragment momentum, β its velocity, Z its charge, x the traversed distance $\partial\theta$ is the deviation of the track slope along its path and X_0 the radiation length characteristic of the material.

The imprinting process due to the passage of a particle in the emulsion film and the following development process make the emulsion spectrometer a one-shot detector: for each data taking with a fixed combination of ion beam, energy and target, a different emulsion spectrometer has to be assembled, exposed and lately scanned and analyzed.

Chapter 3

Monte Carlo Simulation and measurements

The software developed for the FOOT experiment called SHOE (Software for Hadron-therapy Optimization Experiment), is organized as a toolkit. The simulation is carried out by a Monte Carlo code FLUKA[25][26]. The latter is used to generate accurate models of hadronic interactions with graphite and polyethylene targets according to the approach described in the section 2.2.2, in the energy range typical of charged particle therapy.

The simulation of events proceeds according to four phases:

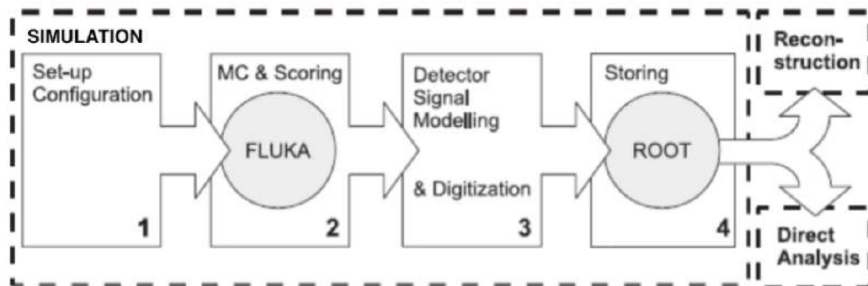


Figure 3.1. Data simulation process.

1. A detailed description of the experimental setup, the geometry of the detector and the materials, to correctly evaluate the interaction in all active detectors and the production of secondary fragments outside the target;
2. Software generates the particles and their transport, allowing to obtain the physical quantities of the traces (for example, primary and secondary particles propagated through the experimental volume) and hits (for example, deposition of the particle energy in the detector elements);
3. Modeling the responses of the detectors, the information that comes from the first simulation phase is processed and the interaction of the particles with the apparatus becomes available;

4. Information produced, relating to the simulated tracks, hits and digitized signals, passes to a subsequent analysis phase.

The simulation process is illustrated in figure 3.1. To facilitate geometry modeling and data processing, a C++ interface is used. The simulation of the detector response is stored in ROOT files[36], with which the analysis and study of the quantities in question are carried out.

An high degree of detail is fundamental to evaluate with high accuracy the acceptances, the efficiencies and resolutions for the cross-section measurement.

This chapter briefly describes the operating principle of the Monte Carlo Fluka simulation and the experimental measurement methods for identifying the fragments.

3.1 Fluka

Fluka is a general purpose tool developed from the collaboration of INFN and CERN for calculations of particle transport and interactions with matter, covering an extended range of applications spanning from proton and electron accelerator shielding to target design, calorimetry, activation, dosimetry, detector design, Accelerator Driven Systems, cosmic rays, neutrino physics, radiotherapy etc[25][26][27]. The highest priority in the design and development of Fluka has always been the implementation and improvement of sound and modern physical models. Fluka can simulate with high accuracy the interaction and propagation in matter of about 60 different particles, including photons and electrons from 100 eV–1 keV to thousands of TeV, neutrinos, muons of any energy, hadrons of energies up to 20 TeV and all the corresponding antiparticles, neutrons down to thermal energies and heavy ions. The program can also transport polarised photons (e.g., synchrotron radiation) and optical photons. Time evolution and tracking of emitted radiation from unstable residual nuclei can be performed on line.[25] Figure 3.2 shows the geometry of the experimental setup described in chapter 2, implemented in FLUKA.

The validity of the physical models used by FLUKA was compared to a variety of experimental data over a wide range of energies. In the field of particle therapy, the *hadron-nucleus* and *nucleus-nucleus* interaction models are fundamental to obtain an accurate calculation of the dose released in the body of the treated patient.

Hadron-nucleus model

The hadron-nucleus inelastic collisions in FLUKA are described, in terms of resonance and decay production, up to a few tens of GeV and, in terms of the Dual Parton Model (DPM) coupled to a hadronization scheme, up to tens of TeV.

This process could be described in three steps: Glauber-Gribov[38] cascade (for energies $>5\text{GeV}$) or Generalized Intra-Nuclear cascade (for energies $<5\text{GeV}$) which corresponds to the *abrasion* or entrance channel phase process (see 1.2), pre-equilibrium emission in which the nucleus reaches a balance through a chain of nucleon-nucleon collisions and at the end an evaporation, fission, fragmentation or γ de-excitation phase as long as the energy is insufficient for any other process.

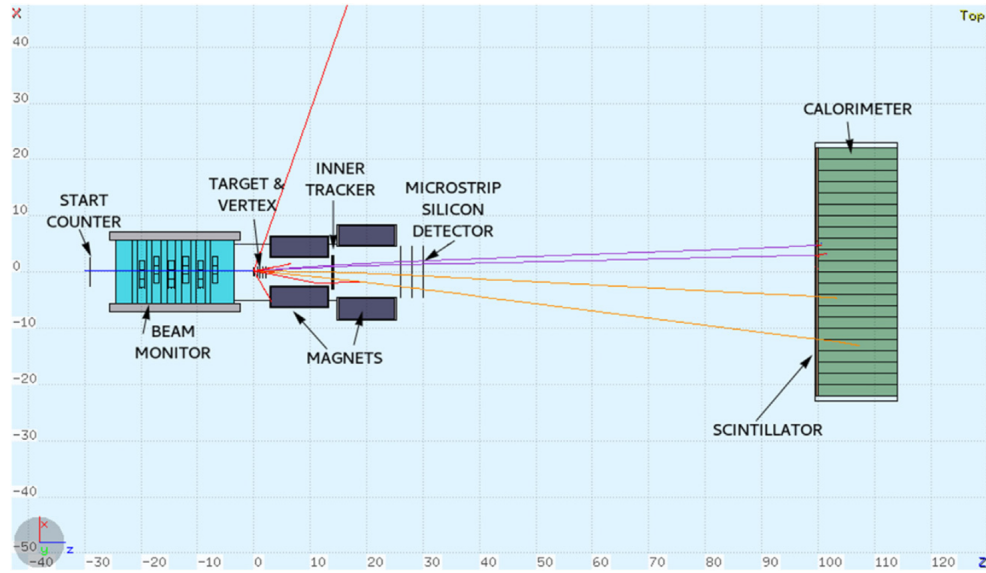


Figure 3.2. 2D view of the FOOT complete experimental setup produced with Flair, the Fluka geoviewer.[32]

Nucleus-nucleus model

The probability that a projectile nucleus collides with a target nucleus, within a certain distance x traveled in the material, depends on the total reaction cross sections σ_R , i.e. the probability that inelastic collisions occur:

$$\sigma_R = \sigma_{inel}(E) \quad (3.1)$$

FLUKA uses the σ_R value in addition to the particle decay time for the determination

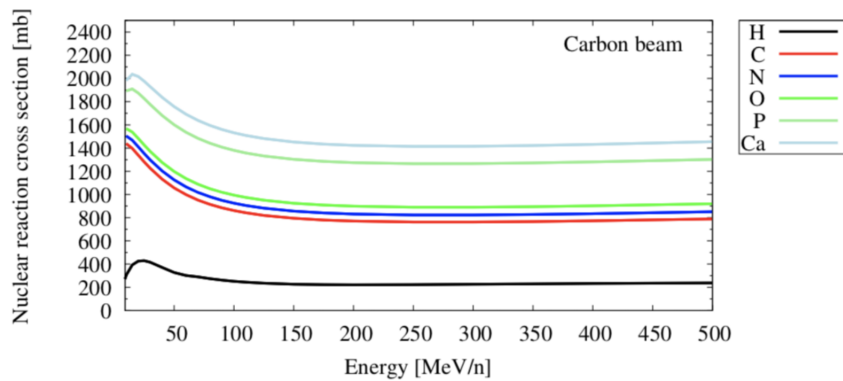


Figure 3.3. Reaction cross section of carbon ions at therapeutic energies as predicted by FLUKA for the most frequent elements present in the human body[28].

of the mean free path of a transported particle: the next collision point is chosen using the reaction cross section calculation. For energy below 5GeV, FLUKA uses a parametrization of σ_R based on the Tripathi semi-empirical model[37] while for higher energies the Glauber model[38] predictions is used.

Figure 3.3 shows the predicted nuclear reaction cross section of carbon ions for the most frequent elements present in the human body as a function of the energy. There is a strong dependence on energy at energies lower than 50 MeV/u while at higher energies a constant behavior is observed

3.2 Isotopic identification of fragments

In order to carry out the measurements of the cross sections of fragmentation it is necessary to identify the fragments and measure their direction of emission, the pulse module and the energy. The experimental apparatus, located after the target, was designed to measure these quantities.

A nuclear fragment is uniquely identified when its charge and mass number are correctly measured. The charge Z of the fragment is measured, through the ΔE and TOF measurements of the TW detector. The charge measurement coupled to the measurement of the *rigidity* (p/Z) of the fragments, through their tracking and bending in the magnetic field, provides the momentum p . As discussed in chapter 2 by using the measurement of p , TOF and E_k and inverting the set of equations 2.1,2.2,2.3, it is possible to have three different measurement of the fragment mass:

- m is related to its momentum and velocity measured by the magnetic spectrometer plus the TW detector according to eq. 2.1 and then the mass number is:

$$A = \frac{m}{u} = \frac{p}{u\gamma\beta c} \quad (3.2)$$

- given the particle kinetic energy measured by the calorimeter in eq. 2.2 the mass number is:

$$A = \frac{m}{u} = \frac{E_k}{u(\gamma - 1)c^2} \quad (3.3)$$

- using instead eq. 2.3 that exploits the momentum measurements from the magnetic spectrometer and the E_k measurements from calorimeter:

$$A = \frac{m}{u} = \frac{p^2 c^2 - E_k^2}{2E_k^2 c^2} \quad (3.4)$$

where u is the atomic mass unit equal to $931.494 \text{ MeV}/c^2$ and the Lorentz factor β is calculated as:

$$\beta = \frac{L}{\text{ToF} \cdot c} \quad (3.5)$$

with L as the total distance traveled by the particle from the production point to the entrance face of the $\Delta E - \text{TOF}$ detector. The uncertainty on the mass measurement depends strongly, in all three cases, on the resolution of the kinetic energy, the momentum and β , and therefore on the TOF measurements accuracy. To understand which detectors mostly affect the precision on the mass determination, a systematic study varying the resolution on the TOF, p and E_k has been performed. The fragments mass resolution of carbon isotopes evaluated by changing one of the three parameters (TOF, p , E_k) in the range of interest and by keeping constant the other two is shown in figure 3.4. A major influence of the TOF value on the fragments

mass identification is evident (figure 3.4C). The obtained measured performances in terms of resolution of the detectors of the FOOT apparatus leads to a mass resolution of $\simeq 3\%$ for ^{12}C .

In order to get the best mass estimation, taking advantage of the mass measurement

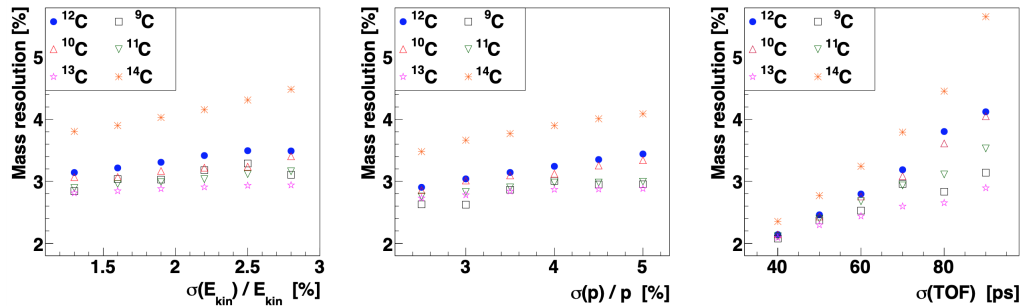


Figure 3.4. Mass resolution of the identified isotopes of carbon ions (^9C , ^{10}C , ^{11}C , ^{12}C , ^{13}C , ^{14}C) as a function of: A) kinetic energy resolution ($\sigma(E_k)/(E_k)$) with carbon ions TOF fixed at 70 ps and momentum resolution at 3.7%; B) momentum resolution ($\sigma(p)/(p)$) with carbon ions TOF fixed at 70 ps and kinetic energy resolution at 1.5%; C) carbon ions TOF with kinetic energy resolution fixed at 1.5% and momentum resolution at 3.7%. [19]

redundancy, a standard χ^2 minimization approach (see figure 3.5) or an Augmented Lagrangian Method (ALM) [42] approach can be pursued, performing a fit to the mass values. The two fit procedures lead to compatible results, centering the mass of the selected fragments always around the expected values. The final mass resolution ranges between 3% for ^{12}C to 6% for protons. Additionally, the χ^2 of the selected fit procedure can be used to select and exclude the events with a worse mass determination, improving further the reached mass resolution. These results, together with the ones on Z determination, assure a complete isotopic identification of the selected fragments. However, the TOF, p and E_{kin} evaluation affects the resolutions achieved on the mass number estimation, as output of the above mentioned fit procedure.

3.2.1 Beam Energy and fragments energy loss measurement

Three of the FOOT electronic setup detectors are involved in energy measurement. Two of them, microstrip silicon detector (MSD) and scintillator wall (TW), have the task of measuring the energy released by the fragments. So the released energy is:

$$\Delta E = \Delta E_{MSD} + \Delta E_{TW} \quad (3.6)$$

For what concerns beam kinetic energy measurement the leading actor between the FOOT detectors is the calorimeter. The aimed resolution goal is of the order of 2-3% for a particle kinetic energy equal to 200 MeV/u, it has to be achieved considering all the terms of equation 3.7 added in quadrature: *stochastic, noise, constant*.

$$\frac{\sigma(E_k)}{E_k} = \frac{a}{\sqrt{E_k}} \oplus \frac{b}{E_k} \oplus c \quad (3.7)$$

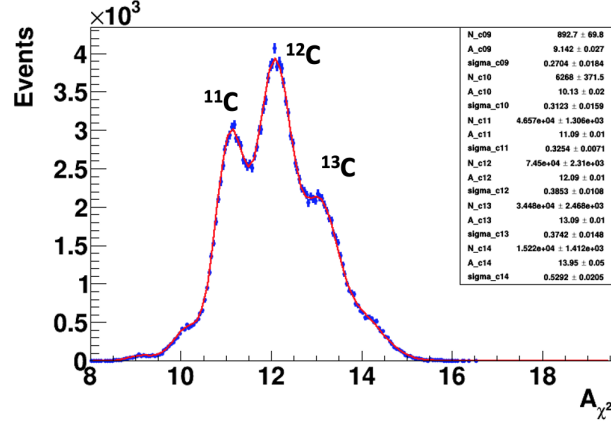


Figure 3.5. An example of mass number determination obtained with the χ^2 fit for the carbon fragments for the case of $\sigma(TOF) \simeq 70$ ps, $\sigma(p)/p \simeq 3.7\%$ and $\sigma(E_{kin})/E_{kin} \simeq 1.5\%$. The ^{11}C , ^{12}C and ^{13}C isotopes are clearly visible.[19]

3.2.2 Time Of Flight measurement

The fragments time of flight measurement is performed by subtracting the start time t_{sc} measured by the SC, to the stop time t_{tw} measured by the TW detector (see figure 3.6). Therefore the TOF is evaluated as follows:

$$TOF = t_{tw} - t_{sc} \quad (3.8)$$

The resolution on the time of flight measurement is computed as:

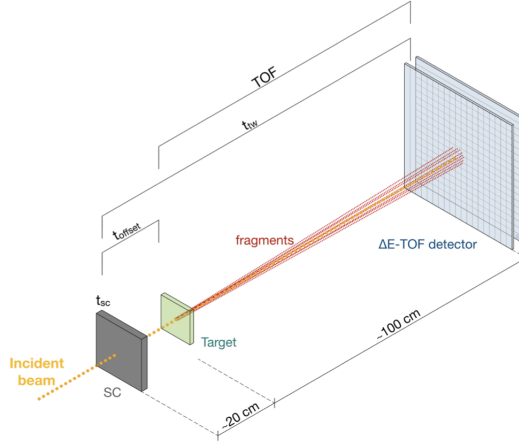


Figure 3.6. Schematic view of the fragments TOF measurement. Detectors not included in this measurement are not represented.

$$\sigma(TOF) = \sqrt{(\sigma(t_{tw}))^2 + (\sigma(t_{sc}))^2} \quad (3.9)$$

In order to match the requirements on the cross section measurements and isotope identification, the TOF measurement needs to be performed with an overall resolution

of ~ 100 ps. The SC detector hence was made to achieve a ~ 70 ps resolution on the incoming ions (at all the different energies). The TW, in a similar way, was projected to measure the fragments crossing time with resolution ~ 30 -40 ps for all the different fragments at different energies (more details in section 4.1.1). All this considering the material and the electronics used by the FOOT experiment, after the first tests, better levels of resolution were reached: ~ 55 ps for the SC and ~ 35 ps for TW.

3.2.3 Momentum measurement

The fragments momentum is derived from the particle deflection inside the magnetic field, if electronic experimental setup is considered, or from the multiple Coulomb scattering if ECC is active (see chapter 2).

The trajectory of a particle with momentum p (in GeV/c) and a charge Ze inside a constant magnetic field \vec{B} is a helix, with radius of curvature r and pitch angle ζ [4]. The radius of curvature and the momentum component perpendicular to \vec{B} are related by:

$$p \cos(\zeta) = 0.3ZeBr \quad (3.10)$$

where B is in Tesla and r in meters. In the case of FOOT experiment the radius of

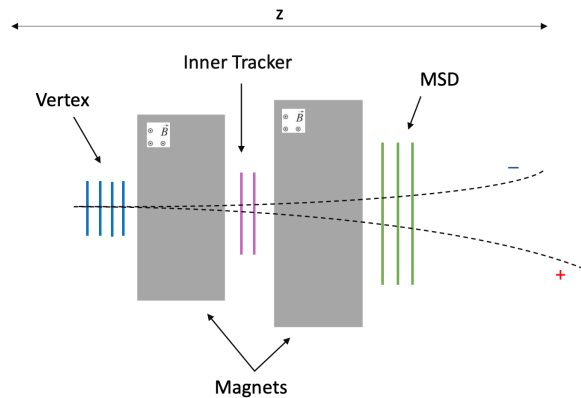


Figure 3.7. Track deflection scheme of a charged particle inside the FOOT magnetic spectrometer.

curvature is much greater than the length of the magnet l , as seen in figure 3.7, so curvature angle θ could be approximated as:

$$\theta = \frac{l}{r} \quad (3.11)$$

Using the FOOT tracking system is possible to evaluate the entrance angle (θ_1) before each magnet and the exit angle (θ_2) after that, in this why the measurement of momentum is performed as:

$$p = \frac{ZeBl}{(\theta_2 - \theta_1)} \quad (3.12)$$

The expected momentum resolution for the FOOT experiment is at the level of 5% for a particle energy of 200 MeV/u. When using the ECC setup, as seen in equation

2.11, the particle momentum is evaluated from its multiple Coulomb scattering inside the emulsions. Also in this case the expected momentum resolution is of the order of 5%.

3.2.4 Charge identification

The fragments charge is evaluated using both the energy loss and the time of flight measurements in TW detector. These two quantities are related to the particle charge according to the Bethe-Bloch equation (see equation 1.1). As already said ΔE could be evaluated using MSD and TW (section 3.2.1) and TOF by start counter and TW (section 3.2.2). Part of the original work of this thesis has consisted in the development and in the implementation of an algorithm for the measurement of the fragment charge Z , exploiting the TW and SC detectors, as explained in next chapter.

Also the emulsion second section is meant to measure the charge of the fragments. The grain density along the particles trajectory is almost proportional to the particle energy loss over a certain range, above which a saturation effect occurs. By keeping the emulsion at a specific temperatures condition this effect can be controlled and, as a consequence, the emulsions become sensitive to particles with higher ionization. The charge separation is then obtained by the correlations between pairs of volume variables.[40]

Chapter 4

Z identification with TW detector

The main goal of the FOOT experiment, as explained in section 2.1, is to measure the fragmentation cross sections for the interaction process of light ions ($Z \leq 8$) at the typical PT energies impinging on different target materials representative of human tissues.

The first step for cross section measurement is the identification of the charge Z and the mass A of the fragments, whose simultaneous measurement uniquely identify a produced nucleus.

This thesis work aims to introduce an algorithm in SHOE to identify the fragment charge Z , on an event-by-event basis, exploiting the energy released in the TW as a function of the TOF information (TW-SC) as it is described in details below in this chapter.

4.1 Bethe-Bloch parametrization on Monte Carlo

The track reconstruction strategy developed for FOOT uses as a seed the fragment charge Z , as measured by the TW. Thanks to the global reconstruction is possible to extract the curvature of the fragments in the magnetic fields, that means also the path length L of the tracks together to their rigidity p/Z and so their momentum, once Z is measured. So, with the adopted strategy, the Z measurement come before the global track.

The idea at the basis of the Z identification (ZID) algorithm, developed in this thesis, is to correlate the measurement of the energy loss in the TW and the TOF for each track that hits the TW to the Z of the track, through a parametrization of the Bethe Bloch formula as a function of time of flight, rather than as a function of β (which instead depends on the path length L measured through the global reconstruction). Therefore, plotting the tracks on an ΔE vs TOF plain, we could assign to each TW hit the Z corresponding to the closest BB curve. Once BB parameters are obtained the experimental fragments produced by the beam on the target can be identified in the same way.

The algorithm has been developed in MC and then tuned on data as will be shown

in this chapter. Four Monte Carlo simulation, produced with FLUKA, to account for different combinations of FOOT setup, beam energy and target, have been adopted to develop and test the ZID algorithm:

- two simulations with complete geometry (therefore with all the detectors foreseen in the FOOT experiment) with different beams, once ^{12}C and once ^{16}O with 200 MeV/u energy impinging on a carbon target.
- two simulations with geometry that reproduces the detectors used during the experimental data collection of April 2019 at the GSI (Gesellschaft fur Schwerionenforschung, Darmstadt, Germany) laboratory (start counter, beam monitor, target, vertex and TW detector) with an ^{16}O beam at 200 MeV/u and 400 MeV/u impinging on a carbon target.

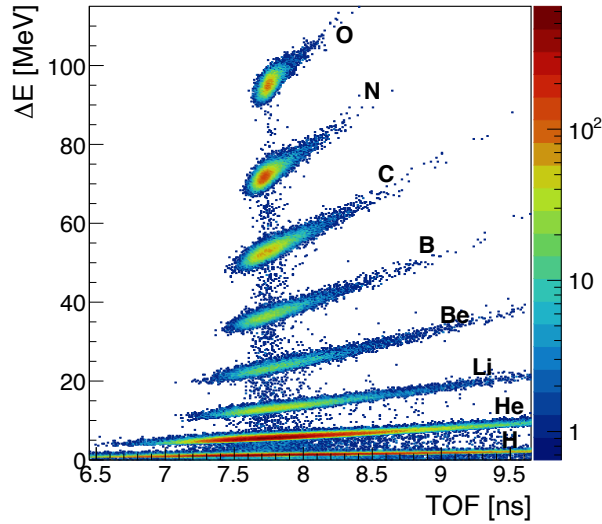


Figure 4.1. Energy loss in MeV vs time of flight in ns for fragments detected by TW detector using Monte Carlo true simulation of a ^{16}O beam with energy 200 MeV/u impinging on a C target (asking for only primary fragments).

The first step is to describe the trend of the Bethe-Bloch curve (eq. 1.1) in our Time of Flight interval considering that:

$$TOF = t_{tw} - t_{sc} = L/(\beta c) \quad (4.1)$$

with L the length between the start counter and the scintillator wall and βc the velocity of the fragment.

In figure 4.1 the energy loss in TW vs TOF is shown for MC simulation of a ^{16}O beam with energy 200 MeV/u impinging on a C target. The eight regions corresponding to the eight charges of the oxygen fragments are easy to identify. In this case only the primary fragments (born from the first interaction between beam ions and the target) are considered. From that plot, and similarly for the others in appendix A, the β is estimated for a straight beam in the TOF interval in which there are almost

Simulation	Beam Energy [MeV/u]	L [m]	TOF [ns]	β
GSI	400	2.10	9.5-12.0	0.58-0.74
GSI	200	2.10	12.0-16.0	0.44-0.58
Full Setup	200	1.30	6.5-10.0	0.43-0.67

Table 4.1. β intervals of interest considering a fixed maximum value of L between SC and TW and the most populated TOF region in GSI and Full Setup simulations.

all the events. In table 4.1 are reported the β intervals calculated for all the different simulations we have using formula 3.5. Taking into account the β values, the energy loss inside the detector is directly proportional to $1/\beta^2$ and in our case to TOF^2 , far away from MIP region that occurs for $\beta \simeq 0.95$, as already said in section 1.1.1. At this point for each region (and so for each charge) in figure 4.1 we have a distribution easy to fit with Bethe-Bloch formula. Result is shown in figure 4.2. In

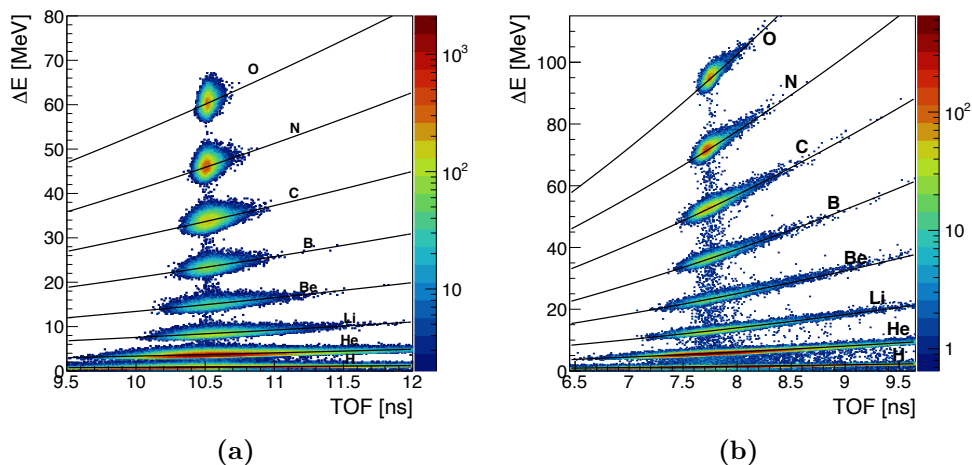


Figure 4.2. In panel (a) Bethe-Bloch parametrized curves superimposed to energy loss in MeV vs time of flight in ns for fragments detected by the TW detector using Monte Carlo true simulation of a ^{16}O beam with energy 400 MeV/u impinging on a C target in GSI setup configuration. In panel (b) the same plot using Monte Carlo true simulation of a ^{16}O beam with energy 200 MeV/u impinging on a C target in full geometry setup.

appendix A are reported plots like 4.2 for all the simulations available in SHOE.

4.1.1 Tuning of the Monte Carlo on Data

In figure 4.2 true Monte Carlo simulations are shown, in which only primary fragments generated inside the target have been considered, in such a way to have the clearest possible situation for the parameterization of the BB curves. After this initial step, to make the Monte Carlo reconstructed as truthful as possible, a gaussian smearing in energy loss and time of flight has been introduced inside the simulation. This Monte Carlo Reconstructed was made using the resolution curves obtained thanks to the various detector calibration data acquisitions at the Centro Nazionale di

Adroterapia Oncologica (CNAO - Pavia, Italy) with carbon beams of three energies (115 MeV/u, 260 MeV/u and 400 MeV/u) and with a 60 MeV proton beam.

For each irradiated point charge collected was calibrated and converted to energy release, then the energy resolution was evaluated for each layer individually and for the whole TOF wall by combining the information of both layers. The resolution obtained is overall below $\sim 5\%$. Figure 4.3(a) shows the time of flight resolution

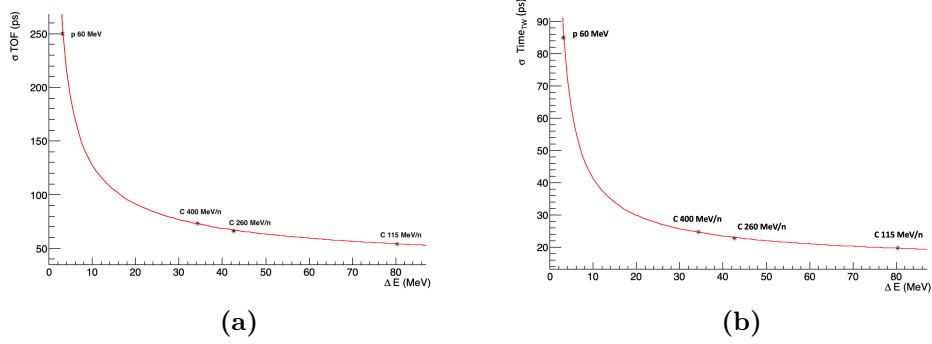


Figure 4.3. In panel (a) Time of flight resolution expressed as the standard deviation of the difference in the reconstructed hit TOF distribution of the two TW detector layers. In panel (b) time resolution considering only TW measurement.[50]

obtained during the same calibration tests at CNAO. The time resolution between the two layers, considering only TW measurement (see figure 4.3(b)), achieved with carbon ions is between 20 ps and 40 ps. The best performance was achieved, as expected, with 115 MeV/u ions, when a higher energy is released. An average time resolution of ~ 85 ps was achieved with proton beams between the two layers.

In order to extract the TOF resolution over the whole ΔE range a fit with the function:

$$\sigma_{TOF} = \frac{p0}{\Delta E} + \frac{p1}{\sqrt{\Delta E}} + p2 \quad (4.2)$$

has been performed. In order to have a more reliable Monte Carlo Reconstructed simulations we have to take into account also the Pile-Up effect in the TW detector. Two or more fragments of the same event are piled-up when they hit simultaneously the same TW bar. Even if a real digitization and modeling of the signal is not yet present. The above treatment allows to have a MC more similar to reality that gave the result shown in figure 4.4 of Energy loss by the fragments as a function of their TOF: the Bethe-Bloch curves obtained with MC truth are superimposed in the plot.

4.2 Charge assignment

The method implemented in the SHOE software to assign the charge to the pair lost energy-flight time is the *bisection* one (explained in appendix B). Being the Bethe-Bloch curves in the considered TOF interval of increasing monotone functions (see section 4.1), the distance function of a ΔE -TOF point from the curve always admits a minimum. This minimum can be found using the bisection method to determine the zero of the derived function of the distance. Distance is then calculated

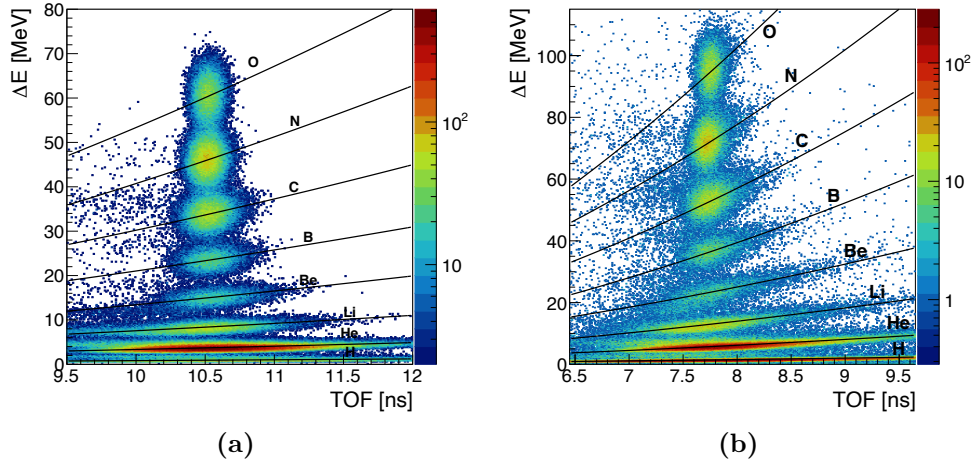


Figure 4.4. In panel (a) Bethe-Bloch parametrized curves superimposed to energy loss in MeV vs time of flight in ns for fragments detected by the TW detector using Monte Carlo Reconstructed simulation of a ^{16}O beam with energy 400 MeV/u impinging on a C target in GSI setup. In panel (b) the same plot using Monte Carlo Reconstructed simulation of a ^{16}O beam with energy 200 MeV/u impinging on a C target in full geometry setup.

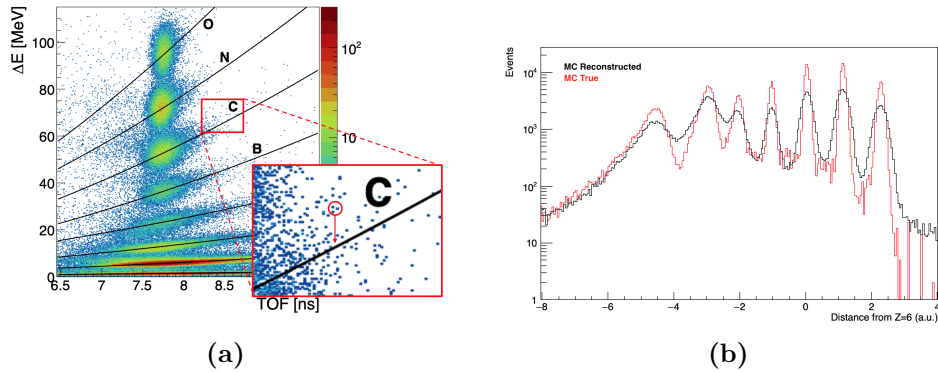


Figure 4.5. In panel (a) explicative zoom on a track assigned to Z=6 BB curve. In panel (b) distance from Z=6 BB curve in True and Reconstructed Monte Carlo simulation of a ^{16}O beam with energy 200 MeV/u impinging on a C target with request of only primary fragments in order to tune the algorithm.

for each point of the ΔE -TOF plane from all the BB curves present for that given beam (see figure 4.5). Finally the charge corresponding to the curve for which the distance is minimum is assigned to that TW hit.

In figure 4.5 (a) is reported a zoom on a carbon track that has been correctly assigned with the explained method, in the same figure panel (b) there is the distance of the tracks from the Bethe-Bloch curve for charge equal to 6, fragments assigned to this Z are those peaked in zero.

4.3 Algorithm performances

To test the goodness of the algorithm, the charge of the fragments given by the Monte Carlo and the reconstructed charge assigned through the identification algorithm have been correlated. In figure 4.6 is possible to see the correlation matrix for Monte

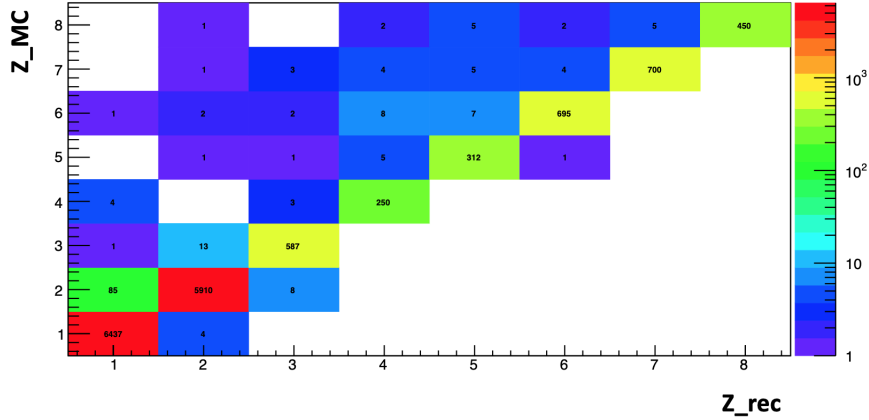


Figure 4.6. Charge identification algorithm performances (wrong Z charge assignment $< 1.2\%$) using full FOOT setup Monte Carlo true simulation of a ^{16}O beam with energy 200 MeV/u impinging on a C target with request of only primary fragments in order to tune the algorithm.

Carlo True, asking only for primary fragmentation. In this case we have a really good agreement between MC charge and our algorithm one, in fact the most populated zone is the diagonal. Misidentified fragments are seen in the non-diagonal position ($< 1.2\%$) they are given by the fact that if, for example, an Oxygen fragment hits the region between two TW bars, and so, leaves less energy inside one single bar, it is identified as an ion with charge < 8 . This misidentification can occur also with high time of flight fragments which are closer to the wrong BB curve. The good performances of the algorithm are worsened by the introduction of other effects like experimental resolutions, secondary fragmentation and pile-up. The overall Z identification performance once these effects are introduced is shown in figure 4.7. Resolution introduces an increment on non-diagonal population but wrong charge assignment stays under 4.8% therefore the algorithm adequately reflects the required precision. In order to correlate Z_{rec} and Z_{true} in this case pile-up have been switch-off otherwise it would be impossible to assign the true charge to a piled-up hit given by the combination of more hits in the same bar. That hit will produce an higher energy release of the single hits and so most probably a wrong Z_{rec} , that will further deteriorate the obtained performances. A clusterize information of the two layers is for this reason necessary in order to minimize pile-up and maximize Z identification performances.

4.4 Critical Aspects

This charge identification method presents some critical aspects, first of all the presence of non-primary fragments produced by the interaction of the primary ones

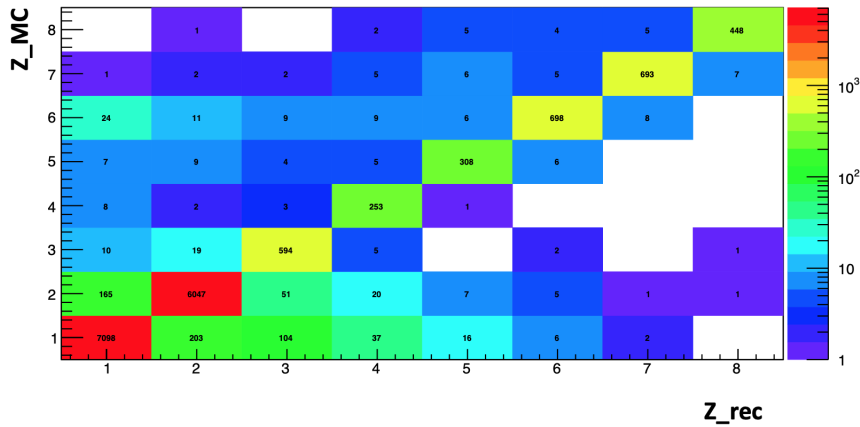


Figure 4.7. Charge identification performances (wrong Z charge assignment $<4.8\%$) using full FOOT setup Monte Carlo reconstructed simulation with no Pile-Up effect (impossible to assign a true MC Z charge in the case of Pile-Up) of a ^{16}O beam with energy 200 MeV/u impinging on a C target.

with the materials of the experimental apparatus. In the case of simulation with the full FOOT setup, the percentage of these superior order fragments is $\sim 30\%$. This $\sim 30\%$ can, in turn, be analyzed in order to identify the origin of the fragments as shown in table 4.2. The previous table shows separate contributions of the various

Detector	percentage
Calorimeter	$\sim 73.7\%$
TW	$\sim 16.1\%$
Magnets	$\sim 6.5\%$
MSD	$\sim 1.7\%$
Inner tracker	$\sim 0.9\%$
Vertex	$\sim 0.2\%$

Table 4.2. Separate contribution of the $\sim 30\%$ non-primary hits of the TW detector in full FOOT setup simulation.

detectors. It is therefore noted that most of the non-primary fragments come from the calorimeter, followed by the contribution of the scintillator and the magnet. These fragments contribute to the worsening of identification as they can present energies and flight times that do not agree with the primary beam.

A further analysis showed as reported in the table 4.3 that of this 30% of non-primary fragments, the majority is entitled to a production order higher than the second. For this reason, the simulation of only the primary fragments was chosen for the parameterization of the Bethe-Bloch curves in order to exclude the effects given by further fragmentation. As regards the simulation with experimental apparatus present at the GSI data socket, the situation improves considerably. The percentage of non-primary fragments drops to $\sim 7\%$ (see table 4.4) thanks to the presence of less detectors and therefore less surrounding matter with which the ions can interact. Another critical aspect is the presence of unwanted neutrons. These are

Order of fragments	percentage
2^o	$\sim 37.3\%$
$> 2^o$	$\sim 62.7\%$

Table 4.3. Order of non-primary fragments that hit the TW detector in full FOOT setup simulation.

Order of fragments	percentage
1^o	$\sim 92.7\%$
$> 1^o$	$\sim 7.3\%$

Table 4.4. Order of fragments with GSI experimental apparatus simulation.

mainly produced by secondary interactions and therefore more present in complete simulations than those with GSI apparatus (start counter, beam monitor, target, vertex and TW detector) in fact 93.2% of 73.7% of the non-primary fragments seen by the scintillator and given by calorimeter are neutrons as shown in figure 4.8 (a). Neutrons, being neutral particles, are not deflected by the magnets and often make

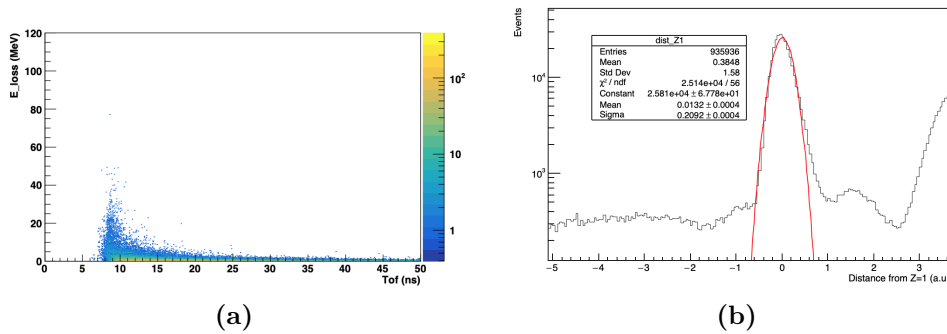


Figure 4.8. In panel (a) non-primary fragments given by calorimeter. In panel (b) cut in Monte Carlo simulation of a ^{16}O beam with energy 200 MeV/u impinging on a C target.

very long distances outside the length of the experimental apparatus, these deposit, in most cases, a very small amount of energy in the TW detector and therefore the risk is that they are assigned to a charge equal to 1 being below the first BB curve. They also have a flight time sometimes much greater than expected (see figure 4.8 (a)) and are distributed as a plateau in the energy loss vs time of flight graph. To get around this problem, as shown in the figure 4.8 (b), is possible to fit the peak centered in zero of the distribution of the distance from the $Z = 1$ BB curve with a Gaussian function and exclude from the assignment to this charge all those fragments out of 5σ at the left of the mean value.

4.5 Moving from Simulation to GSI data

One of the two main topics of this thesis work is the analysis of the data acquired in 2019 in GSI laboratory (Gesellschaft für Schwerionenforschung, Darmstadt, Germany) with a partial set-up of the final FOOT detector (figure 4.9). The experimental

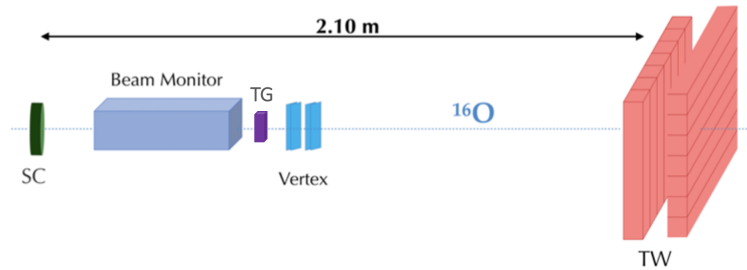


Figure 4.9. Schematic view of the GSI experimental setup.

landscape consists on a ^{16}O beam at 400 MeV/u energy impinging on a 5 mm thick Carbon target ($\rho = 1.83\text{g}/\text{cm}^3$). The on-work detectors were: start counter, beam monitor, vertex and TW.

The distances along the Z axis were fixed and the TW could translate along X-Y axes. To apply the charge identification algorithm to this data has to be considered the different distance between Start Counter and TOF wall (that obviously changed the time of flight mean value, as already said in section 4.1). The employment of a reduced setup with respect to the full FOOT setup implies a decrease in the secondary fragments born from the interaction of the primary with the interposed matter (see section 4.4).

The objective of the test beam carried out at GSI was to provide more data for TW detector energy calibration and perform some fragmentation measurements, so the data set includes acquisitions both without (calibration run) and with target (fragmentation run). Four fragmentation data samples were collected and are available inside the FOOT software:

- Run 2239
- Run 2240
- Run 2241
- Run 2251

Is also available in SHOE the calibration data taking (Run 2242) that consist on 20.000 events acquired without target, spanning a cross region on the TW detector.

In next subsections are discussed in detail some preliminary steps that have been done in order to apply charge identification algorithm to GSI data in SHOE.

4.5.1 Implementation of the detector calibration

A scintillator is a material that exhibits *scintillation*, the property of luminescence, when excited by ionizing radiation (i.e. re-emit the absorbed energy in the form of

light). The WaveDAQ (see section 2.3 *Plastic scintillar wall*) samples the waveform of the signals at both ends of the bar at 5 Gsample/s. The charge from the integral can be extracted offline from the signal thus sampled and the time is measured with a CFD technique (Constant Fraction Discrimination¹).

For the calibration in charge the quantity in 4.3 is considered in order to minimize the dependence of the energy release by a TW hit on its position along the bar. To go back from the total charge thus obtained to the energy released by a hit again, as for the TOF, the MC information of the energy released by the different fragments in the TW is exploited. Being the plastic scintillators of organic scintillators, they are strongly affected by the quenching predicted by Birks (see appendix C) and therefore the dependence between total charge and released energy will not be linear but will be governed by Birks' law.

$$Q_t = \sqrt{Q_A Q_B} \quad (4.3)$$

where Q_A and Q_B are respectively the charges collect by the left and the right side of the detector's bar. Once this quantity is retrieved, it is possible to obtain mean and sigma values of the charge peaks corresponding to the charge of the fragments (see figure 4.10(a)) and subsequently plotting them according to the expected energy release. Figure 4.10(b) displays an example of the energy calibration curve obtained for a reliable position of the front layer of the TW. What can be seen is that the light output of the bar is reproduced by the model. Anyhow, inspecting the low energies, small discrepancies can be observed between the model and the curve. In fact it was not possible to perform a good fit to retrieve the average charge value due to the fragments with charge 1 because, during the data acquisition, there was an energy threshold that cut a large part of them. The TW energy calibration was done at

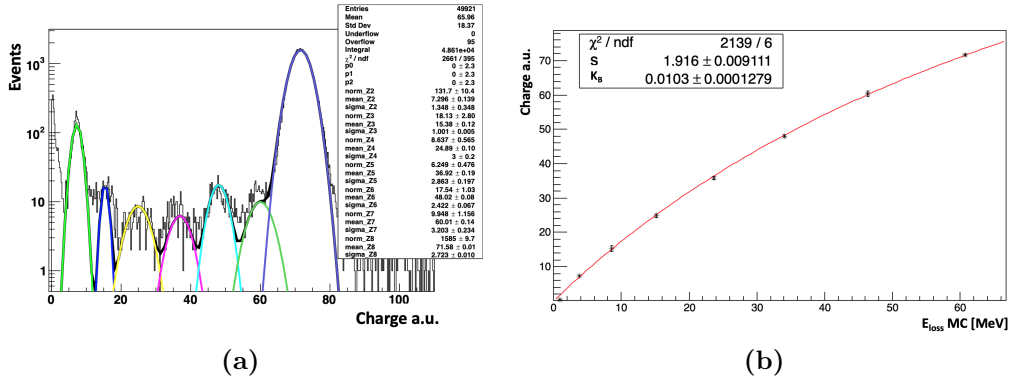


Figure 4.10. In panel (a) is shown the performed fit for charge peaks from data acquisition at GSI of a ^{16}O beam with energy 400 MeV/u impinging on a C target. In panel (b) the Birks fit that correlates charge acquired to the expected energy loss in the Monte Carlo simulation.

the CNAO by irradiating the different x and y bars at their center with beams of different type and energy (as already said in section 4.1.1). From the calibration

¹Constant fraction discrimination (CFD) is an electronic signal processing, it consist in finding a maximum of a pulse by finding the zero of its slope.

it was realized that despite the quantity 4.3 being used, the total independence from the position is not verified as expected and that the response in charge of the bars varies up to 10% moving from the center to one end of the bars. To take this variation into account and to have a better resolution in energy of the final detector, which corresponds to a better identification in charge of the fragments, it was decided to perform a position-by-position calibration going to irradiate all 400 crossings (20×20 bars). This complete calibration will be done in the future, for now, due to lack of time, only some positions (see figure 4.11) have been calibrated (each position must be irradiated with different beams of different energy). In figure

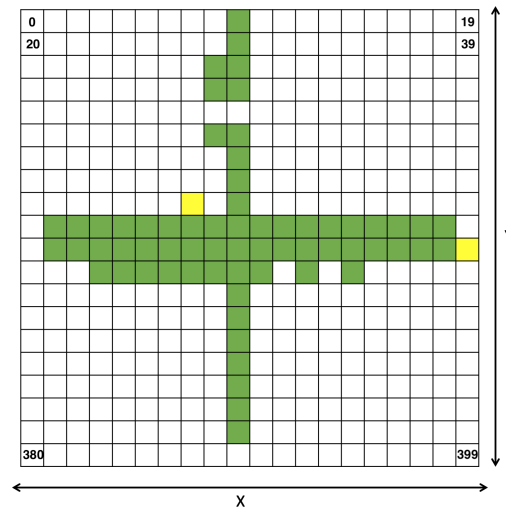


Figure 4.11. TW detector Energy calibration map: in green are highlighted good positions, in yellow positions with sufficient statistic but no good Birks curve. Each position is a $2\text{cm} \times 2\text{cm}$ square.

4.11 is shown the TW schematic map, not all the detector area is highlighted in green, this means that in the case of positions with insufficient statistics (in white) or in which the Birks curve could not adequately represent the data (in yellow), there is an unusable detector square.

To solve this problem the calibration has been extended to the not-calibrated position filling empty ones with the average of the calibrated positions' parameters of the same bar/layer. Memorizing then the two fit parameters of Birks' law (scintillation efficiency and Birks parameter) in a map that connects them to the position they belong to (0-399 by figure 4.11) for each layer it has been possible to implement the calibration inside the FOOT software. This leads to a calibration essentially per bar, where only a few positions really have their own independent calibration. Despite this, part of my job was to set up the reconstruction software in SHOE to manage a calibration of the 400 positions.

Once the kinetic energy of the beam is known, the time of flight can be calibrated position-by-position simply by rescaling the difference between the times obtained between SC and TW (see equation 4.4) to the time of flight of the MC simulation associated with the experimental setup of the GSI.

$$TOF_{raw} = \frac{(T_A + T_B)}{2} - T_{SC} \quad (4.4)$$

where T_A and T_B are respectively the times taken at right and left side of the detector's bar and T_{SC} is the time provided by the start counter. In figure 4.12 the comparison between raw time from eq. 4.4 in panel (a) and final flight time scaled to MC in panel (b). Both, energy and Time of Flight calibration given from CNAO

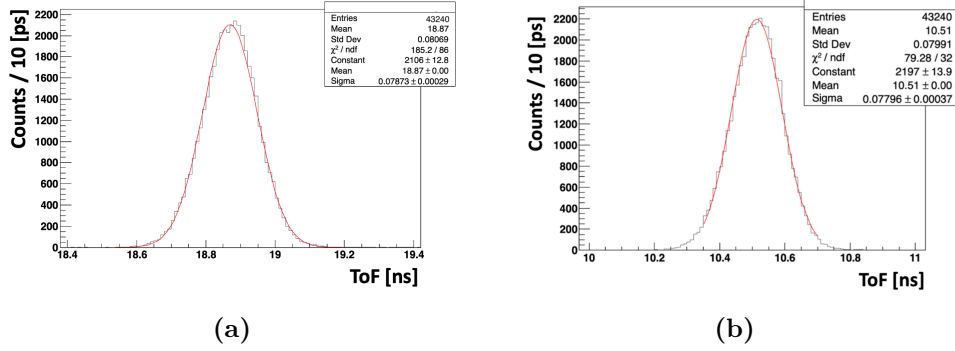


Figure 4.12. In panel (a) raw time of flight from data acquisition at GSI of a ^{16}O beam with energy 400 MeV/u impinging on a C target. In panel (b) final flight time scaled to MC expected one. Time of flight resolution is $\sigma_t \sim 78\text{ps}$

data sets, were checked out comparing them to a bar-by-bar standalone calibration made using GSI fragmentation data. The choice of making this GSI standalone calibration on a bar basis was given by the few statistics available. It is clear from

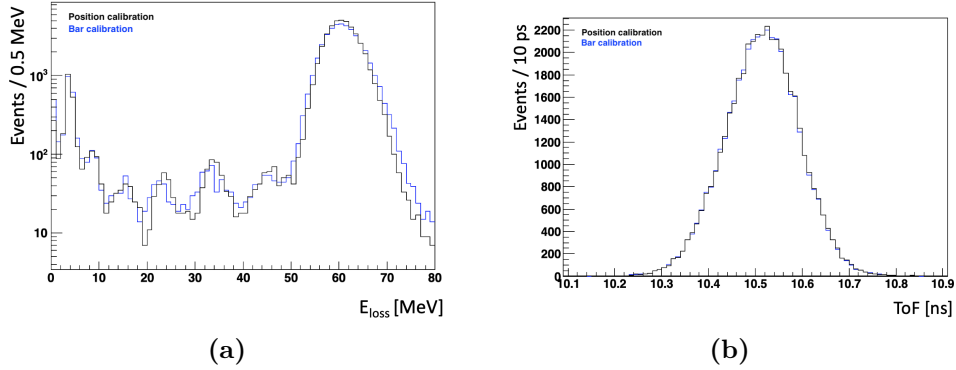


Figure 4.13. In panel (a) comparison between energy calibration per bar (blue) and per position (black) of data acquired at GSI of a ^{16}O beam with energy 400 MeV/u impinging on a C target. In panel (b) same comparison but regarding time of flight.

figure 4.13 that the calibrations are in agreement, in particular with regard to flight time. The only difference is that, as expected, the one made per bar shows a slightly worse resolution since it cannot take into account the variation of the calibration in different positions of the same bar for a limited statistic. For this reason the position-by-position calibration is preferable despite the considerable amount of data required to implement it in SHOE (400 positions each layer, each with its Birks parameters for energy and its own shift parameter for time compared with only 20 bars for each layer). This comparison however allowed the validation of the method

used.

4.5.2 Ghosts management

The problem of ghosts represents a major issue in the charge identification procedure, since it can introduce a non-negligible uncertainty in the calculation of fragment yields and, eventually, fragmentation cross sections. Suppose that two particles impinge at almost the same time on two separated positions of the TW, turning on 4 different bars (2 per layer). The resulting situation is displayed in figure 4.14. In this situation, since the corresponding bars provide both charge and TOF

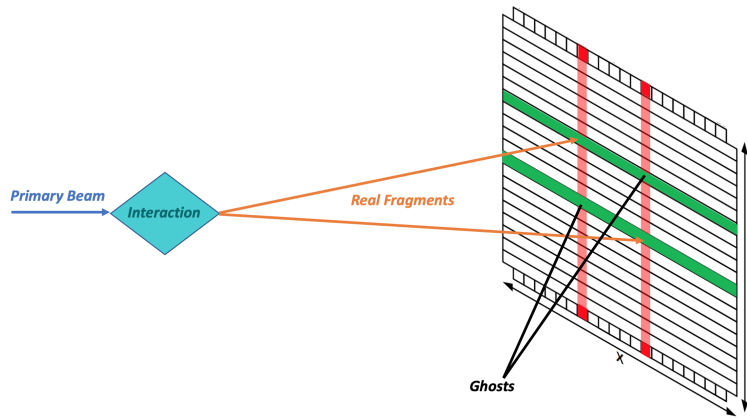


Figure 4.14. Visualization of how TW detector’s ghost events are created. The colored bars are the ones switched on in the front (green) and rear (red) layer.

data in the observed event, the software will identify all the 4 possible crossings as hit positions. This results in the addition of two spurious “particles” to the charge spectra. These points are likely to contribute to the background since the corresponding TW positions were not actually hit and, thus, the corresponding bars can register very different charge and time data. Ghosts have been managed on an

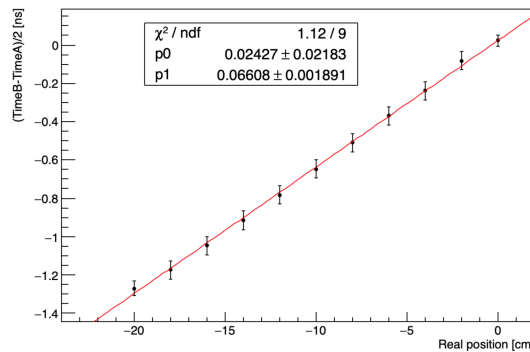


Figure 4.15. Linear fit over $(T_B - T_A)/2$ vs the the average value of the position along the bar during a GSI calibration run in April 2019. The slope $p1$ gave us the value of the inverse propagation velocity inside the TW detector.

event-by-event basis exploiting the reconstructed position along the bar from time

differences at the bar edges using the following equation:

$$Pos = \frac{T_B - T_A}{2 \frac{1}{v_p}} \quad (4.5)$$

where $1/v_p = 0.066 \pm 0.002$ ns/cm is the inverse of the light propagation velocity inside the scintillator detector. This velocity has been extracted thanks to the TW GSI calibration run (2242, see section 4.5) in which some bars were irradiated in different positions. Plotting the TW hits semi-difference in time $((T_B - T_A)/2)$ vs the the average value of their position along the bar as in figure 4.15 it was possible to perform a linear fit $((T_B - T_A)/2 = p1 \cdot Pos + p0)$ in which the inverse of the velocity corresponds to the slope.

Thanks to the same run also the position resolution has been studied. In fact, as can be seen in figure 4.16 (a), the reconstructed position of fragments is clearly distinguishable. σ_{Pos} , reported in figure 4.16 (b), has a mean value < 8 mm that is less than a bar cross of 2 cm.

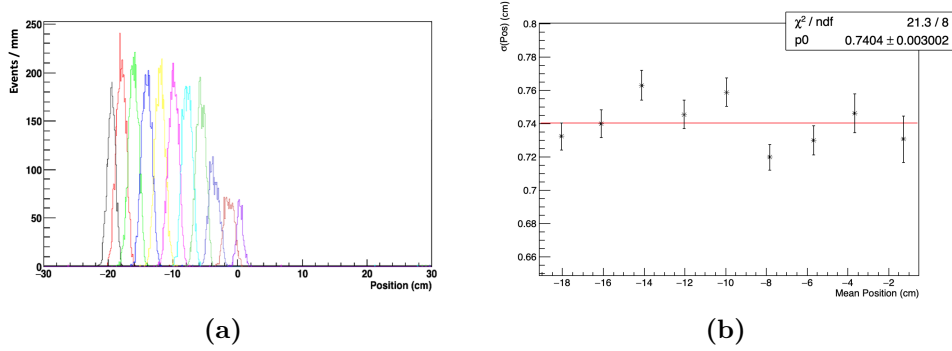


Figure 4.16. In panel (a) positions of the calibration run’s particles with GSI configuration in April 2019, the beam was shifted covering an half-cross of the TW detector. In panel (b) linear fit over σ_{Pos} of each peak of the same calibration run.

4.6 Final result on GSI 2019 data

After the implementation within the SHOE software of the data resolutions, the calibration of the energy loss in TW and of the TOF, the introduction of the charge identification method and the management of the ghosts, we finally have all the necessary elements to proceed with the offline study of the data acquired by FOOT at GSI in April 2019.

Three fragmentation runs (2239-2240-2241) gave consistent results from the analysis and were therefore merged into a single file; the last one (run 2251), instead gave a different raw time (as reported in table 4.5) due to a change in cables during the data acquisition. For this reason it needed a dedicated time of flight calibration (see section 4.5.1) before merging with the others to have the maximum possible statistics. In figure 4.17 is reported the comparison between data energy loss in the scintillator wall and Monte Carlo reconstructed one which takes into account

Data sample	Raw TOF [ns]
Runs 2239-2240-2241	18.760 ± 0.002
Run 2251	22.300 ± 0.001

Table 4.5. Raw time of flight from eq. 4.4 given by the different data samples.

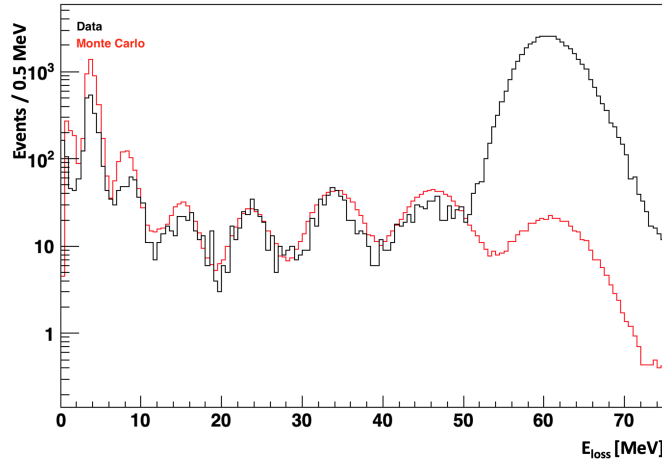


Figure 4.17. Data energy loss in TW (black) compared to Monte Carlo reconstructed one (red).

experimental resolutions. It is possible to see the good agreement between the two except for proton and oxygen peaks (the first and the last ones), in fact in the simulation there is a trigger to exclude events that don't make fragmentation in order to discard a very huge amount of non-needed informations. During the data acquisition a Minimum Bias trigger based on the signal presence in the SC was used and no fragmentation trigger has been implemented, so it wasn't possible to exclude non-fragmented events: this is the reason why there are a large number of ^{16}O from primary beam (in MC simulation instead are considered only ^{15}O and ^{14}O given from ^{16}O fragmentation following the emission of one, or more, neutrons).

For what concerns the protons in the GSI data taking, to avoid DAQ problems for the event size, apart from implementing a zero suppression logic, a threshold has been inserted on all bars, with the exception of the two central ones (id 9, see figure 5.6). This threshold removes most of the protons, in addition to those physical (neutrons) or electronic noise events comparable to the passage of a proton. The distributions in Energy loss of the calibrated data were used to implement this situation also in the MC in order to make it more reliable for the measurement of efficiencies explained in the next chapter. Also the dead bar (id 4 of the front layer in figure 5.6) during the data taking, was "turned off" in the MC.

In any case, the TW detector is not optimized for the measurement of protons. To measure a release of energy ranging from $Z = 1$ to $Z = 8$, with a limited dynamic range, was preferred to favor heavy ions rather than protons whose cross section is production impact will be measured by the setup with an emulsion spectrometer. Passing now to the flight time, the result obtained is reported in the figure 4.18 (a)

which shows the evident agreement between the forecast given by the appropriately tuned Monte Carlo and the calibrated data.

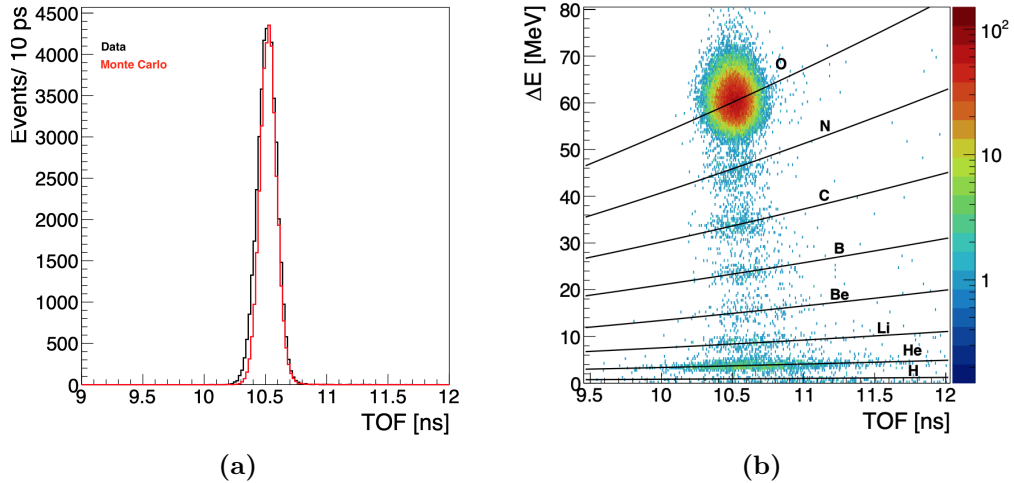


Figure 4.18. In panel (a) Data fragments time of flight (black) compared to Monte Carlo reconstructed one (red). In panel (b) Bethe-Bloch parametrized curves superimposed to energy loss in MeV vs time of flight in ns for fragments detected by the TW detector during GSI 2019 data taking.

Having therefore correctly calibrated the data and having obtained a good result from the comparison with Monte Carlo, we proceeded with the charge identification algorithm. The figure 4.18 (b) shows the data in a graph of lost energy vs flight time thanks to which, with the use of the implemented algorithm and the Bethe Bloch curves previously parameterized, it was possible to assign the corresponding charge to each fragment.

We, then, obtained the result shown in figure 4.19 where the same figure 4.17 graph of the energy lost in the TW detector for the data is reported but with different colors for each charge thanks to the identification algorithm implemented.

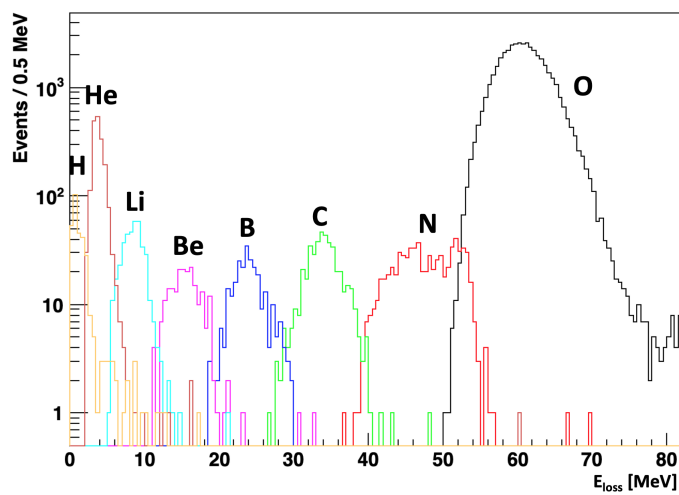


Figure 4.19. Data Energy loss in TW plotted with different colors for each fragment charge thanks to the charge identification algorithm.

Chapter 5

Fragmentation Cross Sections

In this chapter the data taken in the GSI 2019 campaign with the device explained in the previous chapter will be analyzed. With this apparatus, the only detector capable of identifying the Z of the fragments is the TW, while without magnetic field and an adequate tracking system it is not possible to measure the impulse and therefore to identify the mass of the fragments produced (see section 3.2). The constraint posed by the apparatus together with a limited statistics allows however to analyze the acquired data with the aim of measuring the elemental cross sections (for the different Z of the fragments) integrated in angle and kinetic energy. Moreover, this analysis can be considered as a step-0 for future FOOT analysis corresponding to the future data taken of the experiment.

I'll first introduce the detector alignment procedure and the studies about TW detector angular acceptance. Then I will show the studies on Monte Carlo simulations, once tuned on experimental data, as explained in chapter 4, to be as realistic as possible, about kinetic energy of the fragments and efficiency of the detector. In section 5.3 is reported the algorithm implemented to assign the hits of the two TW layers to the same track. After that, I will illustrate the technique used to perform the first cross section measurement on the FOOT data and the result obtained. At the end of this chapter there is also a short discussion about what has to be improved and what is still missing to perform a final measurement of the elemental cross sections.

5.1 Detectors alignment and angular acceptance

In order to correctly measure the angles of the emitted traces and estimate the angular acceptance for the measurement of the integrated cross section, the detectors must be properly aligned taking into account small shifts and rotations of the individual detectors with respect to the global FOOT reference in which the beam is along Z axis and centered at $X, Y = (0, 0)$. In particular, as shown in figure 5.1, the Beam Monitor turned out to be rotated with respect to the beam axis, having observed at the end of the setting given a thickness of 6 mm under the edge positioned at -35.05 cm. For this purpose the Run 2242 (calibration one, in which the target was not present) was used. Figure 5.2 shows the angular distribution of the traces reconstructed by

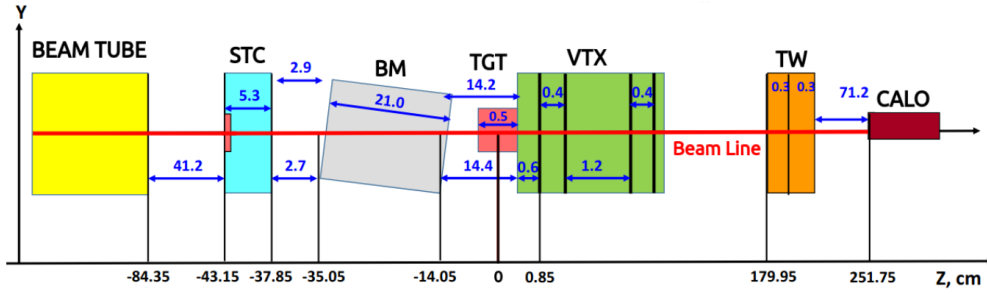


Figure 5.1. Schematic view on the Y-Z plane of the GSI experimental setup.

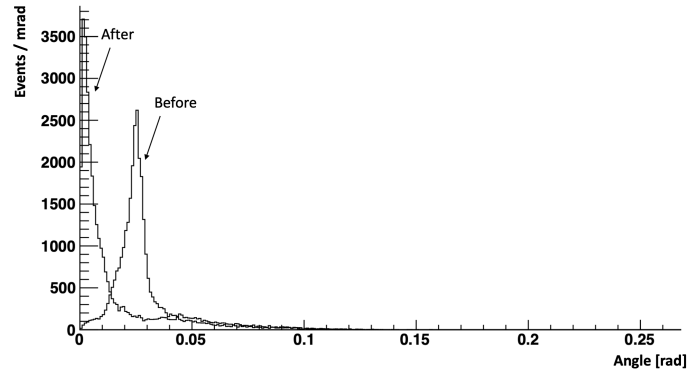


Figure 5.2. Polar angle of Beam Monitor tracks in radians before and after the reference frame's tilt.

the BM, in the global reference frame, before and after the alignment procedure. To align BM and TW, the projection of the traces of the BM on the TG and TW planes was exploited: in figures 5.3 panel (a) and (b) the distributions of the beam in X and Y on the two planes taken into consideration are shown after the alignment procedure. From the distributions shown, can be seen how the beam structure, even if not Gaussian, is centered at $(x,y) = (0,0)$ in the global reference frame. The broadening of the distribution on the TW located at 180 cm from the TG shows a divergence of the beam of ~ 5 mrad (about 0.3°) in X and Y.

Subsequently we proceeded with the study of the acceptance angle of the TOF wall in order to know the integration angle for the cross section measurement. Figure 5.4 shows a simple diagram of what we want to achieve. In this case we had to consider that the target was not perfectly centered with respect to the scintillator wall, in fact, as it is explained in figure 5.5, the TW center was a little bit shifted. The $(0,0)$ cm position in XY axes of the global reference frame corresponds to the $(1,1)$ cm position in the detector's one. This choice made it possible to irradiate the TW at the center of the bars with Id 9 of the front and rear layer (see figure 5.6). This relative displacement between TG and TW and the beam structure, shown in figure 5.5, impose a limit on the angular acceptance of the set-up. Choosing to select those traces with projection on the TG in the symmetrical interval $[-0.7,0.7]$ cm, shown in figure 5.3 (a) with red dotted lines, both in X and in Y, the maximum angular acceptance is fixed at $\Delta\theta = 5.7^\circ$.

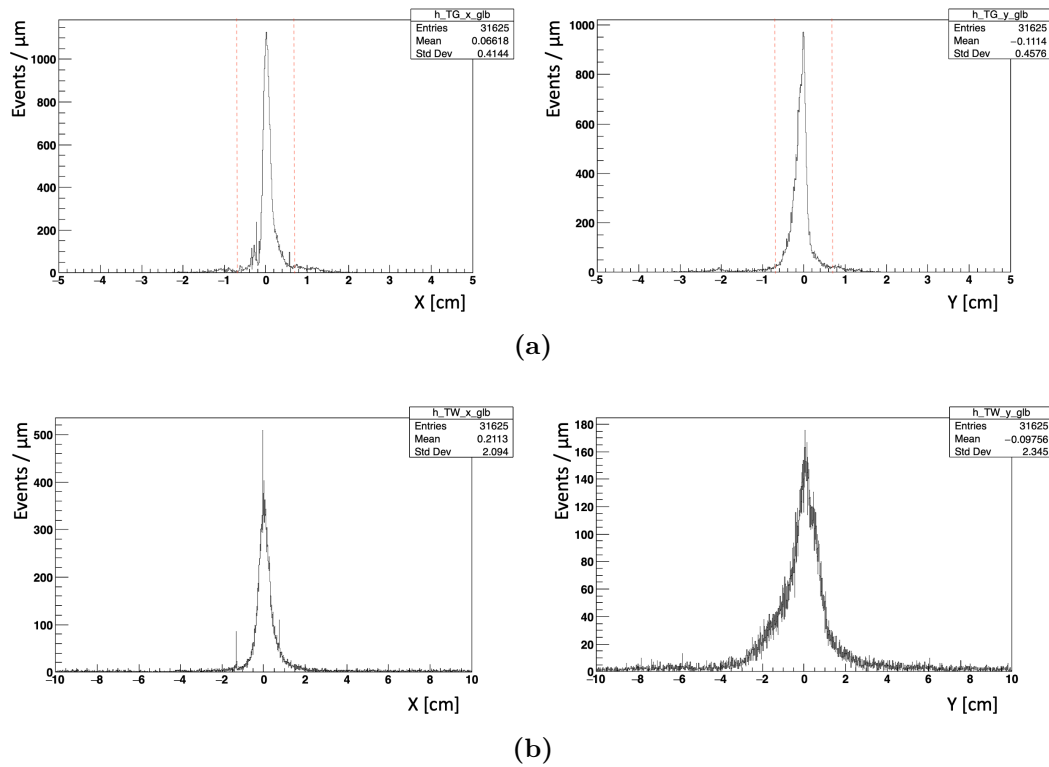


Figure 5.3. GSI 2019 data taking: beam dimensions projected along XY axes. In panel (a) the projection on target in which is highlighted with red dotted lines the interval $[-0.7, 0.7]$ cm. In panel (b) the projection on TW detector that shows the beam divergence.

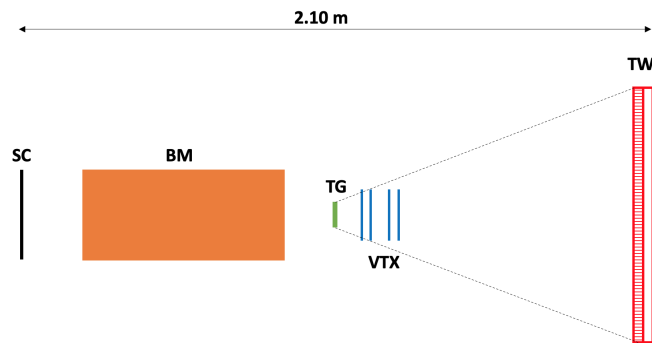


Figure 5.4. Schematic view of the angular acceptance with the GSI experimental setup.

5.2 Monte Carlo simulation and detector efficiency

One of the main factors necessary to obtain a cross section measurement is that of the detector *efficiency*.

In general, efficiency is a measurable concept, quantitatively determined by the ratio

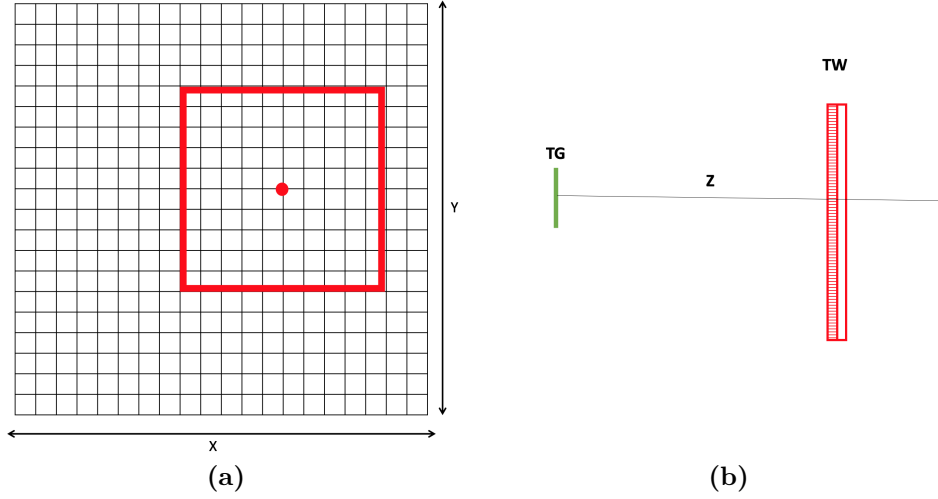


Figure 5.5. In panel (a) TW scheme view in XY plane with target and beam spot size projection highlighted in red on it. In panel (b) is shown the same scheme in YZ plane.

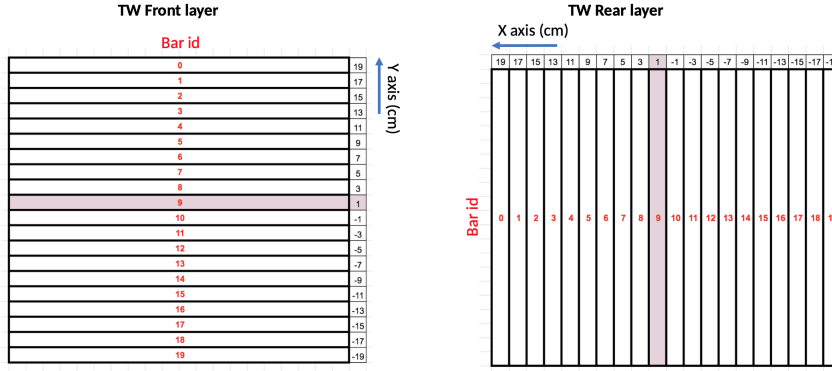


Figure 5.6. Schematic view of the TW in which is highlighted the correlation between the bar-Id and the detector position in X-Y plane.

of useful output to total input. So in our case:

$$\varepsilon(Z) = \frac{N_{TW}(Z)}{N_{TG}(Z)} \quad (5.1)$$

where $N_{TG}(Z)$ are the fragments with charge Z produced in the nuclear interaction between primary beam and target material (TG), that exit the target and that enter in the TW acceptance, while the $N_{TW}(Z)$ are the fragments with charge Z detected by the TW. This number varies between 0, when TW detector cannot identify any of the fragments emitted, to 1, when it recognizes all the generated fragments. To extract the efficiency, the Monte Carlo generated with FLUKA of a beam of ^{16}O at 400 MeV/u on carbon TG, which reproduces in detail the GSI geometry, as discussed in the previous chapter, was used. Obviously the efficiency has to be measured in the detector angular acceptance because is not possible to ask our detector about a

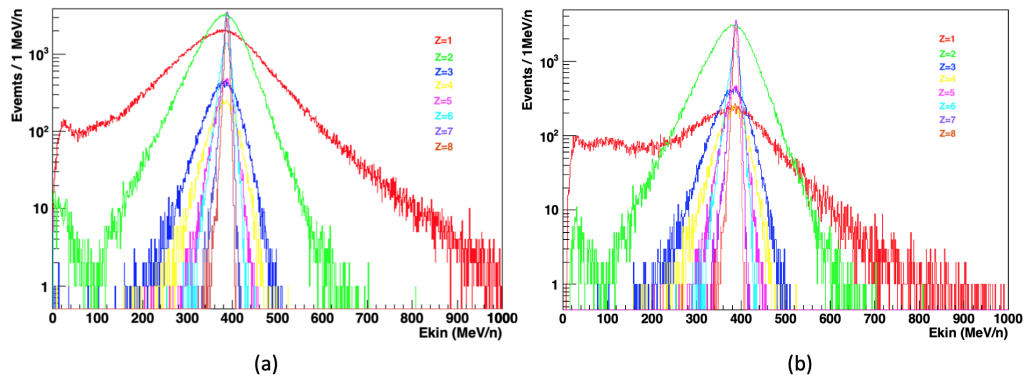


Figure 5.7. Kinetic energy distribution of the fragments produced by the primary beam particle interaction with the graphite target for the for the GSI simulation with ^{16}O beam at 400 MeV/u. In panel (a) the distribution of the fragments emitted in the acceptance angle region, in panel (b) the kinetic energy distribution of the fragments that hit the scintillator wall.

fragment emitted with an angle out of $\Delta\theta$.

In figure 5.7 panel (a) are reported the kinetic energy distributions (each charge with a different color), as extracted from MC, of the fragments produced by the interaction of the primary beam ions inside the target inside the acceptance angle. For each track the angle of emission is taken as the polar angle of the initial momentum from MC truth. From the same momentum and the mass information, extracted also from MC truth, is calculated the production kinetic energy used in the distributions of figure 5.7, using equation 2.3.

In order to not depend on fragmentation in FLUKA in the extraction of the efficiencies, only the primary fragments produced in the target have been considered. Secondary fragmentation in the target, in the detector and surrounding material is in this way removed. Furthermore, in order to account for the kinetic energy lost in the target and not to depend on the fragments produced in target and therein absorbed (most of them coming from target fragmentation), only the fragments produced in target and exiting from it have been considered. Integrating the different kinetic energy distributions shown in figure 5.7 (a) for each Z the $N_{TG}(Z)$ for each fragment have been extracted.

To extract the $N_{TW}(Z)$ the TW reconstructed clusters (two associated hits in front and rear layer), whose associated MC tracks satisfied the same conditions required for the $N_{TG}(Z)$, have been counted, for each Z . In figure 5.7 (b) the kinetic energy distributions of the detected fragments is shown.

$N_{TG}(Z)$ and $N_{TW}(Z)$, and so the corresponding efficiencies, have been extracted in the kinetic energy range [200,600] MeV/u. The integration limits have been chosen accordingly to the kinetic energy distributions of each fragment in data, as shown in figure 5.8. As already mentioned, due to lack of statistics a differential measurement is not possible so the interval has been chosen in order to maximize the available statistic. In such interval the efficiencies for each fragment have been checked to be flat against the kinetic energy.

The result of this efficiency calculation is reported in table 5.1 in which is possible

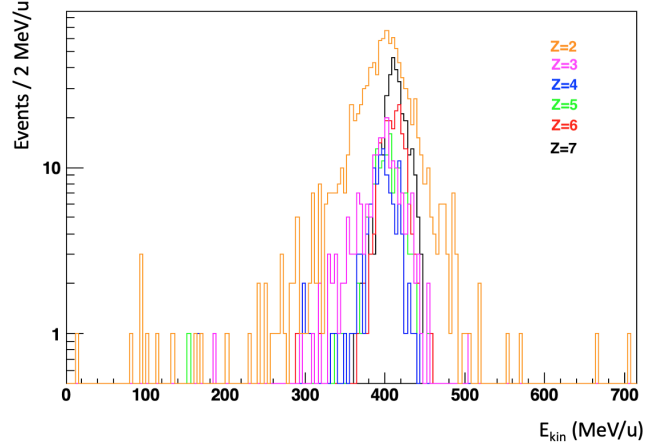


Figure 5.8. Kinetic energy distribution of fragments from GSI 2019 data taking (^{16}O beam at 400 MeV/n impinging on a graphite target).

to notice an increase with increasing charge. Table 5.1 shows the efficiencies for charge fragments between 2 and 7, of interest for the cross sections measurement. Hydrogen efficiency is not reported, reminding that, as explained in chapter 4, in the simulation is implemented the same hardware energy threshold present during the data taking for what concerns the scintillator's bars. Errors on the efficiencies

Element	Efficiency (%)
He	95.56 ± 0.04
Li	96.88 ± 0.10
Be	97.71 ± 0.12
B	98.21 ± 0.10
C	98.77 ± 0.06
N	99.02 ± 0.05

Table 5.1. Elemental efficiencies in percentage from GSI 400 MeV/u simulation.

are calculated using binomial formula as:

$$e_{\varepsilon}(Z) = \sqrt{\frac{\varepsilon(Z)(1 - \varepsilon(Z))}{N_{TG}(Z)}} \quad (5.2)$$

where $e_{\varepsilon}(Z)$ is the error on the efficiency $\varepsilon(Z)$ of charge Z .

5.3 Clustering implementation

Clustering implementation within the SHOE software is fundamental to retrieve the correct number of fragments that hit the scintillator wall. The TW detector, as already mentioned, consists of two matched layers, each of which has 20 bars. Clustering has the task of joining the hits released in the two layers corresponding

to the same fragment. For this purpose a method is implemented that assigns to each hit of a layer the one of the other layer closest to the first. This method is affected by some factors as:

- Spatial resolution
- Secondary fragmentation inside the TW
- Pile-Up effect
- Fragments hitting multiple bars on the same TW layer

These aspects have been studied in detail. The spatial resolution has been obtained with the data acquired at CNAO exploiting the same method explained in paragraph 4.5.2, retrieving the time difference at the TW bars edges. The spatial resolution as a function of the energy released by the beam in the TW is shown in figure 5.9, it is always less than ~ 1.6 cm and for fragments heavier than lithium always less than 8 mm that is better of the bar crossing ($2 \times 2\text{cm}^2$). This assure a good reconstruction of the position of the TW cluster. So in the case of well separated fragments

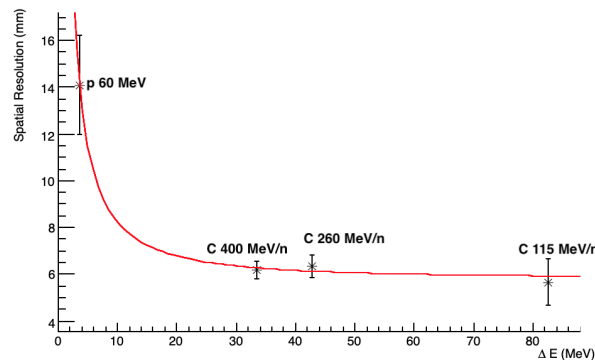


Figure 5.9. Spatial resolution obtained from the TW detector calibration runs at CNAO.

the measurement of the hit position along the bar is the key to disentangle from ghost and reconstruct good TW clusters. In the case of Pile-up and fragmentation inside the TW this is not true anymore. Bad clusters can be reconstructed due to these effects with wrong Z charge assignment by the charge identification algorithm. Also the case of fragments releasing energy in between two bars provides a wrong information about the fragment identity and wrong cluster. These cases have been studied in MC and the results are shown in figure 5.10. The MC showed that in most of the cases such bad events can be avoided using the TW layer with more hit bars to train the clustering, using the Z of these hits as Z of the final cluster. Looking in detail figure 5.10, the first column shows the percentage of total TW events affected by pile-up (25%), below are shown separately the cases in which pile-up occurs only on the front layer and only on the rear layer ($\sim 10\%$ each). Our cluster method manages to resolve these last events. The cases that remain critical are those shown in the fourth column, in which occurs pile-up on both, the front and rear, layers ($\sim 5\%$); in this situation, in fact, is not possible disentangle correctly

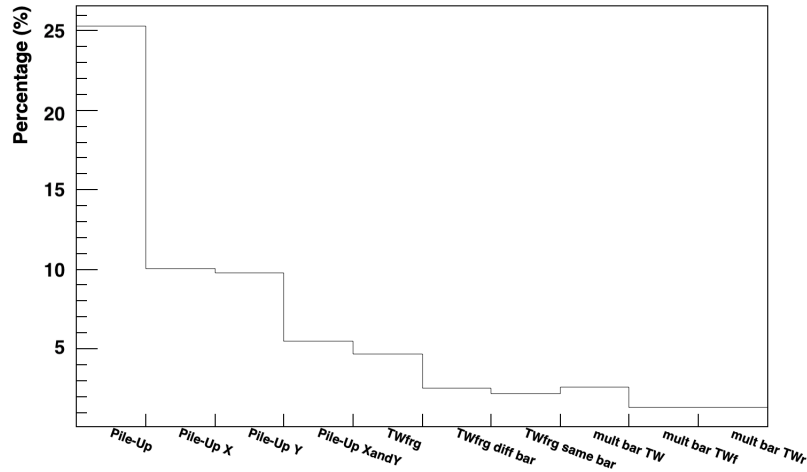


Figure 5.10. Study on the probability of failure of the clustering algorithm carried out using Monte Carlo reconstructed simulation of a 400 MeV/u ^{16}O beam impinging on a graphite target in GSI experimental setup.

the TW hits. A way to further filter this intrinsic background is to use a golden cut requiring same Z for the two hits of the cluster: this selection decreases the total statistics but clean the sample.

A further investigation highlighted the cases in which secondary fragmentation occurs within the TW detector itself ($\sim 5\%$), shown in figure 5.10 column 5. In these cases it was possible to assign the right charge to a fragment, and therefore correlate it with the right hit of the other layer, only if the fragmentation products release energy within the same bar where the original fragment break-up ($\sim 2.5\%$, see column 7 of the histogram). In the event that the secondary fragments, instead, release energy in different bars of the same layer, our clustering fails by assigning a wrong match ($\sim 2.5\%$, see column 6). The last three columns of the histogram in figure 5.10 show a further possibility of error, namely the one that occurs when a fragment releases energy across two bars of the same layer ($\sim 3\%$ equally divided between multiple hit in front or rear layer).

These two last cases of single tracks releasing energy in two (or more) bars of the same layer make the clustering algorithm fails. Also for this cases the request on the same Z in front and layer helps in decreasing this intrinsic background. The separation of the Energy loss for the different fragments extracted after the introduced TW clustering is shown in figure 5.11. The results is very good providing a very strong Z identification, fundamental in the extraction of the fragment yields for cross section measurement as shown in next paragraph.

5.4 Event selection and fragment yields extraction

After having implemented all that is needed for the study of the Monte Carlo simulation and having estimated the efficiency of the detector, we proceed with counting the number of primaries impinging on the target and the identification of the number of fragments detected during the data taking of April 2019 at the GSI.

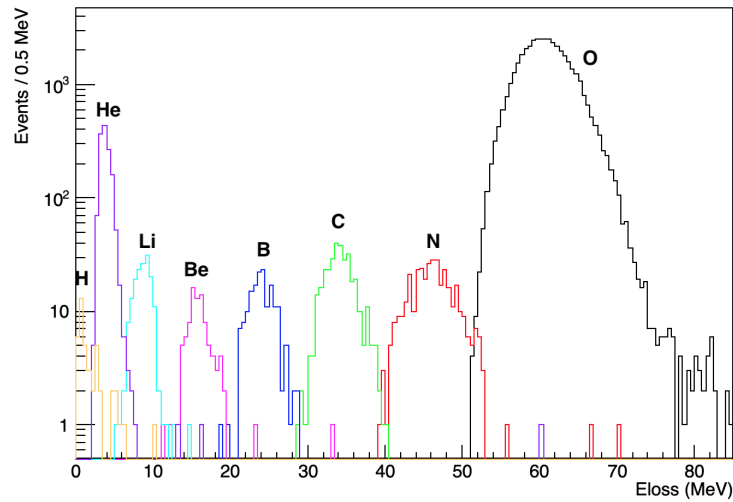


Figure 5.11. Energy loss inside the TW using Monte Carlo reconstructed simulation of a 400 MeV/u ^{16}O beam impinging on a graphite target in GSI experimental setup. The plot shows the charge separation reached implementing our clustering algorithm.

As already said in section 4.6 we have used four data sets and merged them together to have the highest possible statistic.

To complete everything necessary for the cross section measurement, the count of primary ions of the beam interacting with the target is missing.

This number is provided by the Start Counter reminding that the trigger adopted during the data taking was a minimum bias trigger based on start counter good signals (over a fixed threshold in order not to trigger over noise). In figure 5.12

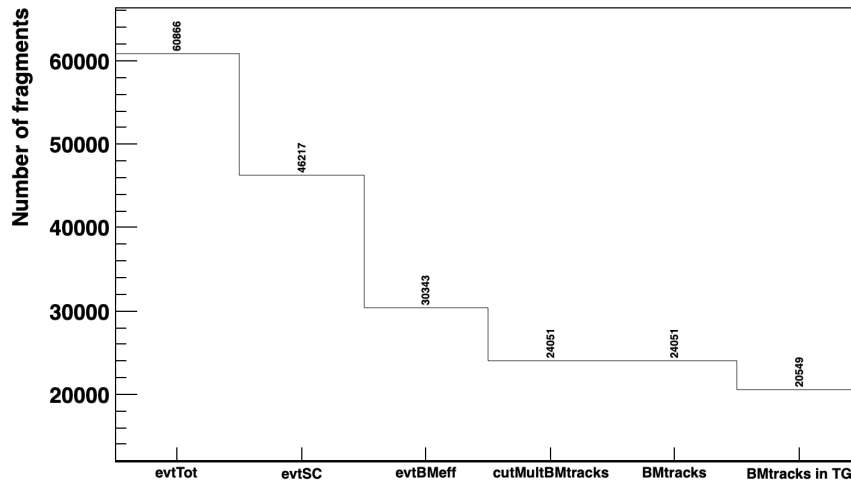


Figure 5.12. Number of events considered to perform the cross sections measurement. The histogram includes all the cuts necessary to clean the data sample.

the number of events is shown in the first bin. Due to problems with the writing of the events by the DAQ some MB events lost the charge and time information

from SC and TW. For these reason such events have been rejected resulting in the number of events shown in second bin. Requiring also on the impinging primaries a good reconstructed track by the beam monitor, excluding the cases of BM multiple tracks (that can be caused by primaries fragmentation in SC), we ended up with the number of events in fifth bin. Finally requiring tracks of BM with projection on the target within our default selection of $[-0.7, 0.7]$ cm in x and y compatible with the selected angular acceptance of 5.7° we got the total number of primaries selected for the cross section measurement.

In correspondence of such event selection, the fragments yields coming from clustering algorithm have been extracted for each Z . The measurement of the yield of the proton is strongly suppressed and biased, as already mentioned, by the high threshold set on TW DAQ. For this reason no measurement of proton production cross section has been performed. The resulting yields are printout in next section together with cross section results.

5.5 Fragmentation cross sections

Considering the discussion in previous paragraphs we have obtained all the necessary to perform a first measurement of the elemental cross sections of ^{16}O beam at 400 MeV/u impinging on a graphite target with the FOOT apparatus. The elemental cross section could be calculated using the following formula:

$$\sigma(Z) = \int_{E_{kinmin}}^{E_{kinmax}} \int_0^{\Delta\theta} \frac{\partial^2\sigma}{\partial\theta\partial E_{kin}} d\theta dE_{kin} = \frac{N(Z)}{N_{oxy} \cdot N_t \cdot \varepsilon(Z)} \quad (5.3)$$

where $\Delta\theta$ is the maximum TW detector acceptance angle (5.7°), E_{kinmax} and E_{kinmin} are respectively the maximum and minimum of the kinetic energy integration range, $N(Z)$ is the number of fragments of a specific charge produced by the beam-target interaction, N_{oxy} is the number of initial ^{16}O ions impinging on the target, as selected in figure 5.12, $\varepsilon(Z)$ is the elemental intrinsic efficiency reported in table 5.1 and N_t the number of target scattering centers per unit surface obtained as:

$$N_t = \frac{\rho \cdot dx \cdot N_A}{A} \quad (5.4)$$

in which:

- $\rho=1.83 \text{ g/cm}^3$ is the graphite target density
- $dx=0.5 \text{ cm}$ is the GSI target thickness
- N_A is the Avogadro's number
- $A=12.0107$ is the graphite mass number

Table 5.2 reports the values obtained for the cross sections for the production of He , Li , Be , B , C and N integrated in the angle $0 < \theta < 5.7^\circ$, together with the measured yields. Final cross sections values are also graphically displayed in figure 5.13.

As shown in the table 5.2 the error is dominated by the poor statistic and range

Element	Integration angle	E_{kin} range [MeV/u]	Yield	σ_{Data} [mbarn]
He	$0^\circ - 5.7^\circ$	200 – 600	940 ± 31	1043 ± 35
Li	$0^\circ - 5.7^\circ$	200 – 600	146 ± 12	160 ± 13
Be	$0^\circ - 5.7^\circ$	200 – 600	77 ± 9	84 ± 10
B	$0^\circ - 5.7^\circ$	200 – 600	107 ± 10	116 ± 11
C	$0^\circ - 5.7^\circ$	200 – 600	183 ± 14	197 ± 15
N	$0^\circ - 5.7^\circ$	200 – 600	281 ± 17	301 ± 18

Table 5.2. Elemental cross sections from April 2019 GSI data taking.

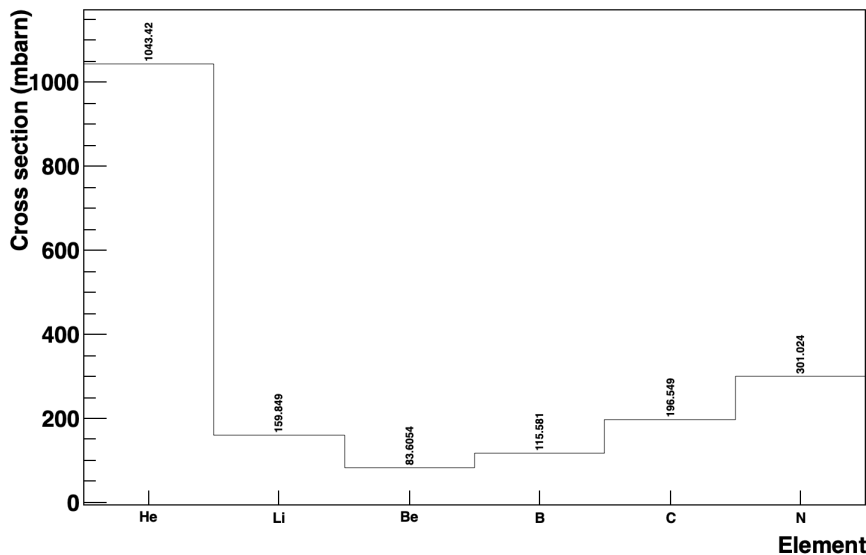


Figure 5.13. Cross sections result on GSI ^{16}O beam at 400 MeV/u data taking graphically displayed.

between 6% – 12% with the exception of the He for which the relative error is $\sim 3\%$. The impact of systematics errors on the precision of the measurement has not been studied in the framework of this thesis. Nevertheless many sources of systematics have to be considered in the future. Different selection criteria of the projection of the beam on TG can be varied with respect at the default value of $[-0.7, 0.7]$ cm and relative position of detectors to be moved inside spatial resolutions. Integration angle can be varied accordingly to the angular resolution and also the kinetic energy range could be modified accordingly to time of flight distributions in data to look for some effect on the final result. Systematics on the charge identification and clustering algorithms have also to be included. For efficiency evaluation a cross check with a MC simulation of fragments of each Z isotropically emitted directly from the target with flat kinetic energy distribution is already in plan. Furthermore some additional corrections to the final cross section have still to be included, as hint in the following section.

It's clear that the values measured are really preliminary and only after performing all the necessary crosschecks, including the additional corrections and a reliable

systematics evaluation, will make sense to compare the results with similar data present in the literature.

5.6 Future corrections to the cross sections measurement

This thesis proposes the preliminary result of the elemental cross sections measured using the apparatus of the FOOT experiment present at the data taking of April 2019 at GSI (start counter, beam monitor, target, vertex and TW detector). In any case, this result can be deepened and improved in the future by the collaboration through some deepest studies of the measure.

In the following subsections two of the studies to be implemented to the work already carried out are presented: the correction of the cross sections considering the charge mixing matrix and the correction for the out-of-target fragmentation.

5.6.1 Charge mixing matrix

Considering the GSI ^{16}O beam at 400 MeV/u simulation, that corresponds to the data set we have, it is possible to correlate in a charge mixing matrix (as the ones in subsection 4.3) the reconstructed charge to the real one. In figure 5.14 is shown

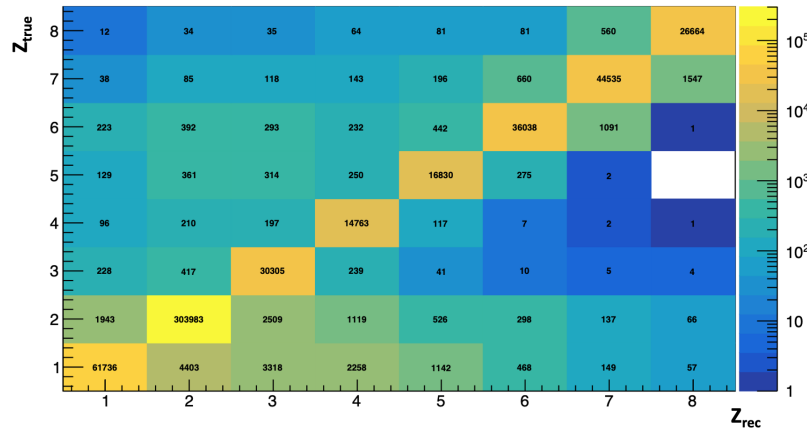


Figure 5.14. GSI ^{16}O beam at 400 MeV/u simulation charge mixing matrix.

the result thanks to which is possible to observe how our charge identification algorithm assigns in some cases a fragment to a wrong Z. As already said it is a small effect (about 2% of wrong assignment in GSI simulation case because of the small percentage of secondary fragments) but it is relevant and our cross sections measurement doesn't take care of it.

Such charge mixing is due to the overlap of the different fragment regions, as shown in chapter 4 figure 4.4 in the Energy loss vs TOF plots, due to experimental resolution. In order to use the Monte Carlo to correct data the comparison of data and MC ΔE and TOF distributions need to be improved as much as possible. Once assured a good MC data matching, MC can be used for such correction because the charge

mixing is something related only to the charge identification algorithm performances and no dependence on the FLUKA MC cross sections is introduced.

5.6.2 Secondary fragments impact

To understand the effect of secondary fragmentation in the acquired data, Run 2242 can be exploited: for this run the geometric configuration of the FOOT detectors is the same of the used run for the data analysis, but without the graphite target. In this way it would be possible to estimate the fragmentation out-of-target and subtract the found contribution to the cross section measurement identifying the produced fragments. Obviously a fundamental step to understand if this measurement can be performed is to check the available statistics.

Conclusions

This thesis reports the work I did regarding the charge identification of the fragments produced by the interaction of the primary beam with the target of the FOOT experiment apparatus using the information acquired by the TW detector. The method implemented also allowed to perform the preliminary measurement of the elemental fragmentation cross sections.

Cross section measurements are the main goal for FOOT (FragmentatiOn Of Target) experiment, funded by INFN (Istituto Nazionale di Fisica Nucleare, Italy). In particular FOOT has been designed to perform measurements of differential cross sections for the production of charged fragments in the nuclear interaction between ion beams (p , ${}^4\text{He}$, ${}^{12}\text{C}$, ${}^{16}\text{O}$) and targets (H , C , O) of interest for charged Particle Therapy and space radioprotection. To this aim, it measures the particles Time of Flight, energy loss and bending in magnetic field, thus allowing to evaluate their velocity, energy and momentum.

My work was focused on the scintillator wall detector, its calibration procedures provide a precise characterization and a really good resolution in time (50-75 ps) and energy ($< 5\%$) that allows achieve good performances for the charge identification algorithm.

Results achieved for what concerns fragments charge identification are fundamental and allows to implement a global tracking algorithm inside the SHOE software. Our method is already implemented and available for future applications also considering different energies, beams and target material from the ones previously described (${}^{16}\text{O}$ beam at 400 MeV/n impinging on a graphite target). The wrong charge assignment is never over $\sim 4.8\%$, once experimental resolution is included, even considering the complete FOOT environment.

The preliminary measurement of the cross section using the GSI April 2019 data taking is the culmination of the work done. It can still be improved by studying the secondary fragmentation in the data, the systematic error and applying the charge mixing matrix but it is an excellent starting point for further studies by the research group considering also that during the data acquisition used not all the experimental setup was available. All the code needed to produce these results is now ready to be used in a more complete data acquisition during the last month of 2020 at CNAO, using ${}^{12}\text{C}$ ions at 200 MeV/nucleon. An application for beam time in 2021/2022 at GSI is in preparation, having as one of the main priorities the request of a ${}^4\text{He}$ ion beam at 700 MeV/nucleon useful for radiation protection in space studies. In future, an update of the FOOT detector can be envisaged: the evaluation of the neutron production together with the charged fragments can constrain even more strongly Monte Carlo nuclear production models that are relevant both for Particle Therapy

and radioprotection in deep space. For this reason, different studies on providing neutron detection capability to the FOOT experiment are currently under study.

Appendix A

Bethe-Bloch parametrized curves

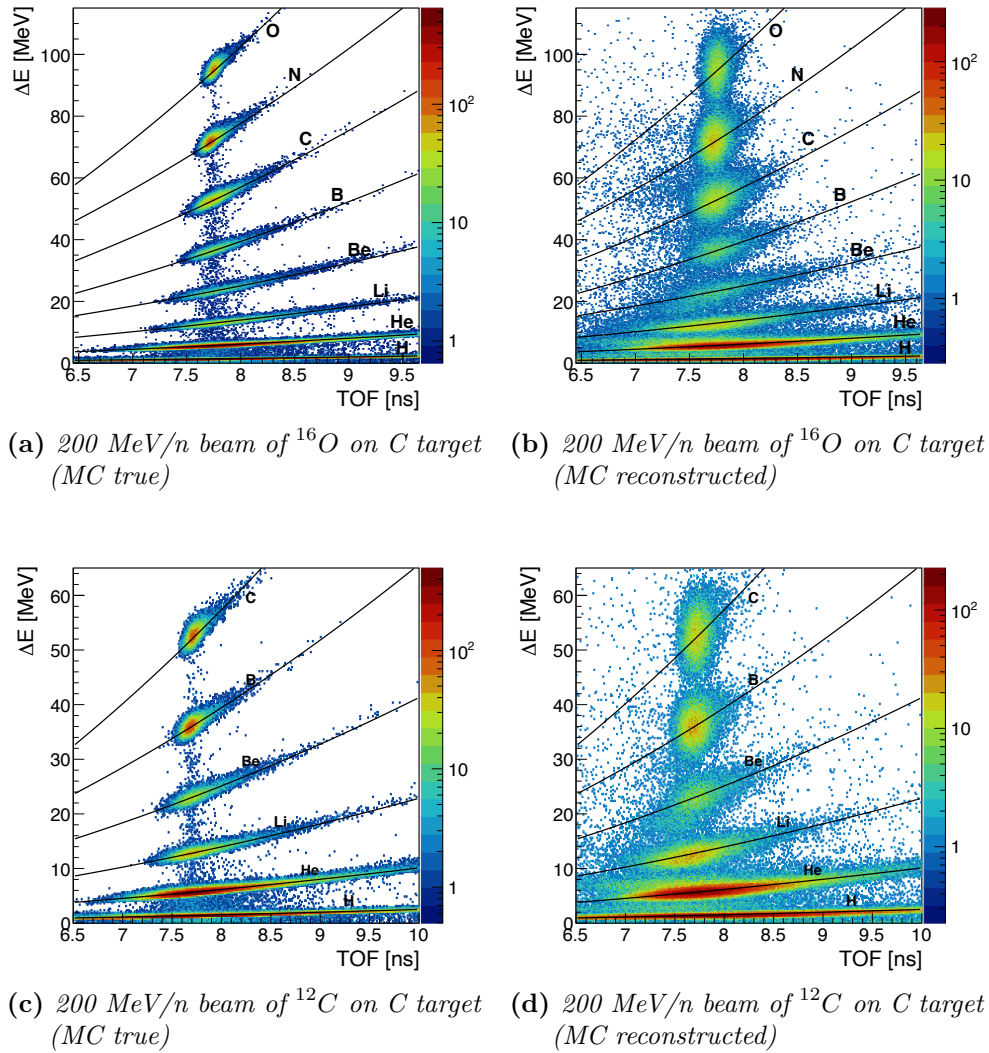
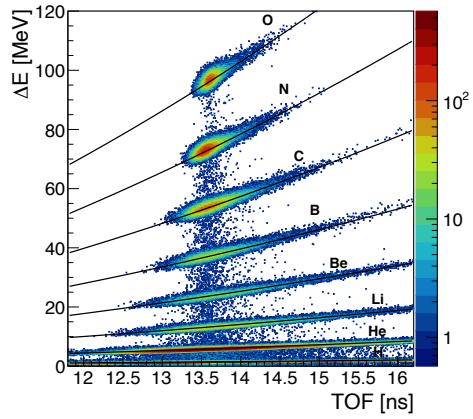
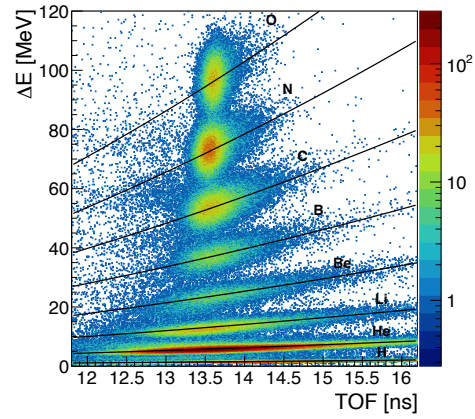


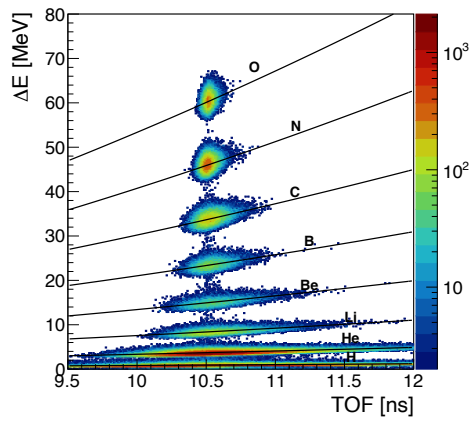
Figure A.1. Bethe-Bloch parametrization with full set of detectors



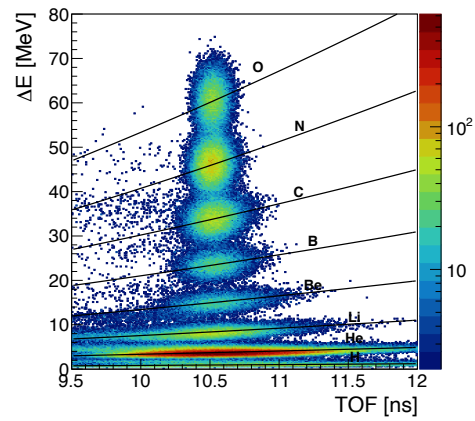
(a) 200 MeV/n beam of ^{16}O on C target (MC true)



(b) 200 MeV/n beam of ^{16}O on C target (MC reconstructed)



(c) 400 MeV/n beam of ^{16}O on C target (MC true)



(d) 400 MeV/n beam of ^{16}O on C target (MC reconstructed)

Figure A.2. Bethe-Bloch parametrization with GSI set of detectors

Appendix B

Bisection method

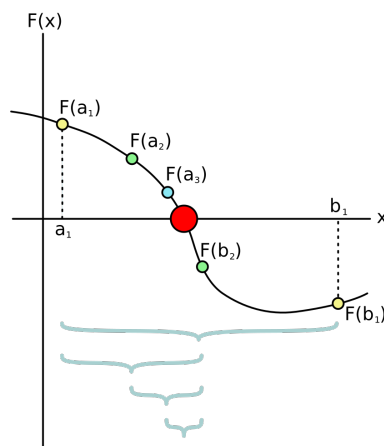


Figure B.1. A few steps of the bisection method applied over the starting range $[a_1; b_1]$. The bigger red dot is the root of the function.

In mathematics, *the bisection method* is a root-finding method that applies to any continuous functions for which one knows two values with opposite signs. The method consists of repeatedly bisecting the interval defined by these values and then selecting the subinterval in which the function changes sign, and therefore must contain a root (see figure B.1). The input for the method is a continuous function f , an interval $[a, b]$, and the function values $f(a)$ and $f(b)$. The function values are of opposite sign (there is at least one zero crossing within the interval). Each iteration performs these steps:

- Calculate c , the midpoint of the interval, $c = \frac{a+b}{2}$
- Calculate the function value at the midpoint, $f(c)$.
- If convergence is satisfactory (that is, $c - a$ is sufficiently small, or $|f(c)|$ is sufficiently small), return c and stop iterating.
- Examine the sign of $f(c)$ and replace either $(a, f(a))$ or $(b, f(b))$ with $(c, f(c))$ so that there is a zero crossing within the new interval.

Appendix C

Birk's Law

The organic scintillators are aromatic hydrocarbon compounds containing linked or condensed benzene-ring structures. Their most distinguishing feature is a very rapid decay time on the order of a few nanoseconds or less. Scintillation light in these compounds arises from transitions made by the free valence electrons of the molecules. These delocalized electrons are not associated with any particular atom in the molecule and occupy what are known as the n -molecular orbitals. A typical energy diagram for these orbitals is shown in figure C.1, where we have distinguished the spin singlet states from the spin triplet states. The ground state is a singlet state which we denote by S_0 . Above this level are the excited singlet states (S^* , S^{**} , ...) and the lowest triplet state (T_0) and its excited levels (T^* , T^{**} , ...). Also

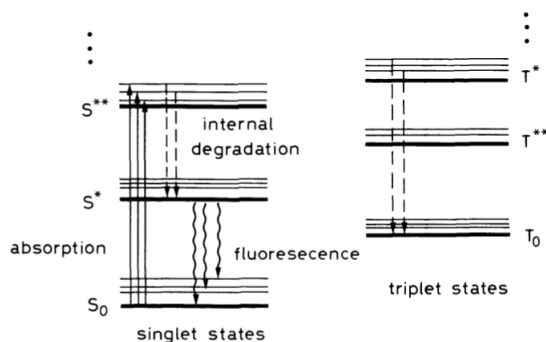
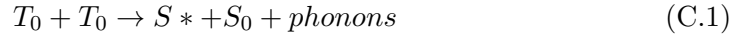


Figure C.1. Energy level diagram of an organic scintillator molecule. For clarity, the singlet states (denoted by S) are separated from the triplet states (denoted by T)

associated with each electron level is a fine structure which corresponds to excited vibrational modes of the molecule. The energy spacing between electron levels is on the order of a few eV whereas that between vibrational levels is of the order of a few tenths of eV. Ionization energy from penetrating radiation excites both the electron and vibrational levels as shown by the solid arrows. The singlet excitations generally decay immediately (<10 ps) to the S^* state without the emission of radiation, a process which is known as *internal degradation*. From S^* , there is generally a high probability of making a radiative decay to one of the vibrational states of the ground state S_0 (wavy lines) within a few nanoseconds time. This is the normal process

of *fluorescence*. The fact that S^* decays to excited vibrational states of S_0 , with emission of radiation energy less than that required for the transition $S_0 \rightarrow S^*$ also explains the transparency of the scintillators to their own radiation. For the triplet excited states, a similar internal degradation process occurs which brings the system to the lowest triplet state. While transitions from T_0 to S_0 are possible, they are, however, highly forbidden by multipole selection rules. The T_0 state, instead, decays mainly by interacting with another excited T_0 molecule:



to leave one of the molecules in the S^* state. Radiation is then emitted by the S^* as described above. This light comes after a *delay time* characteristic of the interaction between the excited molecule and is the delayed or slow component of scintillator light. It is commonly assumed that scintillators respond in a linear fashion

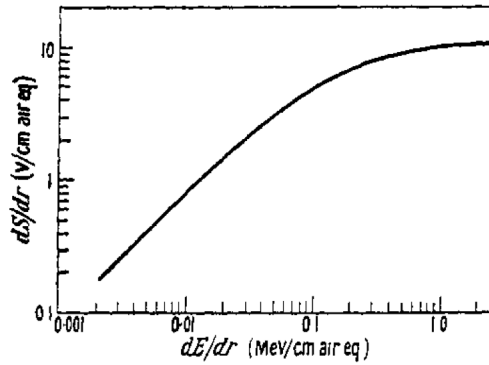


Figure C.2. Specific fluorescence dS/dr plotted against specific energy loss dE/dr in anthracene.

with respect to the exciting energy, that is the fluorescent light emitted is directly proportional to the energy deposited by the ionizing particle. Strictly speaking, this linear relation is not true (see figure C.2), although for many applications it can be considered as a good approximation.

Birks' law[48][49](named after British physicist John B. Birks) is an empirical formula for the light yield per path length as a function of the energy loss per path length for a particle traversing a scintillator, and gives a relation that is not linear at high loss rates.

The relation is:

$$\frac{dL}{dx} = S \frac{\frac{dE}{dx}}{1 + k_B \frac{dE}{dx}} \quad (\text{C.2})$$

where L is the light yield, S is the scintillation efficiency, dE/dx is the energy loss of the particle per path length, and k_B is Birks' constant, which depends on the material. k_B is 0.126 mm/MeV for polystyrene-based scintillators and $1.26 - 2.07 \times 10^{-2} \text{ g/(MeV cm}^2\text{)}$ for polyvinyltoluene-based scintillators.

Birks speculated that the loss of linearity is due to recombination and quenching effects between the excited molecules and the surrounding substrate. Birks' law has mostly been tested for organic scintillators.

Bibliography

- [1] WHO, World Health Organization *World Health Statistics 2020*. Monitoring health for the SDGs (sustainable development goals).
- [2] Durante M., Orecchia R., Loeffler J. S. *Charged-particle therapy in cancer: clinical uses and future perspectives* Nat Rev Clin Oncol 14, 483–495 (2017).
- [3] Jermann M. Particle Therapy Statistics in 2014. International Journal of Particle Therapy (2015) 2(1):50-54.
- [4] *Particle Data Group*, Review of Particle Physics, Physical Review D. August 2018, D1 PART A.
- [5] Barkas, H. W., 1963, *Nuclear Research Emulsions* Academic, New York, Vol. 1.
- [6] William R. Leo *Techinques for Nuclear and Particle Physics Experiments*, Springer-Verlag Berlin Heidelberg GmbH, Second Revised Edition 1994.
- [7] Thilo Elsässer Dieter Schardt and Daniela Schulz-Ertner. *Heavy-ion tumor therapy: Physical and radiobiological benefits*. Rev. Mod. Phys, 82(383), 2010.
- [8] S.B. Jia, A.A. Mowlavi, M.H. Hadizadeh, M. Ebrahimi Loushab *Impact of range straggling and multiple scattering on proton therapy of brain, using a slab head phantom*. International Journal of Radiation Research, April 2014. Vol 12 no. 2.
- [9] Tsai, Y. S., 1974, *Pair production and bremsstrahlung of charged leptons*, Rev. Mod. Phys. 46, 815–851.
- [10] Carlos A. Bertulani *Nuclear Physics in a Nutshell* Princeton University Press - Princeton and Oxford, 2007.
- [11] V.N Ivanchenko *Geant4 toolkit for simulation of HEP experiments* Nuclear Instruments and Methods in Physics Research Section A: Accelerators, Spectrometers, Detectors and Associated Equipment. Volume 502, Issues 2–3, 21 April 2003, Pages 666-668
- [12] C. Perrin J. Arvieux R. Bertholet J. F. Bruandet M. Buenerd R. Cherkaoui A. J. Cole Y. El-Masri N. Longequeue J. Menet F. Merchez S. Kox, A. Gamp and J. B. Viano. *Trends of total reaction cross sections for heavy ion collisions in the intermediate energy range*. Phys. Rev. C., 25:1678–1691, 1987.
- [13] E. Haettner, H. Iwase, and D. Schardt, *Experimental fragmentation studies with ^{12}C therapy beams*, Radiat. Prot. Dosim. 122 (2006) 485–487.

- [14] M- E. Lomax et al. *Biological Consequences of Radiation-induced DNA Damage: Relevance to Radiotherapy*. *Clinical Oncology* 25 (10 Oct. 2013), pp. 578–585.
- [15] Mark Oldham *Radiation physics and applications in therapeutic medicine*. Vol.36 Physics Education. William Beaumont Hospital, Royal Oak, Michigan, USA.
- [16] Jerrold T. Bushberg, J. Anthony Seibert, Edwin M. Leidholdt Jr, Jhon M. Boone *The Essential Physics of Medical Imaging*, Wolters Kulwer | Lippincott Williams & Wilkins. 2nd edition 2002 Philadelphia.
- [17] D. Shardt, T. Elsasser and D. Schulz-Ertner, *Reviews of Modern Physics*, Volume 82 (2010) p 383-425.
- [18] Scholz, M., 2003, *Effects of ion radiation on cells and tissues*, *Adv. Polym. Sci.* 62, 96–155.
- [19] G.Battistoni, M.Toppi et al. *Measuring the impact of Nuclear Interaction in Particle Therapy and in Radio Protection in Space: the FOOT experiment.*, submitted to *Frontiers in Physics*, section Medical Physics and Imaging.
- [20] Friedrich, T.; Scholz, U.; Elsasser, T.; Durante, M.; Scholz, M. *Systematic analysis of RBE and related quantities using a database of cell survival experiments with ion beam irradiation* *J. Radiat. Res.* 2012, doi:10.1093/jrr/rrs114.
- [21] Tommasino F., Durante M., *Proton radiobiology*. *Cancers*. 7 (2015), pp. 353–381.
- [22] Carabe, A.; Moteabbed, M.; Depauw, N.; Schuemann, J.; Paganetti, H. *Range uncertainty in proton therapy due to variable biological effectiveness*. *Phys. Med. Biol.* 2012, 57, 1159–1172.
- [23] Grün, R.; Friedrich, T.; Krämer, M.; Zink, K.; Durante, M.; Engenhardt-Cabillic, R.; Scholz, M. *Biologically effective proton range analysis*. *Med. Phys.* 2013, 40, 1–10.
- [24] FOOT *Conceptual design report*.
- [25] A.Ferrari et al., *FLUKA: a multi-particle transport code*, 2005. CERN-2005-10, INFN TC-05/11, SLAC-R-773.
- [26] T. Böhlen et al., *The FLUKA code: developments and challenges for high energy and medical applications*, *Nucl. Data Sheets*, vol. 120, pp. 211-214, 2014.
- [27] Battistoni G., Böhlen T. T., Cerutti F. et al. *Overview of the fluka code*. *Annals of Nuclear Energy*, 82(10), 2015.
- [28] Toppi M. et al. *Measurements of ^{12}C ion fragmentation on thin carbon target from the FIRST collaboration at GSI*. *Journal of Physics: Conference Series*, 590, 2015.
- [29] Galli L, Baldini AM, Cei A, Chiappini M, Francesconi M, Grassi M et al. *WaveDAQ: An highly integrated trigger and data acquisition system*. *Nucl Instrum Meth A* (2019) 936:399–400.

- [30] Glenn F. Knoll *Radiation Detection and Measurement*, 3rd edition. New York, 2000.
- [31] G. Silvestre *Evaluation of double-sided silicon microstrip sensor for the FOOT experiment*. Nuclear Inst. and Methods in Physics Research, A 936 (2019) 36-38.
- [32] S.M. Valle, A. Alexandrov et al. *FOOT: a new experiment to measure nuclear fragmentation at intermediate energies*, Prospectives in Science (2019) 12, 100415. Elsevier.
- [33] P. Marrocchesi, O. Adriani, Y. Akaike, M. Bagliesi, A. Basti, G. Bigongiari, S. Bonechi, M. Bongi, M. Kim, T. Lomtadze, et al., *Beam test performance of a scintillator-based detector for the charge identification of relativistic ions*, Nucl. Instrum. Methods Phys. Res. A 659 (1) (2011) 477-483.
- [34] Sarti A. et al. *Development and characterization of a ΔE -TOF detector prototype for the FOOT experiment*, Nuclear Inst. and Methods in Physics Research, A 916 (2019) 116-124.
- [35] G. De Lellis et al., *Nuclear emulsions*, CW Fabjan and H Schopper, *Elementary Particles: Detectors for Particles and Radiation*, vol. 21B, Springer, 2011.
- [36] Brun R., et al. *Root an object oriented data analysis framework*. Nuclear Instruments and Methods in Physics Research Section A: Accelerators, Spectrometers, Detectors and Associated Equipment 389 (1996), pp. 81–86.
- [37] Triparthi R. and et al. *Accurate universal parameterization of absorption cross sections*. Nuclear Instruments and Methods in Physics Research, B117:347–349, 1996.
- [38] Glauber R. J., Matthiae G. *High-energy scattering of protons by nuclei*. Nucl. Phys. B12, 135 (1970).
- [39] *ICRU, 2007, ICRU Report 78, "Prescribing, Recording and Reporting Proton-Beam Therapy," J. ICRU 7 (2)*.
- [40] A. Alexandrov, L. Alunni Solestizi et al. *The FOOT Experiment: Fragmentation Measurements In Particle Therapy*. Radiation & Applications Vol. 3 pp. 190–196, march 2019.
- [41] Daniel Cussol. *Nuclear Physics and Hadrontherapy*. LPC Caen, ENSICAEN, Université de Caen Basse-Normandie, IN2P3/CNRS, 2000.
- [42] Cho WS, Gainer JS, Kim D, Lim SH, Matchev KT, Moortgat F et al. *OPTIMASS: a package for the minimization of kinematic mass functions with constraints*. JHEP 01 (2016) 026.
- [43] Pleskac R, Abou-Haidar Z, Agodi C, Alvarez MAG, Aumann T, Battistoni G et al. *The FIRST experiment at GSI*. Nucl Instrum Meth A (2012) 678:130-138.
- [44] Thwaites D. *Accuracy required and achievable in radiotherapy dosimetry: have modern technology and techniques changed our views?* Journal of Physics: Conference Series (2013) 444:012006.

-
- [45] De Napoli M, Agodi C, Battistoni G, Blancato AA, Cirrone GAP, Cuttone G et al. *Carbon fragmentation measurements and validation of the GEANT4 nuclear reaction models for hadrontherapy*. Phys Med Biol (2012) 57:7651–7671.
- [46] Dudouet J, Labalme M, Cussol D, Finck Ch, Rescigno R, Rousseau M et al. *Zero-degree measurements of ^{12}C fragmentation at 95 MeV/nucleon on thin targets*. Phys Rev C (2014) 89:064615.
- [47] Toppi M, Abou-Haidar Z, Agodi C, Alvarez MAG, Aumann T, Balestra F et al. *Measurement of fragmentation cross sections of ^{12}C ions on a thin gold target with the FIRST apparatus*. Phys Rev C (2016) 93:064601.
- [48] Birks, J.B. (1951). *Scintillations from Organic Crystals: Specific Fluorescence and Relative Response to Different Radiations*. Proc. Phys. Soc. A64 (10): 874–877.
- [49] Birks, J.B. (1964). *The Theory and Practice of Scintillation Counting*. London: Pergamon.
- [50] M. Marrocchi et al. *Performance Evaluation of the TOF-Wall Detector of the FOOT Experiment*. journal of latex class files, Vol. 14, no. 8, August 2015.